

**DEVELOPMENT OF INTEGRATED ZINC OXIDE
NANORODS COATED GLASS SUBSTRATE SENSING
DEVICE**

HAZIEZOL HELMI BIN MOHD YUSOF

**FACULTY OF ENGINEERING
UNIVERSITY OF MALAYA
KUALA LUMPUR**

2020

**DEVELOPMENT OF INTEGRATED ZINC OXIDE
NANORODS COATED GLASS SUBSTRATE SENSING
DEVICE**

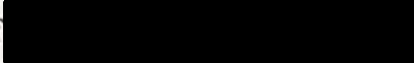
HAZIEZOL HELMI BIN MOHD YUSOF

**THESIS SUBMITTED IN FULFILMENT OF THE
REQUIREMENTS FOR THE DEGREE OF DOCTOR OF
PHILOSOPHY**

**FACULTY OF ENGINEERING
UNIVERSITY OF MALAYA
KUALA LUMPUR**

2020

UNIVERSITY OF MALAYA
ORIGINAL LITERARY WORK DECLARATION

Name of Candidate: Haziezol Helmi Bin Mohd Yusof 

Matric No: KHA160007

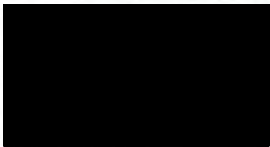
Name of Degree: Doctor of Philosophy

Title of Thesis: Development of Integrated Zinc Oxide Nanorods Coated Glass
Substrate Sensing Device

Field of Study: Electronic (Engineering and Engineering Trades)

I do solemnly and sincerely declare that:

- (1) I am the sole author/writer of this Work;
- (2) This Work is original;
- (3) Any use of any work in which copyright exists was done by way of fair dealing and for permitted purposes and any excerpt or extract from, or reference to or reproduction of any copyright work has been disclosed expressly and sufficiently and the title of the Work and its authorship have been acknowledged in this Work;
- (4) I do not have any actual knowledge nor do I ought reasonably to know that the making of this work constitutes an infringement of any copyright work;
- (5) I hereby assign all and every rights in the copyright to this Work to the University of Malaya ("UM"), who henceforth shall be owner of the copyright in this Work and that any reproduction or use in any form or by any means whatsoever is prohibited without the written consent of UM having been first had and obtained;
- (6) I am fully aware that if in the course of making this Work I have infringed any copyright whether intentionally or otherwise, I may be subject to legal action or any other action as may be determined by UM.

Candidate's Signature 

Date: 6/3/2020

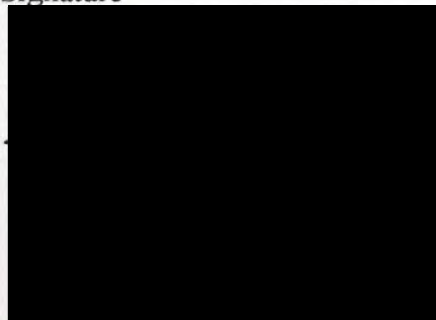
Subscribed and solemnly declared before,

Witness's Signature

Date: 6/3/2020

Name:

Designation:



DEVELOPMENT OF INTEGRATED ZINC OXIDE NANORODS COATED GLASS SUBSTRATE SENSING DEVICE

ABSTRACT

A simple and practical cost-effective integrated zinc oxide (ZnO) nanorods coated glass substrate sensing device for humidity and formaldehyde vapor sensing applications is reported. The developed sensor device is composed of a commercial light-emitting diode (LED) and photodiode that correspondingly served as light source and detector which precisely positioned on a 3D printed sensor platform. A receiver circuit and Arduino platform were employed for signal amplification and processing. A uniform ZnO nanorods coating were grown on the surface of glass substrate via hydrothermal method by controlling the growth durations and coating length. A standard reference for the optimum working condition of sensing device was presented by maximizing the dynamic range of the fabricated glass substrates towards humidity sensing. The first order of theoretical model was derived in which two new normalized parameters (Z and ζ) were introduced. An experimental validation was performed and showed well correlation towards the theoretical approach. The optimum sensing response of the sensor device was found to be effective by the determination of parameter Z and ζ instead of a specific growth conditions (growth duration and coating length). The fabricated sensor device was successfully characterized towards humidity and formaldehyde vapor concentrations. A significant response towards relative humidity (RH) levels between 35% and 90% was exhibited which the output voltage reduced in non-linear trend by 750 mV with average sensitivity of -12 mV/%. The sensing performance of the sensor device produced an average response time of 3.8 s for relative humidity (RH) level from 35% to 85% and showed quicker recovery time of 2.2 s. The device also demonstrated good response in detecting formaldehyde vapor

concentrations with good sensing stability at small change of concentration as low as 1%.

Keywords: zinc oxide, nanorods, glass substrate, humidity, dynamic range.

University of Malaya

PEMBANGUNAN PERANTI MENGESAN BERSEPADU SUBSTRAT KACA BERSALUT NANOROD ZINK OKSIDA

ABSTRAK

Sebuah peranti mengesan bersepadu substrat kaca bersalut nanorod zink oksida (ZnO) yang mudah dan kos efektif untuk aplikasi mengesan kelembapan dan wap formaldehid dilaporkan. Peranti penerima yang dibangunkan terdiri daripada diod pemancar cahaya (LED) dan diod cahaya komersial yang berfungsi sewajarnya sebagai sumber dan pengesan cahaya, di mana disusun secara tepat di atas platform penerima yang dicetak secara 3D. Satu litar penerima dan platform Arduino digunakan untuk penguatan dan pemprosesan isyarat. Satu lapisan salutan nanorod ZnO yang seragam ditumbuhkan di atas permukaan substrat kaca melalui kaedah hidroterma dengan mengawal tempoh pertumbuhan dan panjang salutan. Satu rujukan piawai untuk keadaan bekerja yang optimum bagi sebuah peranti pengesan dibentangkan dengan memaksimumkan julat dinamik substrat kaca yang telah difabrikasikan terhadap mengesan kelembapan. Model teori terbit pertama diterbitkan di mana dua parameter yang dinormalkan (Z dan ζ) telah diperkenalkan. Satu pengesanan ujikaji telah dilakukan dan menunjukkan satu hubungan sekaitan yang baik dengan pendekatan teori. Tindak balas optimum mengesan oleh peranti penerima didapati berkesan dengan penentuan oleh parameter Z dan ζ bukannya pada keadaan penumbuhan yang tertentu (tempoh penumbuhan dan jarak salutan). Peranti penerima yang telah dibangunkan berjaya dicirikan terhadap kadar kepekatan kelembapan dan wap formaldehid. Satu tindakbalas yang ketara terhadap aras kelembapan relatif (RH) di antara 35% dan 90% dipamerkan di mana voltan keluaran berkurangan secara tidak lurus sebanyak 750 mV dengan purata kepekaan sebanyak -12 mV/%. Prestasi mengesan bagi peranti penerima ini menghasilkan purata masa tindak balas sebanyak 3.8 s untuk aras kelembapan relatif (RH) dari 35% ke 85% dan menunjukkan masa pemulihan yang lebih cepat sebanyak

2.2 s. Peranti ini juga menunjukkan tindakbalas yang baik di dalam mengesan kepekatan wap formaldehid dengan kestabilan mengesan yang baik pada perubahan kepekatan yang kecil serendah 1%.

Kata Kunci: zink oksida, nanorod, substrat kaca, kelembapan, julat dinamik.

University of Malaya

ACKNOWLEDGEMENTS

Alhamdulillah, all praises to Allah for giving me the opportunity, determination and strength to complete my research and this thesis. His continuous grace and mercy was with me throughout my life and my research period. Special appreciation goes to my supervisor, Prof. Ir. Dr. Sulaiman Wadi Harun for his great supervision and constant support. His vast knowledge in this field has been a source of motivation and inspiration throughout my research work. I also wish to express my deep gratitude to my co-supervisors, Prof. Ir. Dr. Kaharudin Dimiyati and Dr. Waleed S. Mohammed (Bangkok University). The successful of this research would not have been possible without their constant guidance and support.

My appreciation also goes to all photonics laboratory members in University of Malaya for their kind support, assistance and made the lab most enjoyable to work in despite the stressful and challenges of the research work. I like to extend my special credit to Dr. Hazli Rafis Bin Abdul Rahim for his continuous support during my research period.

Most importantly, my special gratitude goes to my beloved parents; Mohd Yusof Bin Saat and Norizan Binti Ismail for their encouragement and prayers. To my dearest wife, Nurafni Binti Ibrahim, thank you for the love and always been there with me through the ups and downs. Not to forget, the appreciation also goes to all family members for their understanding and support.

Lastly, I like to thank University Teknikal Malaysia Melaka (UTeM) and Ministry of Education (MOE) of Malaysia for sponsoring my PhD program under SLAB/SLAI scholarship.

TABLE OF CONTENTS

Abstract	iii
Abstrak	v
Acknowledgements	vii
Table of Contents	viii
List of Figures	xi
List of Tables	xvii
List of Symbols and Abbreviations	xviii
List of Appendices	xxiv
CHAPTER 1: INTRODUCTION.....	1
1.1 Background.....	1
1.2 Nanomaterial in Optical Sensor.....	2
1.3 Problem Statement.....	5
1.4 Objectives of the Research	7
1.5 Limitation of the Research.....	8
1.6 Thesis Organization.....	8
CHAPTER 2: LITERATURE REVIEW.....	10
2.1 Introduction.....	10
2.2 Concept of Light Propagation.....	11
2.3 Flat Surface Glass Substrate as Light Propagation Medium	15
2.4 Glass Substrate in Sensing Application.....	18
2.5 Intensity Modulation Based Sensors	19
2.6 Zinc Oxide Crystal Structure	23
2.7 Zinc Oxide Nanostructure via Hydrothermal Synthesis Method	26

2.8	Optimization of ZnO Growth	33
2.9	Humidity and Formaldehyde Vapor Sensing	36
2.9.1	Humidity Sensing	37
2.9.2	Formaldehyde Vapor Sensing	42
2.10	Arduino as Data Acquisition Platform for Sensing Device.....	44
2.11	Op-Amp for Signal Conditioning	47

CHAPTER 3: GROWTH OF ZINC OXIDE NANOROD ONTO GLASS SUBSTRATE VIA HYDROTHERMAL SYNTHESIS METHOD 51

3.1	Introduction.....	51
3.2	Growth of ZnO Nanorods via Hydrothermal Method on Glass Substrates.....	52
3.2.1	Preparation of Glass Substrates	52
3.2.2	Seeding Process	56
3.2.3	Growth Process.....	59
3.3	Optical Image of ZnO Nanorods Layer on Glass Substrates.....	62
3.4	ZnO Nanorods Characterization via FESEM	63
3.5	Optical Characterization of Glass Substrates Coated with ZnO Nanorods	69
3.6	Measurement of Forward and Backward Scattering by ZnO Nanorods.....	80
3.7	Summary.....	83

CHAPTER 4: MAXIMIZATION OF OPTICAL DYNAMIC RANGE FOR HUMIDITY SENSING BY CONTROLLING GROWTH OF ZINC OXIDE NANORODS 84

4.1	Introduction.....	84
4.2	Humidity Characterization.....	85
4.3	Dynamic Range Maximization Model.....	97

4.4	Fabrication of ZnO Nanorods Coating onto Glass Substrate for the Development of Humidity Sensing Device.....	105
4.5	Summary.....	111

CHAPTER 5: ZINC OXIDE NANORODS COATED GLASS SUBSTRATE BASED SENSING DEVICE 112

5.1	Introduction.....	112
5.2	Integration of Zinc Oxide Based Sensor Device	113
5.2.1	Design of Sensor Assembly	114
5.2.2	Receiver Circuit of Sensor System.....	118
5.2.3	Device Assembly.....	120
5.2.4	Receiver Circuit to Arduino Controller Board Interface.....	122
5.3	Humidity Sensing Experiment.....	123
5.4	Formaldehyde Vapor Sensing	130
5.4.1	Preparation of Formalin Solution	130
5.4.2	Formaldehyde Vapor Experiment	131
5.5	Summary.....	138

CHAPTER 6: CONCLUSION AND FUTURE WORK 139

6.1	Conclusion	139
6.2	Future Work.....	141
	References	142
	List of Publications	162
	Appendix.....	163

LIST OF FIGURES

Figure 2.1 Types of optical fiber sensors. (a) Extrinsic. (b) Intrinsic.	11
Figure 2.2 Light propagation at interface between two different media.	12
Figure 2.3 Structure of optical fiber cable.	14
Figure 2.4 Concept of light propagation inside an optical fiber.	15
Figure 2.5 Total internal reflection at glass-air interface.	15
Figure 2.6 Basic setup for the excitation of surface plasmons by means of a beam light (Parisi <i>et al.</i> , 2008).	18
Figure 2.7 Classification of optical sensor operating principles.	19
Figure 2.8 Micro-bending based fiber sensor (Connelly, 2004).	20
Figure 2.9 Evanescent wave optical fiber sensor (Fidanboylu <i>et al.</i> , 2009).	21
Figure 2.10 Wurtzite structure of ZnO.	23
Figure 2.11 ZnO structures (a) nanowires (Shan <i>et al.</i> , 2008), (b) nanorods (Dedova <i>et al.</i> , 2007), (c) snowflakes (Jing <i>et al.</i> , 2012) and (d) nanoflowers (Miles <i>et al.</i> , 2015).	25
Figure 2.12 Growth morphologies of ZnO structure in the form of (a) nanowire/rod, (b) polar nanobelt, (c) nanobelt type A and (d) nanobelt type B (Baruah, 2011).	26
Figure 2.13 Spectral electron microscopy (SEM) images of ZnO nanostructures grown under different solution pH value of (a) 1.8, (b) 4.6, (c) 6.6, (d) 9.1, (e) 10.8 and (f) 11.2 (Amin <i>et al.</i> , 2011).	28
Figure 2.14 SEM images of ZnO nanorods grown under chemical concentrations of (a) 25 mM, (b) 50 mM, (c) 100 mM and (d) 300 mM. (Amin <i>et al.</i> , 2011).	29
Figure 2.15 SEM images of ZnO nanorods fabricated hydrothermally using precursor solutions with molar ratio of (a) 10:0, (b) 5:1, (c) 2:1, (d) 1:1, (e) 1:1.2 and (f) 2:3. (Mahmood <i>et al.</i> , 2013).	32
Figure 2.16 Cross-sectional SEM images of ZnO nanorods fabricated at temperature of (a) 50 °C, (b) 70 °C and (c) 90 °C. (Mahmood <i>et al.</i> , 2013).	33
Figure 2.17 Schematic representation on light side coupling to cladding modes through ZnO nanorods (Fallah <i>et al.</i> , 2013).	34

Figure 2.18 Schematic representation showing the side coupling of light to cladding mode in an optical fiber coated with ZnO nanorods (Bora <i>et al.</i> , 2014).....	35
Figure 2.19 Average output voltage observed by light side coupling demonstration on samples with different growth times (Rahim, Lokman, <i>et al.</i> , 2016).	36
Figure 2.20 Experimental setup for humidity sensing using tapered POF coated with Al-doped ZnO nanostructures (Z Harith <i>et al.</i> , 2017).	39
Figure 2.21 Experimental setup for humidity sensing with optical fiber coated with ZnO nanoparticles (Aneesh <i>et al.</i> , 2011).	40
Figure 2.22 Experimental setup utilizing silica fiber coated with ZnO nanorods arrays for humidity sensing (Yanjuan Liu <i>et al.</i> , 2012).	41
Figure 2.23 Schematic representation of the fabricated device structure for formaldehyde detection (Peng <i>et al.</i> , 2009).	43
Figure 2.24 Arduino UNO R3 layout (Barrett, 2013).	45
Figure 2.25 Arduino UNO R3 systems (Barrett, 2013).	46
Figure 2.26 General symbol of an op-amp (Fiore, 1992).	47
Figure 2.27 Equivalent circuit of the op-amp configuration with photodiode (Sterckx, 2015).	48
Figure 2.28 Schematic diagram of (a) LT1884 (LinearTechnology, 2000) and (b) LM358 (TexasInstrument, 2014).	50
Figure 3.1 General procedures of ZnO nanorods synthesis via hydrothermal method... ..	52
Figure 3.2 Glass substrate preparation process.	53
Figure 3.3 Glass slides cutting process. (a) Dimension of glass substrates to be cut from glass slide. (b) Glass slide cutting process with glass cutter. (c) The edges of the glass substrates. (d) Final dimension of glass substrate after cutting process.	54
Figure 3.4 Glass substrate cleaning procedure.	55
Figure 3.5 (a) Glass substrate masking process by using PTFE tape. (b) Dimension of the exposed triangular area. (c) Final masked glass substrate.	56
Figure 3.6 Procedures of seeding process on glass substrate.	57
Figure 3.7 Preparation of seeding solution.	57
Figure 3.8 Masked samples seeding procedure.	58

Figure 3.9 The process of seeding. (a) Masked glass substrates were heated on hot plate. (b) Drop and dry seeding process.....	58
Figure 3.10 Annealing process in a furnace.....	59
Figure 3.11 Procedure for growth process of ZnO nanorods. (a) Stages used for placing seeded glass substrates on petri dish. (b) Seeded glass substrates were placed facing downwards in petri dish. (c) Glass substrates dipped in precursor solutions and placed in an oven.	60
Figure 3.12 Final procedures after the growth process.....	61
Figure 3.13 Successful ZnO nanorods coated glass substrates at growth time of 5 h, 10 h and 15 h.....	62
Figure 3.14 Uniform ZnO nanorods coating in triangular shapes on glass substrates for the growth durations of (a) 5 h, (b) 10 h and (c) 15 h.....	63
Figure 3.15 Top view of the ZnO nanorods grown on glass substrate for the growth durations of (a) 5 h, (b) 10 h and (c) 15 h.....	64
Figure 3.16 Cross sectional SEM image of ZnO nanorods on glass substrate for the growth durations of (a) 5 h, (b) 10 h and (c) 15 h.....	65
Figure 3.17 The comparison graph between the growth time for the (a) length, (b) diameter and (c) number of nanorods per unit area.....	67
Figure 3.18 Typical XRD pattern of ZnO nanorods grown on glass substrate.....	68
Figure 3.19 EDS spectrum of ZnO nanorods showing the peak of zinc and oxygen.....	69
Figure 3.20 Schematic representation of the experimental setup for light scattering behavior of the glass substrate coated with ZnO nanorods. The inset shows the scanning direction of the light scattering measurement.....	70
Figure 3.21 Actual setup for optical characterization.....	71
Figure 3.22 Incident angle of light source at the edge of glass substrate to achieve total internal reflection inside the glass substrate.....	71
Figure 3.23 Light propagates inside the ZnO coated glass substrate via edge excitation.....	72
Figure 3.24 The leakage of light via ZnO coating at (a) shorter coating section and (b) longer coating section.....	73

Figure 3.25 Optical characterization of the ZnO coated glass substrate on coating length variation for the growth duration of (a) 5 h, (b) 10 h and (c) 15 h.....	75
Figure 3.26 Optical measurements of the ZnO nanorods coated on glass substrate for the output intensity measurement at different lengths of ZnO coating.....	77
Figure 3.27 Optical measurements of the ZnO nanorods coated on glass substrate for the scattering coefficient at different lengths of ZnO coating.	79
Figure 3.28 Average scattering coefficient for glass substrate coated with ZnO nanorods at 5 h, 10 h and 15 h growth times.	79
Figure 3.29 Measurement for light scattering by ZnO nanorods.....	80
Figure 3.30 Experimental setup for light scattering by ZnO nanorods measurement for (a) forward and (b) backward.....	81
Figure 3.31 Forward scattering of the ZnO nanorods at growth durations of 5 h, 10 h and 15 h.....	82
Figure 3.32 Backward scattering of the ZnO nanorods at growth durations of 5 h, 10 h and 15 h.....	83
Figure 4.1 Schematic representation of the experimental setup for humidity testing.....	86
Figure 4.2 Four different coating lengths coverage for humidity characterization.....	87
Figure 4.3 The response of humidity sensing on fabricated glass substrates at growth durations of (a) 5 h, (b) 10 h and (c) 15 h.	89
Figure 4.4 A schematic diagram for adsorption of water molecules on ZnO nanorods surface.	91
Figure 4.5 Refractive index of air varies towards humidity concentrations.	94
Figure 4.6 Comparison of humidity response at 80% RH concentrations for samples with different processing time.....	95
Figure 4.7 Sensing responses on two different growth combinations of ZnO nanorods.....	97
Figure 4.8 Schematic representation of the fabricated device including the detection scheme.....	98
Figure 4.9 Schematic representation of the sensor showing the substrates coated with ZnO nanorods.....	99
Figure 4.10 The dynamic range analysis for the optimum sensor device.....	99

Figure 4.11 Contour plots for the dynamic range (ΔT) versus the normalized length (Z) and normalized scattering coefficient (ζ). The blue line running down from $Z = 1$ to 0.25 represents the values of $Z_{Optimum}$ obtained from Equation (4.12).	101
Figure 4.12 3D contour plot for dynamic range analysis	103
Figure 4.13 Experimental contour plots for the dynamic range (ΔT) versus the normalized length (Z) and normalized scattering coefficient (ζ).	104
Figure 4.14 Sample masked with PTFE tape with square area exposed for ZnO coating.	105
Figure 4.15 Successful glass substrate coated with square shaped ZnO nanorods for growth duration of (a) 5 h, (b) 10 h and (c) 15 h.	106
Figure 4.16 Humidity measurements on the new fabricated samples at fixed position of stage.	107
Figure 4.17 Humidity sensing response of fabricated samples for humidity concentration between 50% and 80% of RH.	108
Figure 4.18 Transmittance reduction of fabricated samples measured at 80% of RH.	108
Figure 4.19 Correlation between the fabricated samples with theoretical approach for humidity characterization.	109
Figure 4.20 SEM micrographs of (a) top and (b) cross sectional of ZnO nanorods grown on glass substrate.	110
Figure 5.1 Development process of integrated sensing device.	114
Figure 5.2 Schematic representation of integration of the optical sensor board (Orthographic view of the sensor body model).	115
Figure 5.3 The (a) front, (b) top and (c) side view of the fabricated sensor body via 3D printing.	116
Figure 5.4 Schematic representation of the LED/photodiode cover dimension.	117
Figure 5.5 Fabricated cover for LED/photodiode.	117
Figure 5.6 Schematic diagram of transimpedance amplifier (TIA).	119
Figure 5.7 (a) Orthographic view, (b) top view, and (c) bottom view of the fabricated humidity sensor device integrated with op-amp circuit.	121
Figure 5.8 Wiring diagram for the connection between receiver circuit and Arduino platform.	122

Figure 5.9 Schematic representation of the experimental setup used for humidity sensing.....	124
Figure 5.10 The image of (a) front and (b) top view of the actual of humidity experiment conducted with integrated sensor device.....	124
Figure 5.11 Humidity sensing performance of a typical sensor device.	125
Figure 5.12 Three region of sensitivity of the sensor device. (a) 35% to 55% of RH, (b) 55% to 70% of RH and (c) 70% to 90% of RH.	127
Figure 5.13 Sensor performance analysis. (a) Sensor repeatability at 90% of RH level with respect to room level (50%) and (b) sensor response time and recovery time of the sensor device.	129
Figure 5.14 Schematic representation of the experimental setup used for formaldehyde vapor sensing.....	132
Figure 5.15 Formaldehyde vapor sensing at different RH level.	133
Figure 5.16 Reduction of output voltage for the fabricated sensor in response to the vapor concentrations.	133
Figure 5.17 The stability analysis of the fabricated sensor.....	135
Figure 5.18 Formaldehyde vapor sensing performance.....	136

LIST OF TABLES

Table 2.1 Properties comparison between the transparent materials (KOPP-Glass, 2016).	17
Table 2.2 Properties of ZnO (Baruah, 2011)	24
Table 2.3 Humidity and formaldehyde vapor sensing progress utilizing ZnO as sensing material.....	37
Table 5.1 The output voltage read by Arduino platform.	125
Table 5.2 Performance comparison of humidity sensor with previous works.....	130
Table 5.3 The total reduction of output voltage in average upon exposure to formaldehyde vapor.	137
Table 5.4 Comparison between relative humidity and formaldehyde vapor sensing by the developed sensor device.....	138

LIST OF SYMBOLS AND ABBREVIATIONS

SYMBOLS

n	:	Refractive index
c	:	Speed of light in vacuum
v	:	Speed of light in medium
T	:	Transmittance
α	:	Attenuation coefficient
x	:	Length of path
n_1	:	Refractive index of medium 1
n_2	:	Refractive index of medium 2
θ_i	:	Incident angle
θ_c	:	Critical angle
n_{air}	:	Refractive index of air
n_{zno}	:	Refractive index of zinc oxide
n_{core}	:	Refractive index of optical fiber core
V_{in+}	:	Positive input voltage
V_{in-}	:	Negative input voltage
V_{out}	:	Output voltage
$+V$:	Positive voltage supply
$-V$:	Negative voltage supply
V_b	:	Negative bias voltage
R_f	:	Feedback resistor
V_o	:	Output voltage
i_d	:	Photocurrent
C_d	:	Junction capacitance

n_{glass}	:	Refractive index of glass
2θ	:	Diffraction angle
I	:	Intensity of output light
I_0	:	Intensity of input light
Z	:	Distance of propagation
C_{sc}	:	Scattering cross section
ρ_v	:	Rods density per unit volume
ρ_a	:	Average rods area
L	:	Average rods length
L	:	Coating length
ΔT	:	Optical transmission difference
W	:	Watt
ϵ_r	:	Dielectric constant of a medium
ϵ'	:	Real part of dielectric constant
ϵ''	:	Imaginary part of dielectric constant
N	:	Complex refractive index
K	:	Imaginary part of complex refractive index
σ	:	Conductivity
ϵ	:	Dielectric function
J	:	Electric current density
E	:	Electric field vector
D	:	Electrical displacement field
n_{humid_air}	:	Refractive index of humid air
t_g	:	Growth time
T_{max}	:	Transmittance at maximum humidity
T_{min}	:	Transmittance at minimum humidity

α_1	:	Scattering coefficient at maximum humidity
α_2	:	Scattering coefficient at minimum humidity
Z	:	Normalized length
ζ	:	Normalized scattering coefficient
Z_{max}	:	Normalized length at maximum dynamic range
ΔT_{max}	:	Maximum dynamic range
V_{fmax}	:	Minimum forward voltage
I_{fmax}	:	Maximum forward current
V_s	:	Voltage supply
R_s	:	Series resistor
I_d	:	Photocurrent
C_f	:	Feedback resistor
GND	:	Ground
M_1	:	Molarity of concentrate solution
M_2	:	Molarity of dilute solution
V_1	:	Volume of concentrate solution
V_2	:	Volume of dilute solution
ΔV	:	Output voltage reduction

ABBREVIATIONS

EMI	:	Electromagnetic interference
ZnO	:	Zinc oxide
TiO ₂	:	Titanium dioxide
SnO ₂	:	Tin oxide
In ₂ O ₃	:	Indium oxide
NiO	:	Nickel oxide

O ₂	:	Oxygen
CO ₂	:	Carbon dioxide
NH ₃	:	Ammonia
CH ₄	:	Methane
C ₄ H ₁₀	:	Butane
ZnO:Al	:	Aluminum doped zinc oxide
He-Ne	:	Helium-neon
PTFE	:	Polytetrafluoroethylene
SiO ₂	:	Silicon dioxide
B ₂ O ₃	:	Boron trioxide
Na ₂ O	:	Sodium oxide
CaO	:	Calcium oxide
P ₂ O ₅	:	Phosphorus pentoxide
UV	:	Ultraviolet
IR	:	Infrared
SPR	:	Surface Plasmon Resonance
IM	:	Intensity modulation
WO ₃	:	Tungsten oxide
Zn	:	Zinc
O	:	Oxygen
1D	:	One-dimensional
2D	:	Two dimensional
3D	:	Three dimensional
Zn(NO ₂) ₃	:	Zinc nitrate hexahydrate
pH	:	Acidity scale
SEM	:	Spectral electron microscopy

ZnCl ₂	:	Zinc chloride
NaOH	:	Sodium hydroxide
Zn(OH) ₂	:	Zinc hydroxide
HCl	:	Hydrochloric acid
HMT	:	Hexamethylenetetramine
RH	:	Relative humidity
POF	:	Plastic optical fiber
Al	:	Aluminum
DAQ	:	Data acquisition
HCHO	:	Formaldehyde
UF	:	Urea-formaldehyde
PF	:	Phenol-formaldehyde
VOCs	:	Volatile organic compounds
WHO	:	World health organization
IARC	:	International Agency for Research on Cancer
ITO	:	Indium tin oxide
Xe	:	Xenon
GPU	:	Graphical processing unit
PWM	:	Pulse width modulation
USB	:	Universal serial bus
ADC	:	Analog-to-digital converter
Op-amp	:	Operational amplifier
DI	:	Deionized
Zn(CH ₃ COO) ₂	:	Zinc acetate
Zn(NO ₃) ₂ ·6H ₂ O	:	Zinc nitrate hexahydrate
(CH ₂) ₆ N ₄	:	Hexamethylenetetramine

XRD	:	X-ray diffraction
JCPDS	:	The Joint Committee on Powder Diffraction Standards
EDS	:	Energy dispersive spectroscopy
Pt	:	Platinum
C	:	Carbon
Si	:	Silicon
Ca	:	Calcium
GUI	:	Graphical user interface
LED	:	Light-emitting diode
PC	:	Personal computer
OH	:	Hydroxyl
IM/DD	:	Intensity modulation/direct detection
PLA	:	Poly lactid acid
PCB	:	Printed circuit board
VDC	:	Direct current voltage
Au	:	Gold
Ag	:	Silver
Pt	:	Platinum
Pd	:	Palladium

LIST OF APPENDICES

Publications

University of Malaya

CHAPTER 1: INTRODUCTION

1.1 Background

In recent years since our civilization has becoming more technologically advanced, the interest for information in every aspect of daily life has developed enormously. The technology of sensor device and its detection scheme play an important aspect in the process of collecting information (Patni *et al.*, 2015). Sensor is defined as a device that reacts to a stimulus by producing a functional output induced by a change in some intrinsic properties (Brugger, 2009). The example of stimulus can be physical quantities such as concentration of a specific chemical, biochemical material, chemical vapors, temperature or pressure. An output signal which known as measurand from a sensor device usually appears in voltage, resistance or others and typically varies in respond to the changes in physical parameters (Setter *et al.*, 2006). Generally, sensors are divided into six classes; optical, mechanical, thermal, magnetic, electronic and electrochemical sensors in which they are categorized by its transduction of energy (Setter *et al.*, 2006). Recent optical fiber technology has expanded the interest among researchers for optical based sensors due to the advantages of light characteristics over electronic systems (Sabri *et al.*, 2013). Optical system commonly requires smaller medium for information transfer in comparison to magnetic or electronic systems. Electronic systems are susceptible to electronic interference (EMI) which renders them unsuitable for use in hazardous and explosive environments (Correia *et al.*, 2012). Optical based sensors offer several advantages over electronic sensors. Instead of electrical current, an optical sensor utilizes light rays when measuring physical quantities in which detection is based on the demodulation of light intensity (Ahuja *et al.*, 2012) or wavelength (Setter *et al.*, 2006). Thus, it has immunity to EMI, often providing higher sensitivity and dynamic range of operation, wider bandwidth, faster response time and ability to transmit signals over long distances for remote operations

(Correa-Mena *et al.*, 2017; Ghadir *et al.*, 2016; A. Lokman *et al.*, 2016; Sabri *et al.*, 2013).

The innovation in optical sensors has discovered its noteworthy applications in numerous fields, for example, biotechnology, environmental monitoring pharmaceuticals and clinical analysis (Narayanaswamy *et al.*, 2013). As one of the powerful analytical tool, it has capability in providing information such as their presence, concentration, and other physical properties of interest (Pan *et al.*, 2013). In chemical and biological applications (Narayanaswamy *et al.*, 2013), optical sensors are particularly having advantageous for remote and multimodal sensing compared to other types of sensors that using electronic (Allen *et al.*, 2007), electrochemical (Joseph Wang, 2005) or mechanical (Carrascosa *et al.*, 2006; Fritz *et al.*, 2000) transduction. The recent progress of sensors development focused towards in producing higher sensitive and effective sensing device which leads to almost real-time response (Marquez *et al.*, 2015). The introduction of nanomaterials in the development of sensor device has tremendously improved the sensing performance especially in biosensors (Pandit *et al.*, 2016) and environmental monitoring (Su *et al.*, 2012). The possession of nanomaterials for their unique properties have drawn attention among researchers for the evolution towards nanomaterial-based sensor device in various fields (Chauhan *et al.*, 2016).

1.2 Nanomaterial in Optical Sensor

The advancement in nanotechnology has led the innovation towards high-speed electronics, high efficiency catalyst and sensors (Marquez *et al.*, 2015). According to National Science Foundation and National Nanotechnology Initiative (H. Chen *et al.*,

2013), nanotechnology is described as the material manipulation and control on physical, chemical and biological system at the scale between the range of 0.1 to 100 nm (Keyvani, 2007). Nanomaterial made its first discovery in 1985 (Chauhan *et al.*, 2016) with the introduction of carbon fullerenes (Iijima, 1991; Krätschmer *et al.*, 1990), followed by the carbon nanotubes (Ebbesen *et al.*, 1992) and mesoporous (Kresge *et al.*, 1992) materials in 1991 and 1992, respectively. In the development of sensing device, nanomaterial has gained interest among researchers due to its unique optical, electrical, and mechanical properties which suitable for various applications such in gas sensors, superconductors, photocatalysis and optoelectronic devices (Chauhan *et al.*, 2016; Kulkarni *et al.*, 2015). There are numerous nanomaterials from semiconducting metal oxides have been used for the fabrication of gas sensors such as zinc oxide (ZnO) (Spencer, 2012), titanium dioxide (TiO₂) (Shimizu *et al.*, 2002), tin oxide (SnO₂) (C. Liu *et al.*, 2015), indium oxide (In₂O₃) (Lai *et al.*, 2012) and nickel oxide (NiO) (C.-Y. Lee *et al.*, 2007). These materials served as gas sensitive elements in which their properties such as conductance change upon the adsorption of gas molecules on their surface (Suchorska-Woźniak *et al.*, 2016).

ZnO is one of the most widely used materials for gas sensing applications due to its advantageous in terms of good chemical stability, electrical compatibility, biocompatibility and high electron transfer properties (Anusha *et al.*, 2014). ZnO is a n-type semiconductor which has direct and wide band gap energy of 3.37 eV and a large exciton binding energy of 60 meV (Patil *et al.*, 2016). A simple, low cost and environmental friendly fabrication process of ZnO make it one of the popular choices among researchers (Saidin *et al.*, 2018). It also has a good optical transparency in visible spectrum which makes it useful for short wavelength optoelectronic applications (Ruchika, 2015; Shinde *et al.*, 2008; C.-F. Tang *et al.*, 2008), resonators (Cao *et al.*,

1998), biosensors (Chang *et al.*, 2010; Kong *et al.*, 2009; Kumar *et al.*, 2008) and medical devices (Rasmussen *et al.*, 2010).

In optical based gas sensing application, the detection appears by the interaction of electromagnetic radiation of light rays to gas molecules which has specific properties (Rafis *et al.*, 2017). Numerous methods can be utilized in gas detection analysis (Sberveglieri, 2012), still absorption spectroscopy is one of the reliable method and commonly used in optical gas sensing (Kraft, 2006) such as in detecting oxygen (O₂) (Vanheusden *et al.*, 1996), carbon dioxide (CO₂) (Samarasekara *et al.*, 2007), ammonia (NH₃) (Dikovska, Atanasov, Andreev, *et al.*, 2007; Renganathan *et al.*, 2011), methane (CH₄) (P. Bhattacharyya *et al.*, 2007) and butane (C₄H₁₀) (Dikovska, Atanasov, Tonchev, *et al.*, 2007). Apart of gasses detection, the same absorption spectroscopy concept can also be applied in the detection of humidity and various chemical vapors such as formaldehyde or alcohols (ethanol, methanol and isopropanol).

Humidity monitoring is important in many fields to ensure a better quality of life. According to Malaysia Industry Code of Practice on Indoor Air Quality (2010) (Arifin *et al.*, 2015), a normal humidity level of indoor environment should be within the range of 40% to 70% in order to minimize the spread of viruses and bacteria (Alsmo *et al.*, 2014). In critical applications, it could lead to devastating outcomes if not efficiently monitored. For example, in huge structures such as airplanes, humidity monitoring is essential in evaluating the risk of leakage due to corrosion (Ghadiry *et al.*, 2016) that can lead to degradation of metallic components and failure of electronic systems (Shukla *et al.*, 2015).

1.3 Problem Statement

ZnO nanorods has been a significant technological material widely used in humidity sensing, piezoelectric based sensors and mechanical actuators (Baruah *et al.*, 2009b; Farahani *et al.*, 2014; Horzum *et al.*, 2011; Narasimman *et al.*, 2017). Optimization of the growth process and the coating area are crucial to enhance the sensitivity, and system performance, which leads to the reduction in the complexity of signal detection and analysis. The growth of ZnO nanostructures have been extensively reported in the literature mainly based on optimizing the synthesis parameters such as growth duration (Apiwattanadej *et al.*, 2015; Haque *et al.*, 2013), growth temperature (Hambali *et al.*, 2014), concentration alterations (Emphasis *et al.*, 2015) and solvents variation (Tsay *et al.*, 2010). Although the optimization works on ZnO synthesis process indicates that the maximum sensing response was observed according to their specific optimum growth parameters, there are still inconsistencies in terms of optimum growth conditions related to the performance between the fabricated devices. For instance, the optimum growth time of ZnO nanorods on the surface of optical fiber for the maximum light coupling efficiency was varied between the research works which reported at 5 h (Fallah *et al.*, 2013), 8 h (Bora *et al.*, 2014) and 12 h (Rahim, Manjunath, *et al.*, 2016). These variations definitely affect the performance of sensing devices where the sensing response would differ between one fabrication batches to another.

Two major factors that influence this uncertainty are uniformity of the coatings and repeatability of coating structures. As a sensor device, the sensing surface area is one of imperative factor that influence the sensitivity of a sensing device as discussed earlier. Uniformity of nanomaterial coatings guarantees a consistent sensing response throughout the surface. The reduction of the rough surface due to good uniformity of the coatings make the device suitable for being utilized as transducers, particularly in optoelectronic applications (Haarindradas *et al.*, 2015). Despite the fact that a

uniform coating is achievable, repeatability of the nanomaterial structures is another factor that affects the consistency of the fabricated sensor performance. Due to the sensitivity of growth processes the physical of nanostructures (e.g. length or cross-sectional area of nanorods) grown under similar growth parameters (concentrations, growth time or temperature) may not necessarily be achievable at all times. Also, the optimization of the effective area of the ZnO coating in combination with growth time may not be possible to be repeated synonymously leading to variations in batch to batch fabrication processes since minor variations in the process could lead to dramatic changes in material properties (Uskokovic, 2013).

Thus, the optimization of ZnO nanostructure growth and effective sensing surface area may not be an effective way to determine the maximum sensing response of sensor devices. In retrospect, the analysis of optimum operating conditions of fabricated sensor device delivers promising sensing device performance regardless of growth conditions or surface coverage. This brings up the motivation in exploring a new approach for a standard reference in designing a sensing device which independent to a specific growth conditions. This implies, as long as any fabricated sensor device meets the optimum operating conditions, the device would produce best sensing performance.

This research work was also driven by the initiative in developing a simple and cost effective optical sensing device. In spite of the fact that optical humidity sensors have a lot of advantages over electronic based transducers, the use of expensive equipment in the sensing setup often limits its wide-spread application. Recently, Harith *et al.* (Z Harith *et al.*, 2017) presented tapered plastic optical fiber coated with seeded aluminum doped zinc oxide (ZnO:Al) materials for humidity detection utilizing a He-Ne laser source, a photodetector and lock-in amplifier. Aneesh *et al.* (Aneesh *et al.*, 2011) reported the use of a laser source, photodetector and data acquisition cards

coupled to computers for data storage. In other work, Liu *et al.* (Yanjuan Liu *et al.*, 2012) demonstrated humidity measurement using a 644 nm laser source and optical power meter alongside a silica fiber coated with zinc oxide nanorods. Typically all the reports in the literature describe optical humidity sensors requiring high grade equipment such as laser source, photodetector and optical power meter, which are not optimum for large scale implementation of optical sensors for humidity monitoring. In order to increase the commercial deployment of sensors, the cost of fabrication, operation and ease of deployment of the sensor device needs to be considered.

1.4 Objectives of the Research

The aim of the study is to develop a simple and low cost integrated zinc oxide based sensing device. To achieve this, the following objectives have been outlined:

1. To fabricate ZnO nanorods coating onto glass substrate for optical investigation of growth duration and coating length effect.
2. To theoretically and practically maximize the optical dynamic range by controlling ZnO nanorods growth conditions on glass substrate towards humidity sensing.
3. To develop and experimentally validate an integrated zinc oxide nanorods based sensing device towards humidity and formaldehyde vapor concentrations.

1.5 Limitation of the Research

The research work was focused on the development of sensing device based on the analysis on optical dynamic range maximization. A cosmetic works such as casing, dedicated printed circuit board design or graphical user interface (GUI) for the developed sensor device are not covered in this research.

As the cutting process of the glass substrates were performed manually by using glass cutter, small variation in the dimension of the glass substrates was expected. Besides, smooth edge surfaces of the glass substrates were difficult to achieve and the cutting process needs to be performed carefully to obtain the surface as smooth as possible. As the masking process of the glass substrate was done by using Polytetrafluoroethylene (PTFE) tape, the dimension of ZnO nanorods coating area may not have achieved as precise as desired.

1.6 Thesis Organization

This thesis consists of six chapters demonstrating the development of integrated zinc oxide nanorods coated glass substrate sensing device. **Chapter 1** explains the introduction regarding the research background and problem statements. The objectives and limitation of the research are also highlighted in this chapter.

Chapter 2 presents a literature review on related research topic. This includes the discussion about the flat surface as propagation medium, the role of ZnO nanorods in sensing application, the hydrothermal growth and structure of ZnO nanorods. The recent research on the humidity and formaldehyde sensing are also presented in the chapter.

Chapter 3 explains in detail the fabrication process of ZnO nanorods coating on glass substrate. The optical characterizations on the effect of growth conditions of the fabricated ZnO nanorods are also discussed in the chapter.

Chapter 4 presents the theoretical model of the dynamic range maximization of the fabricated sensor towards humidity sensing application. An experimental analysis was performed for the correlation with theoretical model.

Chapter 5 demonstrates the development of the integrated zinc oxide based sensing device. The final developed sensing device is presented and characterized with humidity sensing experiment. The sensor device is also validated with formaldehyde vapor concentrations as additional sensing application.

University of Malaya

CHAPTER 2: LITERATURE REVIEW

2.1 Introduction

Optical sensing was started in 16th century based on absorbance, emissive and fluorescence methods (Mário *et al.*, 2017). Since then, the evolution of optical sensor emerged by the introduction of the first laser in 1960s (Fidanboylu *et al.*, 2009) and the development of low-loss optical fibers in 1970s (Grattan *et al.*, 2000). The technology of optical fiber sensor has significantly developed in the field of optical fiber communication and optoelectronic industries (Sabri *et al.*, 2013). The employment of optical fiber as sensing device was found in numerous sensing applications such as in natural structures (Udd *et al.*, 1994), medical (Griffiths *et al.*, 1999), chemical (Stewart *et al.*, 1997; Xiong *et al.*, 2014), biological species (Ferguson *et al.*, 1996; Healey *et al.*, 1997; Wolfbeis, 2008), environmental condition (Dietrich *et al.*, 1997; H. Jiang *et al.*, 2013) and many other physical parameters (Udd *et al.*, 2011). The utilization of the optical fiber as light-guiding medium offers excellent features for developing a good sensor device such as corrosion resistance due to non-metallic component parts, small in size, stability due to no moving parts and ability for long distance or remote sensing application (Culshaw, 2015). Optical fiber sensors can be distinguished into two categories which are extrinsic and intrinsic sensors (Connelly, 2004). The difference between the two is the sensing location where the extrinsic type uses external optical device (light modulator) for the sensing while intrinsic carries the sensing by optical fiber itself (Connelly, 2004; Fidanboylu *et al.*, 2009; Udd, 1995) as illustrated in Figure 2.1. Nevertheless, both types of sensor employ the same concept of light propagation which utilizes optical fiber as a medium to carry light from its source and to a detector.

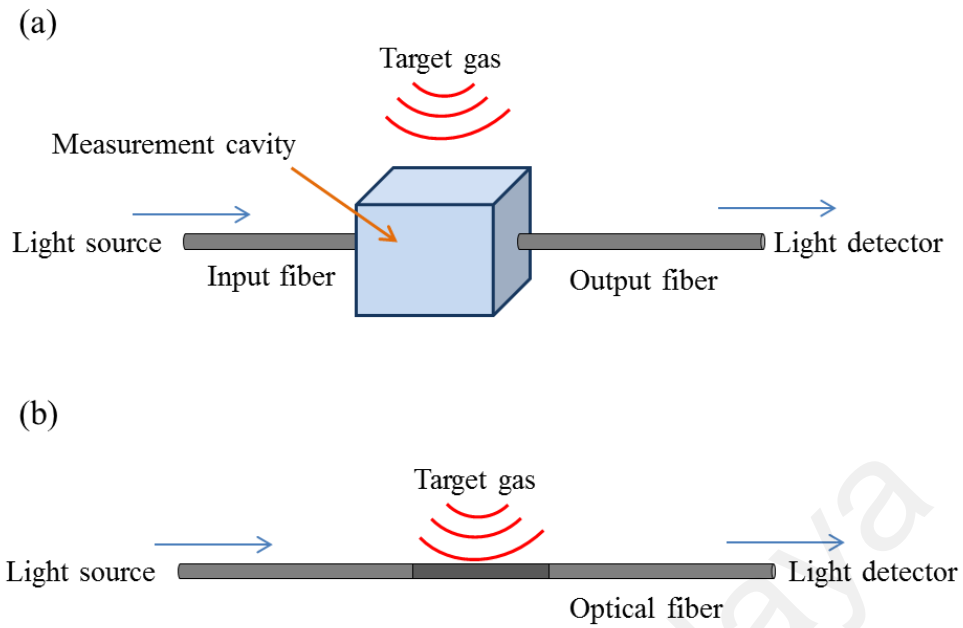


Figure 2.1 Types of optical fiber sensors. (a) Extrinsic. (b) Intrinsic.

This thesis aims to develop a simple and low cost integrated zinc oxide based optical sensing device. In this chapter, a thorough literature review is presented on the related research topic. This includes the discussion about the flat surface as propagation medium, the role of ZnO nanorods in sensing application, the hydrothermal growth and structure of ZnO nanorods. The recent research works on the humidity and formaldehyde sensing are also discussed. At the end of this chapter, Arduino is introduced as data acquisition platform for the sensing device.

2.2 Concept of Light Propagation

Light propagation is the process of energy transfer of an electromagnetic wave from one point to another. Lights can be propagated either through space or various medium. Light travels at the speed of 3.00×10^8 m/s in a vacuum. The propagation of light through any medium would observe at the speed of less than in a vacuum due to

the process of absorption and reemission of the wave by the atom of the medium. The medium density determines the effective speed of electromagnetic wave travels through the medium. In other words, different materials have different rate of speed thus affect the amount of delay for the electromagnetic wave travels through the medium. The speed of light travels in a given medium can be explained by the index of refraction, n which is given by

$$n = c/v \quad (2.1)$$

where c and v is the speed of light in a vacuum and any given medium, correspondingly. This expression explains that the speed of light that travels in a vacuum is n times of the speed as it travels through the medium. Generally, as the light is launched into a transparent or semi-transparent medium, it encounters three mechanisms; transmission, reflection and refraction at the interface of two media as described in Figure 2.2.

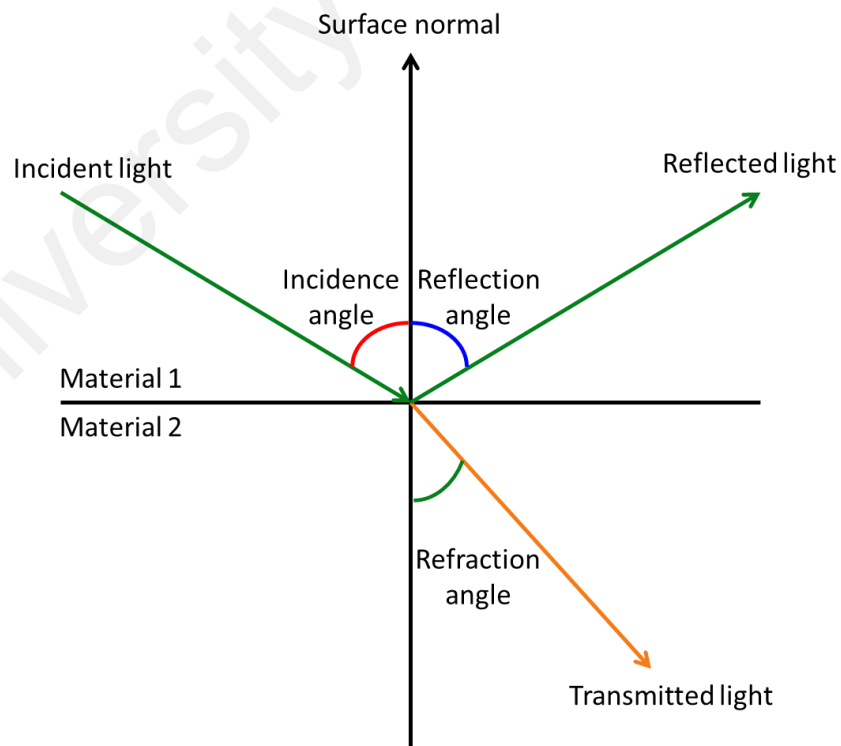


Figure 2.2 Light propagation at interface between two different media.

Transmission is defined by the part of light that can be transmitted through a medium. The amount of light passes through the medium is subjected to attenuation of light by the medium properties. Lambert's and Beer's law stated that the absorbance of a given medium is directly proportional to its thickness (length of path) and concentrations of the absorption species in the medium, correspondingly. Therefore, Beer-Lambert law expressed the transmittance of light in a medium as

$$T = e^{-\alpha x} \quad (2.2)$$

where α is attenuation coefficient and x is the length of the path for the light travel in the medium. The transmitted light will not bend when the incident light is normal to the interface and part of normal ray will be reflected at normal reflection coefficient. However, at any angle of incident light, the transmitted light will be refracted at certain angle depending on the density of the material. This phenomenon is called refraction.

Refraction is interpreted as the change in direction when light travels from one medium to another. For example, when light enters a medium that has higher refractive index from its origin, the light is refracted towards the normal. The angle of bending light at the interface is described by Snell's Law as

$$\frac{n_1}{n_2} = \frac{\sin\theta_2}{\sin\theta_1} \quad (2.2)$$

where the n_1 and n_2 are the refractive index of two mediums while θ_1 and θ_2 are the incident angle and refractive angle respectively. The equation explains that if the incident medium has larger refraction index, then the angle to the normal is decreased by refraction. This concept is used in the operation of a fiber optic cable.

Generally, optical fiber is made up by several layers which are the core, cladding and buffer as illustrated in Figure 2.3 (J.-R. Lee *et al.*, 2011). In the optical fiber

operation, light travels through the core while it covered by a cladding layer which served as reflector to bounce back the light to the core. The buffer served as protection for the fiber cable from wear and tear.

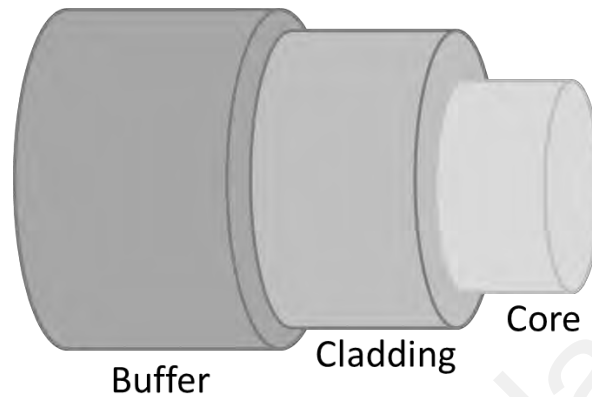


Figure 2.3 Structure of optical fiber cable.

In an optical wave guiding concept, it is known that the variation of refractive index between two medium has to be achieved. In the case of optical fiber, the refractive index of the core has to be higher than the one in cladding. In this condition, when the light travels from higher to lower dense of the medium, it refracts away from the normal. At certain incident angle, a phenomenon called total internal reflection is achieved where total amount of light is completely reflected in the original medium (Cherin, 1983; Hentschel *et al.*, 1983; Keiser, 2010). This angle is called critical angle. Critical angle is the minimum angle required for the incident light in order to be reflected completely in the medium. Figure 2.4 shows that any light travels at incident angle (θ_i) greater than critical angle (θ_c) will be fully reflected internally into the medium from which it originated. This concept can be also applied in any other waveguide medium such as glass substrate.

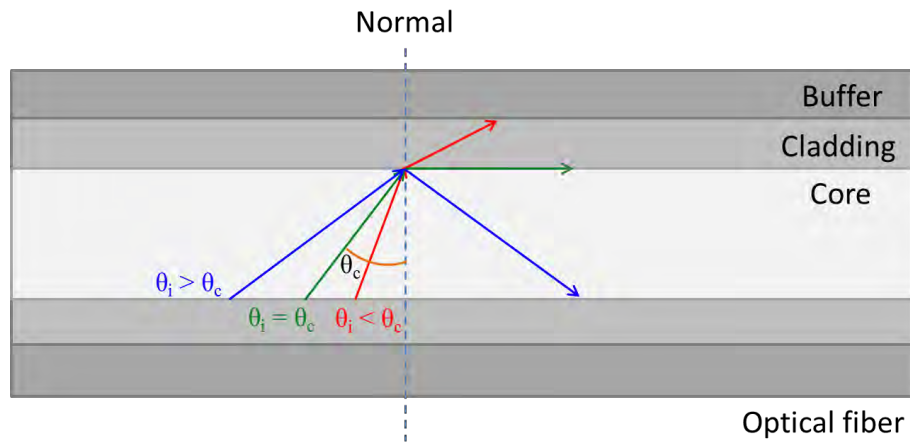


Figure 2.4 Concept of light propagation inside an optical fiber.

2.3 Flat Surface Glass Substrate as Light Propagation Medium

Similar to the characteristic of an optical fiber, glass substrate can be used as a medium to propagate light through it. The same concept of total internal reflection is applied by considering a normal glass substrate with refractive index of 1.50. In normal air condition, the glass substrate is surrounded by lower refractive index ($n_{air} \sim 1.00$). According to Snell's Law, the critical angle at the glass-air interface is calculated to be approximately 41.81° . Therefore, fully guided light in the glass substrate can be achieved as long as the angle of incident light is greater than the mentioned critical angle as shown in Figure 2.5.

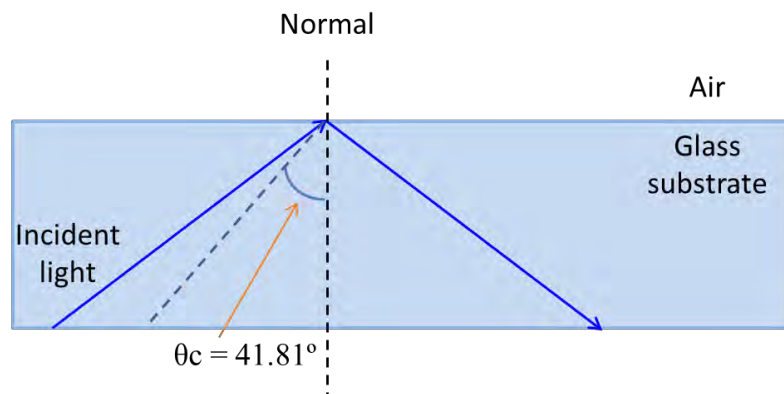


Figure 2.5 Total internal reflection at glass-air interface.

Flat surface glass substrate offers several advantages especially in the application of optical sensor. Due to its flat surface, it does not have bending loss which exists in the optical fiber (Salleh *et al.*, 2015). Bending in fiber cable contributes to reduction of the fiber performance (Yu *et al.*, 2012). In a multimode optical fiber, curvature of the cable causes the reduction of the modes propagating in the fiber (Semenkoff, 1992). As a result, the power at the output fiber is reduced. The variation of output power may be observed due to bending when the cable is not appropriately fixed. This would affect the performance of sensing measurement when it is used as a sensor device. In addition, flat surface glass structure provides a stable platform for light to propagate through it thus ensure a consistent amount of power transferred from one point to another. In nanomaterial based optical sensor, surface of sensing platform plays an important role on sensing performance. ZnO based optical sensor for instance, growth of nanostructures is better on flat surface compared to curvature or cylindrical. It is easier to control the morphological parameters of the nanostructures such as uniformity, alignment and density (Rafis *et al.*, 2017). Good uniformity of nanomaterial coating on flat surface ensures a consistency of sensing response of sensor device.

There are three types of glass commonly used in laboratory for research purposes. They are borosilicates, soda-lime silicates and phosphates, which have different chemical composition. Borosilicate glasses are made up of SiO_2 and B_2O_3 . It has very good thermal shock resistance among others. Besides, these types of glasses are durable with high abrasion and chemical resistance. Soda-lime silicate glasses are composed of SiO_2 , Na_2O and CaO . The addition of calcium and sodium oxide weakens the network connectivity properties. Therefore, the glass is easier to melt and form than the borosilicate glasses. Phosphate glasses are the weakest among the rest. They are made up by P_2O_5 which having weaker bonds than the other two. The melting point for this type of glass is much lower. Nevertheless, all the glasses discussed above have

excellent transmission of light at UV, visible and near-IR wavelengths (KOPP-Glass, 2016). Table 2.1 summarizes the comparison of properties between the glasses and other transparent materials. The characterization of refractive index of an optical glass is usually performed in the middle range of visible spectrum which typically at 587.56 nm and many cases is at 546.07 nm (SHOTT, 2016).

Table 2.1 Properties comparison between the transparent materials (KOPP-Glass, 2016).

Property	Unit	Boro-silicate	Soda-lime silicate	Phosphate	Quartz	Acrylic	Poly-carbonate
Transmission	-	UV-nIR	UV-nIR	UV-nIR	UV-nIR	UVA-nIR	Vis-nIR
Refractive Index	-	1.51	1.52	1.55	1.46	1.49	1.58
Density	g/cm ³	2.23	2.52	2.86	2.20	1.2	1.2
Tensile Strength	MPa	70	40	65	70	70	75
Hardness	Moh's	5.5	5.5	5	6	3	3
Young's Modulus	GPa	65	70	60	72	3	2
Coefficient of Thermal Expansion	E ⁻⁷ /°C	33	80	100	5	720	650
Annealing Temperature	°C	560	525	525	1400	-	-
Operating Temperature	°C	410	410	350	790	70	130
Abrasion Resistance	-	High	Med	Med	Very High	Med	Med
Impact Resistance	-	Med	Med	Med	Med	High	High
Chemical Resistance	-	High	Med	Low	Very High	Low	Low
UV Resistance	-	High	High	High	High	Med	Low

2.4 Glass Substrate in Sensing Application

Glass substrates provide an efficient and cost effective medium to serve as a sensor device. Compare to optical fiber, glass substrates can be formed in any dimension to suit a specific sensing application. The thermal, mechanical, chemical and optical properties discussed earlier show that glass substrates can be adapted to wide sensing application such as temperature, chemical vapor, humidity, gas, vibration and others. Surface plasmon resonance (SPR) based sensor is one of the example in which glass substrate is utilized as a sensing medium. SPR has become an influential optical biosensing technology since its first introduction of real-time biological system analysis in 1990s (Y. Tang *et al.*, 2010). Wide range of biotechnological applications can be applied by using SPR technique. This includes immunological analysis, studies of protein interaction, screening of new ligands and examination of binding kinetics (Silin *et al.*, 1997). SPR is a process where plane-polarized light hits a thin metal film under total internal reflection conditions (BiacoreAB, 1994). Generally, a collimated and polarized light beam is used to excite a surface resonance as illustrated in Figure 2.6 with a gold thin film is deposited on a glass substrate (Parisi *et al.*, 2008).

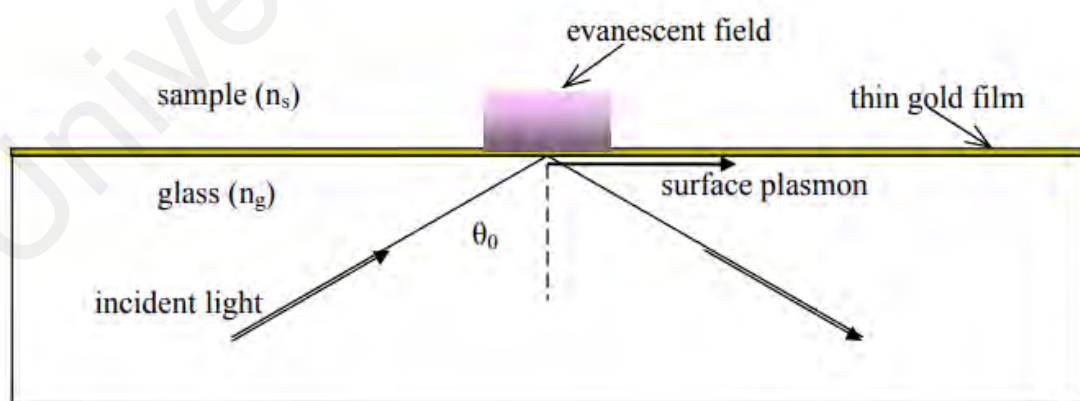


Figure 2.6 Basic setup for the excitation of surface plasmons by means of a beam light (Parisi *et al.*, 2008).

The operating principle of optical sensor can be classified into three types. They are intensity based, phase based and polarization based (Gholamzadeh *et al.*, 2008) sensing as shown in Figure 2.7. These operating principles are based on modulation of light characteristics in response to physical parameters being measured. Intensity based optical sensor is the simplest type of sensing mechanism among the three listed. It measures a change in intensity of transmitted light where it requires simple sensing setup which usually a light is injected at one end of an optical fiber cable and measured at the other end of the cable. On the other hand, polarization and phase based sensing method require complex sensing setup to measure different polarization directions and phase change of the transmitted light, respectively (Gholamzadeh *et al.*, 2008). Due to simple sensor setup and uncomplicated operation of sensing, intensity based is a popular choice especially in developing a cost-effective sensing device (Medlock, 1987).

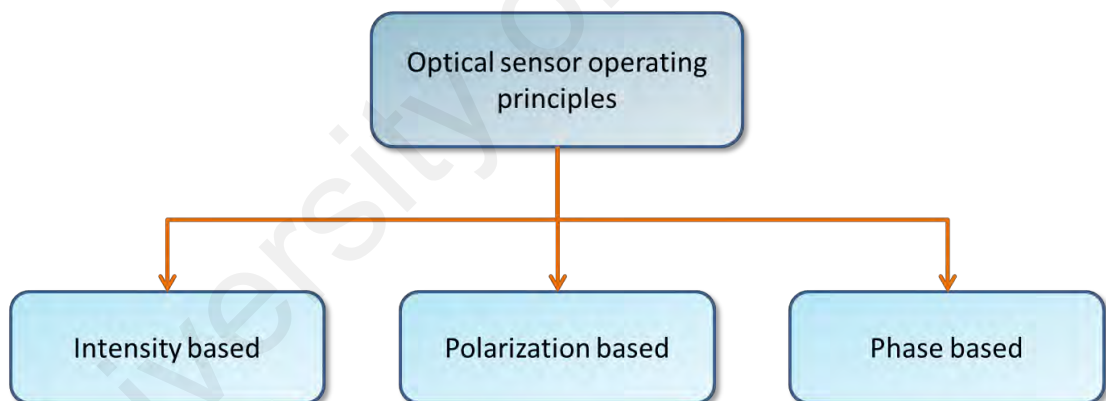


Figure 2.7 Classification of optical sensor operating principles.

2.5 Intensity Modulation Based Sensors

Intensity modulation (IM) based sensor is one of widely used in optical sensing applications due to its simplicity, reliability and cost effective method compared to others (Medlock, 1987). The measurement of this type of optical sensor is based on the modulation of transmitted light intensity through an optical medium upon exposure to

measurand. The change of light intensity is measured by a suitable detector placed at the end of the medium (Kalyani *et al.*, 2016). Both categories either intrinsic or extrinsic optical sensors utilize this method in which various sensing mechanism such as micro-bending loss, attenuation and evanescent field can be applied to produce measurand-induced change in optical intensity (Fidanboylu *et al.*, 2009).

Micro-bending is one of the popular methods used in intensity modulation-based sensor. Basically, this type of sensor consists of two grooved plates where an optical fiber is placed in between of both plates as shown in Figure 2.8. A light source is connected at one end of the fiber while the other end was connected with a light detector. The bottom plate is stationary while the upper plate moves towards the fiber in response to pressure causing the fiber to bend. When the bending radius exceed the critical angle needed for the light to stay in the core, the light starts to leak into cladding thus modulate the intensity of light before being captured by the detector (Berthold, 1995).

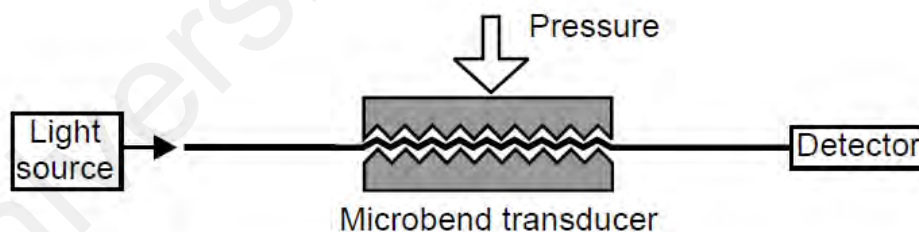


Figure 2.8 Micro-bending based fiber sensor (Connelly, 2004).

Evanescent wave sensor is another type of intensity-based fiber optic sensors which were widely used in chemical sensors. The concept of this sensor is by utilizing the light energy that leaks out from the core. There are several method can be used in order to accomplish the sensing mechanism such as by removing certain region of the

cladding (Khijwania *et al.*, 2005a; Smrithi *et al.*, 2015) or side-polishing (Gaston *et al.*, 2003; Ribeiro *et al.*, 2002) the fiber. Figure 2.9 shows an optical fiber sensor, which was constructed based on evanescent wave method. In the sensor, the cladding of the fiber is stripped to leave only the bare core to be exposed to measurand so that the changing in light intensity is observed depending on the concentrations of the chemical. This sensing method relies on the surrounding effective index of the fiber core. As the cladding was stripped off from the fiber, the core is now depending on the refractive index of surrounding environment (Khijwania *et al.*, 2005a). In the presence of different concentrations of humidity or chemical vapors surrounding the fiber core, it modifies the refractive index of the environment thus modulate the output from the fiber.

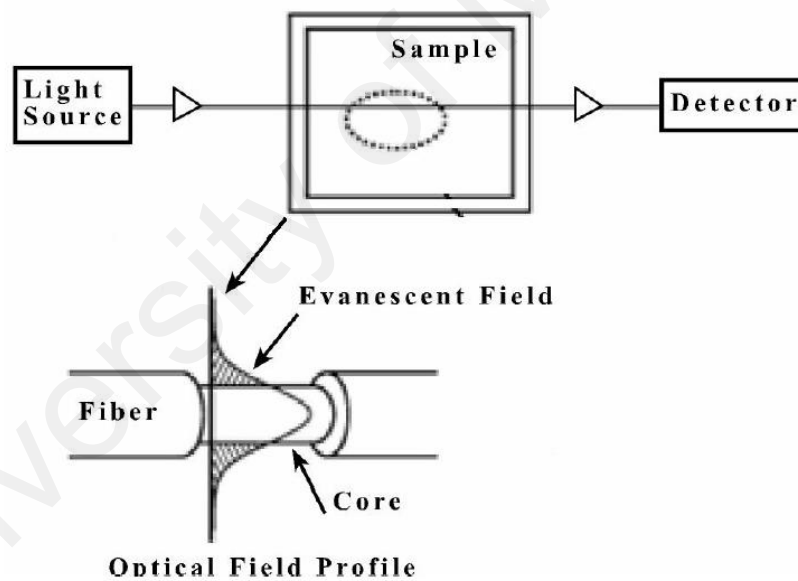


Figure 2.9 Evanescent wave optical fiber sensor (Fidanboylyu *et al.*, 2009).

A similar method can be performed by replacing the cladding with a sensitive material that has optical properties which can be altered by chemical under testing (Fidanboylyu *et al.*, 2009). In the presence of chemical vapors for instance, the complex refractive index of the material coated on the core surface changed due to adsorption

process by the material (Khalil *et al.*, 2004). As a result, this changes the optical scattering patterns of the fiber which leads to light modulation. The material such as zinc oxide (ZnO), tin oxide (SnO₂) or tungsten oxide (WO₃) are commonly used as gas sensitive elements due to its capability in changing its properties upon adsorption of gas molecules on its surface (Suchorska-Woźniak *et al.*, 2016). When these materials are coated on fiber core surface, it acts as a cladding to the core. These materials can be having lower or higher refractive index than the core. If the refractive index is lower, the total internal reflection is met and the intensity modulation of the sensing is depending on the light absorption of the evanescent field in the cladding (Elosua *et al.*, 2006; Yuan *et al.*, 2003). If the refractive index is higher than the cladding, part of a guided light will be reflected in the fiber while some portion of it will be refracted into cladding which transferred into radiation modes (Yuan *et al.*, 2003). In this condition, total internal reflection does not occur in the modified cladding or coated region. When a material with a good optical transparency used as the coating layer on the exposed core surface, the refraction light from the core radiates through the materials which results the reduction of light intensity captured at the output. ZnO nanorods is one of the material that having higher refractive index ($n_{ZnO} \sim 1.9 - \sim 2.1$) than the core of optical fiber ($n_{core} \sim 1.5$) (Bora *et al.*, 2014). ZnO nanorods has been widely utilized together with optical fibers for environmental sensing applications such as humidity (Zuraidah Harith *et al.*, 2015), alcohol vapors (Rahim, Lokman, *et al.*, 2016), CO₂ (Samarasekara *et al.*, 2007) and NH₃ (Renganathan *et al.*, 2011). ZnO demonstrates good material properties which make it suitable for various applications especially when used as sensing active material (Chauhan *et al.*, 2016).

2.6 Zinc Oxide Crystal Structure

ZnO possesses hexagonal wurtzite structure establishing partial polar characteristics with lattice parameters $a = 0.3296$ nm and $c = 0.52065$ nm (Z. L. Wang, 2004). Figure 2.10 illustrates the structure of ZnO crystal which made up from tetrahedrally coordinated O^{2-} and Zn^{2+} stacked alternately along c-axis where a tetrahedral unit is formed by oxygen anions and zinc cations. This coordination produces the properties of piezoelectric and pyroelectric due to inexistence of inversion symmetry. Basal plane (0001) is the most common polar surface in ZnO crystal which both ends of the basal polar planes terminates with partially positive Zn and partially negative oxygen lattice sites, respectively. The opposite charged ions of Zn(0001) and $O(000\bar{1})$ resulting a normal dipole moment and alteration in surface energy (Baruah, 2011; Z. L. Wang, 2004). ZnO $\pm(0001)$ surfaces are generally atomically flat, stable and exhibit no reconstruction (Y. Chen *et al.*, 2000; Emanetoglu *et al.*, 1999). The other two non-polar facets of ZnO; $(2\bar{1}10)$ and $(01\bar{1}0)$ which commonly observed of having lower surface energy than(0001).

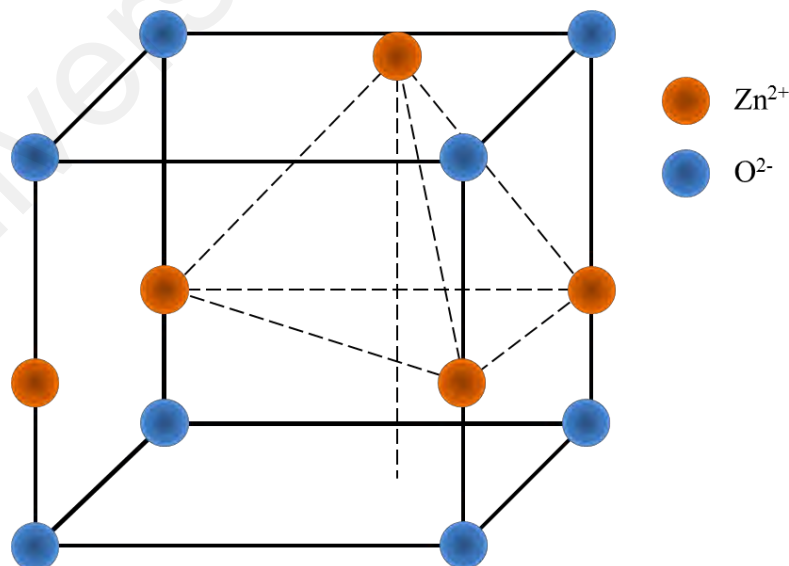


Figure 2.10 Wurtzite structure of ZnO.

ZnO has been implemented in various applications such as in photodetectors, gas sensors, photonic crystals, optical modulator waveguides, light emitting diodes, photodiodes and solar cells (Yi *et al.*, 2005). ZnO has good transparency optical properties especially for visible wavelength range (Ruchika, 2015; C.-F. Tang *et al.*, 2008) and its wide bandgap energy which is 3.37 eV (Patil *et al.*, 2016) makes ZnO suitable for optoelectronic applications. ZnO also permits efficient excitonic emission at room temperature due to its high exciton binding energy (60 meV) (Fonoberov *et al.*, 2006; Patil *et al.*, 2016; Schmidt-Mende *et al.*, 2007). In ceramic industry, ZnO plays an important role because of its hardness and rigidity, less toxicity, biocompatibility and biodegradability (Rafis *et al.*, 2017). This makes ZnO one of the best materials to be used in biomedicine and pre ecological systems (Kołodziejczak-Radzimska *et al.*, 2014). Table 2.2 shows the detail properties of ZnO.

Table 2.2 Properties of ZnO (Baruah, 2011)

Crystal structure	Hexagonal wurtzite
Lattice constant	a=3.264 Å, c=5.207 Å
Molecular weight	81.38
Density	5.67 g/cm ³
Refractive index	2.008
Electron and hole effective mass	m _e [*] = 0.28 m ₀ , m _h [*] = 3.75 m ₀
Cohesive energy	1.89 eV
Band gap at room temperature	3.37 eV
Exciton binding energy	60 meV
Piezoelectric coefficient	12 pC/N
Pyroelectric constant	6.8 A/s/cm ² /K x 10 ¹⁰
Dielectric constant	ε _r = 8.75, ε _∞ = 3.75
Thermal conductivity	25 W/m.K at 20 °C
Thermal expansion coefficient	4.3x10 ⁻⁶ /K at 20 °C and 7.7x10 ⁻⁶ /K at 600 °C
Melting point	1975 °C (3587 F)
Debye temperature	370 K
Heat of fusion	4,470 cal/mole
Lattice energy	964 kcal/mole
Solubility	1.6 mg/L at 30 °C
Standard enthalpy of formation	-348.0 kJ/mol
Standard molar entropy	43.9 J · K ⁻¹ mol ⁻¹

ZnO structure can be grown in several forms such as one dimensional (1D), two dimensional (2D) and three dimensional (3D) structures. The largest group of structure

formation in 1D ZnO includes nanorods, helices, needles, rings and springs (Banerjee *et al.*, 2003). In contrast with 2D where the growth of ZnO structures are more into the form of nanoplates/nanosheets and nanopellets (Chiu *et al.*, 2010). On the other hand, 3D form of ZnO usually grown in different structures such as nanowires (Shan *et al.*, 2008), nanorods (Dedova *et al.*, 2007), snowflakes (Jing *et al.*, 2012) and nanoflowers (Miles *et al.*, 2015) as shown in Figure 2.11.

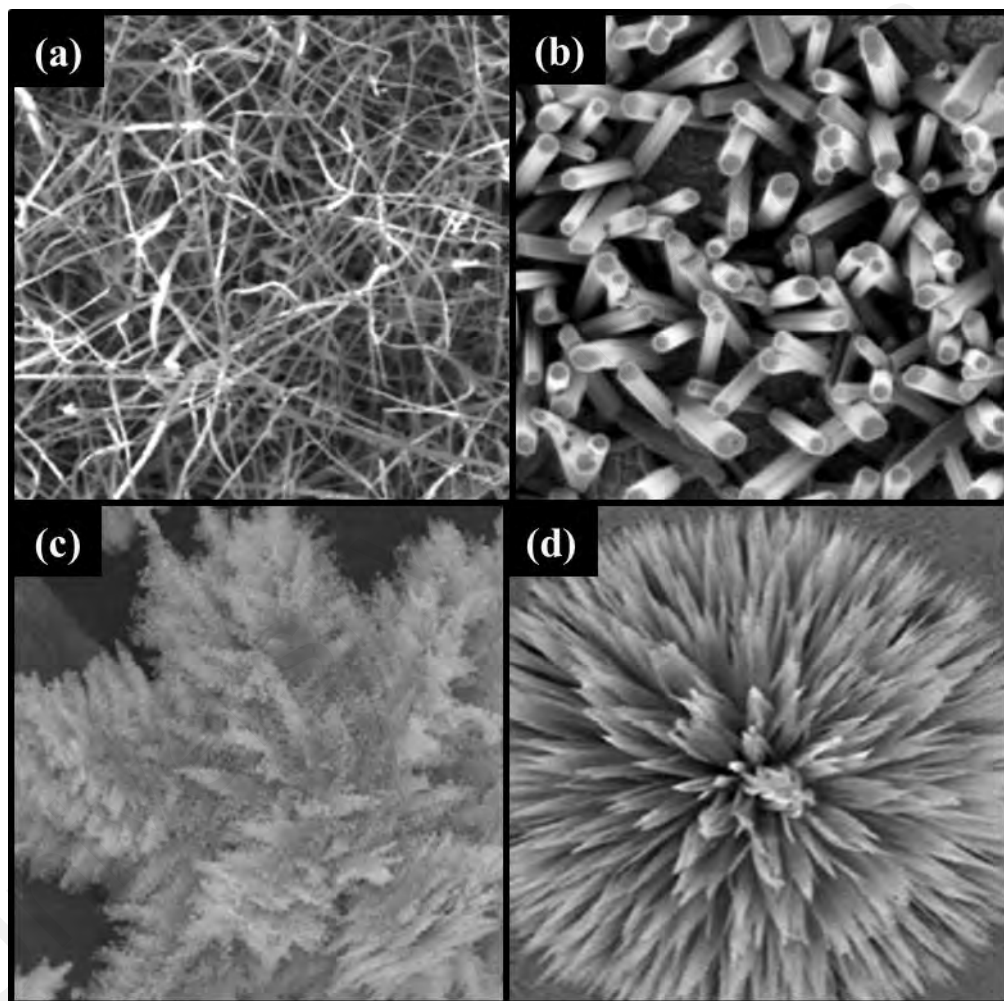


Figure 2.11 ZnO structures (a) nanowires (Shan *et al.*, 2008), (b) nanorods (Dedova *et al.*, 2007), (c) snowflakes (Jing *et al.*, 2012) and (d) nanoflowers (Miles *et al.*, 2015).

Novel structures of ZnO can be fabricated in various form by tuning the rate of growth along three fast growing direction: $\langle 2\bar{1}\bar{1}0 \rangle$ ($\pm[\bar{1}2\bar{1}0]$, $\pm[2\bar{1}\bar{1}0]$, $\pm[\bar{1}\bar{1}20]$); \langle

$01\bar{1}0 > (\pm[01\bar{1}0], \pm[10\bar{1}0], \pm[1\bar{1}00])$ and $\pm[0001]$ (Baruah, 2011). Different crystal planes have its different kinetic energy which emphasized under controlled growth conditions. Therefore, a crystallite will form into a 3D structure after the first moment of nucleation and growth process. Figure 2.12 shows typical growth morphologies of 1D ZnO structures. Depending on the corresponding facets, the formation of ZnO structures can be either in the form of nanowire/rod, polar nanobelt, nanobelt type A or nanobelt type B as illustrated in Figure 2.12(a), Figure 2.12(b), Figure 2.12(c) and Figure 2.12(d) respectively.

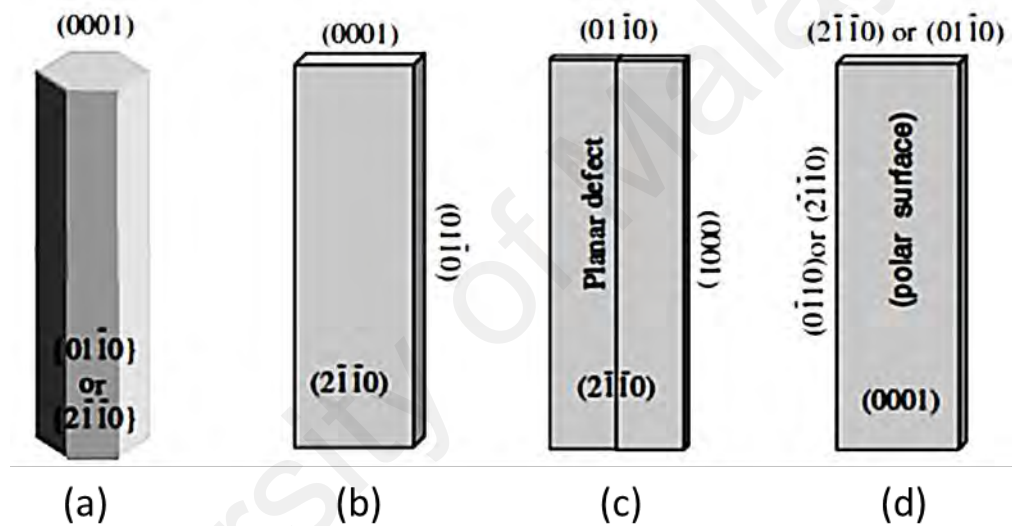


Figure 2.12 Growth morphologies of ZnO structure in the form of (a) nanowire/rod, (b) polar nanobelt, (c) nanobelt type A and (d) nanobelt type B (Baruah, 2011)

2.7 Zinc Oxide Nanostructure via Hydrothermal Synthesis Method

Hydrothermal process in synthesizing ZnO nanoparticles is simple and environmental friendly method as it does not employ organic solvents or additional material process such as grinding or calcination. Research has been reported on the growth of ZnO nanoparticles in alcoholic medium (Baruah *et al.*, 2012). The synthesis of ZnO nanoparticles process in alcoholic medium provides faster nucleation and

growth as compared to water (Baruah *et al.*, 2009b). This synthesis method offers several advantages which include the possibility of performing the synthesis work at low temperature and the diverse shapes and dimensions of the crystals to be growth are depending on the composition of starting mixture, process temperature and pressure. Besides, it also provides high degree of crystallinity and high purity of material (Polsongkram *et al.*, 2008).

Zinc Nitrate Hexahydrate ($\text{Zn}(\text{NO}_2)_3$) is reported in several research as a solution for hydrothermal ZnO nanoparticles synthesis work. $\text{Zn}(\text{NO}_2)_3$ acts as the source of Zn^{2+} ions and the growth was done between 100 °C to 150 °C of temperature. Since hydrothermal process is a solution based method, the acidity or alkalinity of the solution which measured in pH has to be taken into account during the process of growing the ZnO nanoparticles. In previous work, at pH level that less than 11, zinc hydroxide precursors are dissolved partially and ZnO powder is nucleated in a heterogeneous system. However, if the pH level is beyond 11, the zinc hydroxide precursors are completely dissolved and a clear solution is formed with ZnO powder nucleated in homogeneous system (Amin *et al.*, 2011). Figure 2.13 shows the effect of pH level on the growth of ZnO nanostructures. The figure shows that the growth rate increases due to the increases of hydroxyl ions (OH^-) concentration as a result of higher pH level.

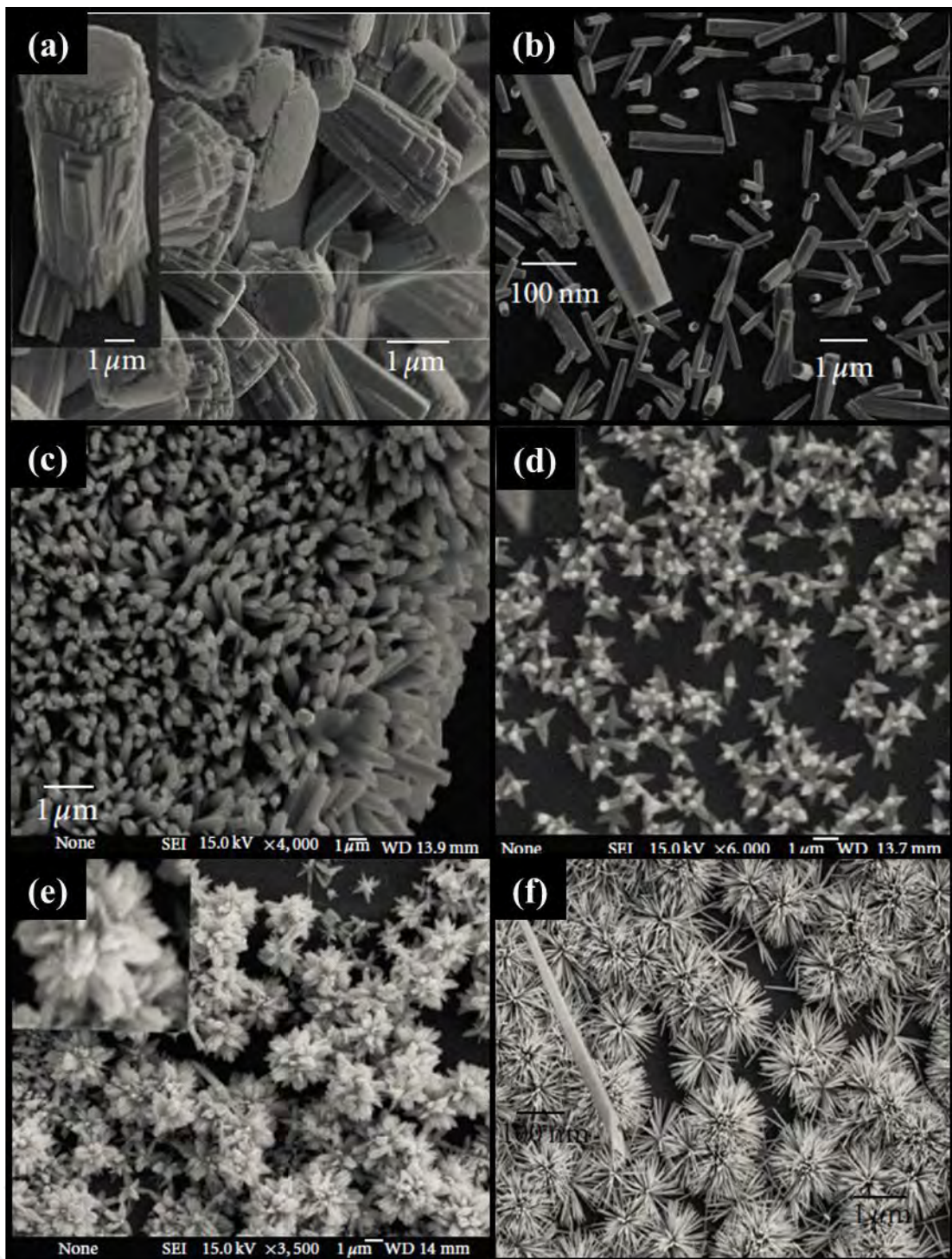


Figure 2.13 Spectral electron microscopy (SEM) images of ZnO nanostructures grown under different solution pH value of (a) 1.8, (b) 4.6, (c) 6.6, (d) 9.1, (e) 10.8 and (f) 11.2 (Amin *et al.*, 2011)

Generally, it is well known that the concentration level of the chemical reactants will affect the desired output. Different level of concentration of chemical reactants during the synthesis process will varies the density, length and diameter of ZnO nanorods. Figure 2.14 shows the effect of different chemical concentration on ZnO nanorod growth. It is very clear that a linear relation can be observed between the incremental of the chemical concentration and the ZnO nanorods dimension. Diameter of the ZnO nanorods shows a significant change where it increases gradually.

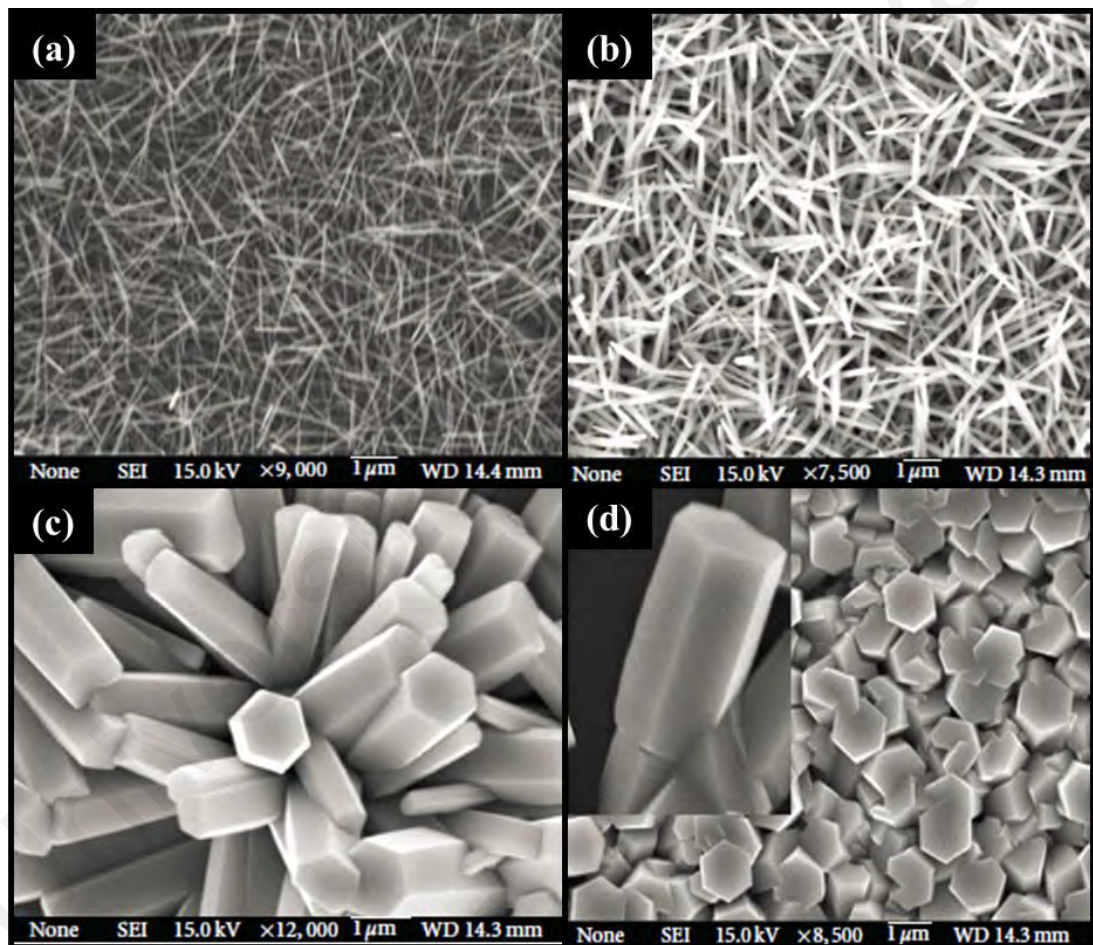
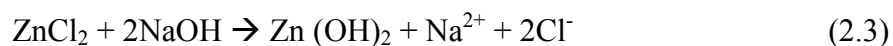


Figure 2.14 SEM images of ZnO nanorods grown under chemical concentrations of (a) 25 mM, (b) 50 mM, (c) 100 mM and (d) 300 mM. (Amin *et al.*, 2011)

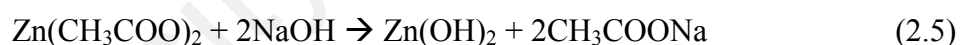
The synthesis of ZnO was carried out by using the reagents of Zinc Chloride (ZnCl_2) and Sodium Hydroxide (NaOH) in a ratio of 1:2 in an aqueous environment (D. Chen *et al.*, 1999). The hydrothermal reaction of the process is expressed as



The white precipitate zinc hydroxide $\text{Zn}(\text{OH})_2$ underwent filtration and washing. Hydrochloric acid (HCl) was used to control the pH in between 5 and 6 followed by heating process in an autoclave with desired temperature. The process subsequently followed by cooling process which the ZnO was then produced as given in equation (2.4)



Ismail *et al.* (AA Ismail *et al.*, 2005) reported another method of hydrothermal process proposed by the following reaction



According to the hydrothermal reaction shown in Equations (2.5) and (2.6), the chemical reaction between $\text{Zn}(\text{CH}_3\text{COO})_2$ and NaOH were carried out in the presence of hexamethylenetetramine (HMT) at room temperature. Based on SEM images, HMT plays a vital role in ZnO particles modification. Besides, the process time and temperature also influence the shape of the particles. It was noted that the size of particles increases when the HMT concentration, process time and temperature increase.

Besides providing hydroxyl ions to carry the precipitation reaction, HMT also performs as a buffer since its hydrolysis rate decreases as the pH increases and vice versa. Sugunan *et al.* (Sugunan *et al.*, 2006) presented a different role of HMT in ZnO

synthesis process. According to the study, the attachment of HMT to the non-polar facets of zincite crystal desirably becomes a long chain polymer and a non-polar chelating agent which resulting an interruption of excess Zn^{2+} ions. This causing the epitaxial growth only happened at the side of polar (0001). Therefore, HMT acts more like a shape inducing polymer surfactant rather than as a buffer as explained earlier. Condition of reaction mixture (zinc acetate, sodium hydroxide and surfactant) affects the morphology of ZnO nanostructures by varying the amount of pH, soft surfactant and ethylenediamine of the solution. The mixture with pH of 12 performed a homogeneous growth of ZnO while it becomes inhomogeneous when the number of pH reduces.

A research by Mahmood *et al.* (Mahmood *et al.*, 2013) on the ZnO growth reported that the ratio of HMT and zinc nitrate in the precursor solution and growth temperature have significant effect on the orientation, density and growth condition of the ZnO nanorods. In the experiment, the ratio of the precursor solution was altered by varying HMT concentrations for 0 mM, 2 mM, 5 mM, 10 mM, 12 mM and 15 mM with a fixed zinc nitrate molarity of 10 mM. It was reported that the HMT molarity amount of 10 mM which formed 1:1 molar ratio of the precursor solution demonstrated the highest photocatalytic efficiency compared to the others. Figure 2.15 shows the SEM micrograph of the hydrothermally grown ZnO nanorods with the variation of precursor molarity ratio between zinc nitrate and HMT. The individual nanorods grown on molar ratio of 10:1, 5:1, 2:1, 1:1, 1:1.2 and 2:3 are shown in respective Figure 2.15(a), Figure 2.15(b), Figure 2.15(c), Figure 2.15(d), Figure 2.15(e) and Figure 2.15(f). It was also reported that the ratio of 1:1 of zinc nitrate and HMT produces good quality and well-aligned ZnO nanorods (Mahmood *et al.*, 2013; Z. Zhou *et al.*, 2010) as shown in Figure 2.15 (d).

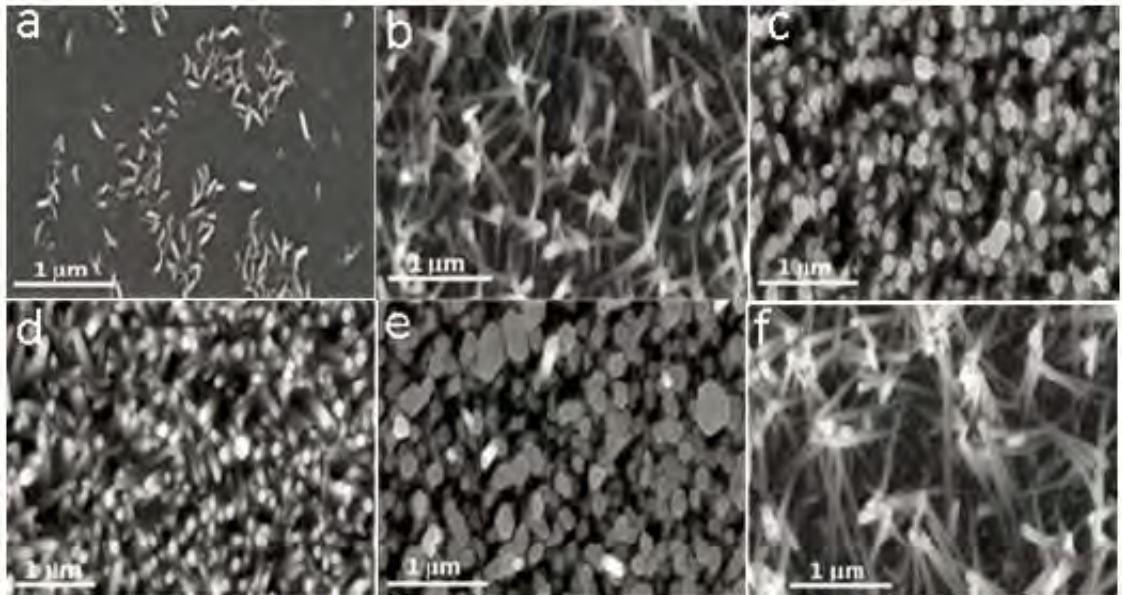


Figure 2.15 SEM images of ZnO nanorods fabricated hydrothermally using precursor solutions with molar ratio of (a) 10:0, (b) 5:1, (c) 2:1, (d) 1:1, (e) 1:1.2 and (f) 2:3. (Mahmood *et al.*, 2013)

It was also reported that the growth rate of ZnO nanorods are affected by the processing temperature due to faster thermal decomposition of hexamine and more OH⁻ are released at higher temperature. An experiment was carried out by varying the temperature of the growth process of 40 °C, 50 °C, 70 °C and 90 °C with 10 mM of precursor for 15 h of growth time. The result revealed that the fabricated ZnO nanorods under process temperature of 90 °C exhibited the highest photocatalytic efficiency. Figure 2.16 shows the cross-sectional SEM images of fabricated ZnO hydrothermally at different growth temperature settings. The growth of ZnO nanorods at temperature of 50 °C, 70 °C and 90 °C are shown in Figure 2.16(a), Figure 2.16(b) and Figure 2.16(c) correspondingly. It was observed that the ZnO grown at temperature of 90 °C have better array of ZnO nanorods as compared to other temperature levels.

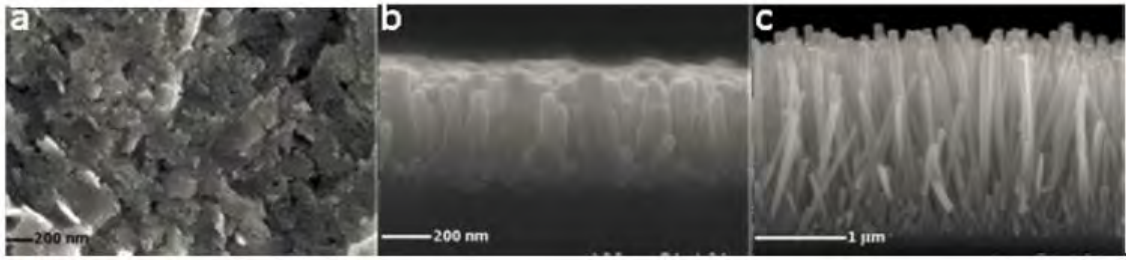


Figure 2.16 Cross-sectional SEM images of ZnO nanorods fabricated at temperature of (a) 50 °C, (b) 70 °C and (c) 90 °C. (Mahmood *et al.*, 2013)

2.8 Optimization of ZnO Growth

Although there were extensive reports on optimization process in synthesizing the ZnO nanostructures such as solvent variations (Tsay *et al.*, 2010), concentration alterations (Emphasis *et al.*, 2015; Mahmood *et al.*, 2013; Z. Zhou *et al.*, 2010), growth temperatures (Hambali *et al.*, 2014; Mahmood *et al.*, 2013) and growth time (Apiwattanadej *et al.*, 2015; Haque *et al.*, 2013), inconsistencies in terms of fabricated device performance still exist. This is because a very minor change in fabrication process could dramatically affect the properties of material (Uskokovic, 2013). For instance, there were several works regarding the fabrication of ZnO nanorods on curved surface of an optical fiber for the application of light coupling through the grown ZnO nanorods by Fallah *et al.* (Fallah *et al.*, 2013), Bora *et al.* (Bora *et al.*, 2014), and Rahim *et al.* (Rahim, Lokman, *et al.*, 2016). In the study, Fallah *et al.* presented the light side coupling where the source light was applied to the side of the optical fiber which ZnO nanorod were grown on its surface. The light excited into the optical fiber by ZnO nanorod and the guided light inside the fiber was measured at the end of the fiber as shown in Figure 2.17. The study presented light coupling measurements were done on several optical fibers grown with ZnO processing time from 2 h to 6 h. The result shows that the maximum coupling efficiency was observed on the sample with ZnO grown at 5 h growth duration.

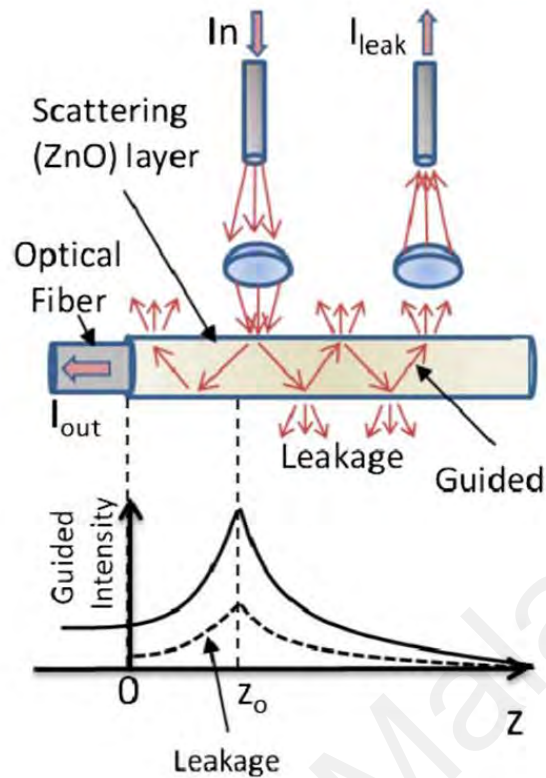


Figure 2.17 Schematic representation on light side coupling to cladding modes through ZnO nanorods (Fallah *et al.*, 2013).

In other work by Bora *et al.*, an identical light side coupling measurement setup was presented as shown in Figure 2.18. The optical fibers were coated with ZnO nanorods with growth times of 5 h, 8 h, 10 h, 15 h and 20 h. It was observed that the length and diameter of ZnO nanorods increased significantly as the growth time increases. Nevertheless, it is not necessarily means that the longer growth rate produces higher fabricated device performance. Among the samples grown with different processing times, it was reported that the sample with 8 h growth time exhibited the maximum average coupling efficiency among all.

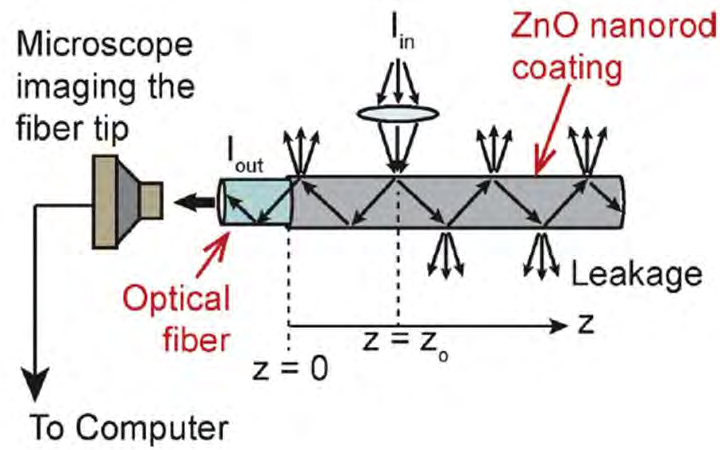


Figure 2.18 Schematic representation showing the side coupling of light to cladding mode in an optical fiber coated with ZnO nanorods (Bora *et al.*, 2014).

Rafis *et al.* (Rahim, Manjunath, *et al.*, 2016) presented another work on light side coupling which ZnO nanorods were grown on plastic optical fiber. The study presented the growth of ZnO nanorods were accomplished for 8 h, 10 h, 12 h, 15 h and 20 h in comparison with bare optical fiber (non-coated). Figure 2.19 presented the optical fiber grown with 12 h growth time yielded the maximum output voltage from the demonstrated light side coupling. It was reported that the growth time of 12 h was the optimum processing rate which limiting backscattering by ZnO nanorods and resulted maximum coupling efficiency on the sample compared to others processing time.

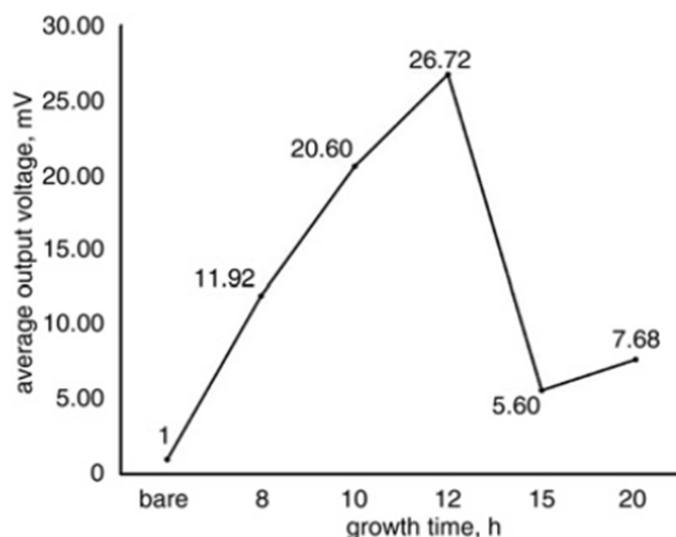


Figure 2.19 Average output voltage observed by light side coupling demonstration on samples with different growth times (Rahim, Lokman, *et al.*, 2016).

These presented works show that there were inconsistencies in terms of optimum growth times in order to achieve the highest light coupling efficiency. This indicates that a similar device performance may not necessarily be achievable with the same growth processing procedure. This is due to the sensitiveness of the process which affects the physical structure or dimension of the ZnO nanorods thus vary the characteristics of the fabricated devices. This indirectly affects its performance when these fabricated devices were used for sensing application such as humidity or chemical vapor concentrations. Therefore, a new approach on the standard reference on operating condition of sensing device is needed and presented in this work.

2.9 Humidity and Formaldehyde Vapor Sensing

ZnO is one of widely used as sensing active material in detecting environmental physical parameters such as humidity (Aneesh *et al.*, 2011; Zuraidah Harith *et al.*, 2015; Salah *et al.*, 2014), chemical vapor (Bora *et al.*, 2014; Kannan *et al.*, 2017; M. Lokman

et al., 2016), gas (Bogue, 2015; Dikovska, Atanasov, Andreev, *et al.*, 2007; Patil *et al.*, 2016) as well as temperature (Rahim *et al.*, 2017). In this section, the employment of optical sensor for humidity and formaldehyde vapor sensing are discussed. The summary of the previous works related to humidity and formaldehyde vapor sensing is presented as shown in Table 2.3.

Table 2.3 Humidity and formaldehyde vapor sensing progress utilizing ZnO as sensing material.

	Sensing element	Synthesis method	Medium	Detection method	Tested range	Sensitivity	Reference
Relative humidity	Al-ZnO	Sol-gel	Tapered Plastic optical fiber	Intensity modulation	50% – 75% RH	0.0386 mV/%RH	Z Harith <i>et al.</i> , 2017
	ZnO	Hydro-thermal	Tapered single mode silica optical fiber	Intensity modulation	10% – 95% RH	0.014 /%RH	Liu <i>et al.</i> , 2012
	ZnO	Sol-gel	Multimode silica optical fiber	Evanescent wave absorption	5% - 95% RH	0.0012 /%RH	Aneesh <i>et al.</i> , 2011
Formaldehyde vapour	ZnO	Hydro-thermal	ITO/Glass	UV-light irradiation	0 – 1120 ppm	Not mentioned	Peng <i>et al.</i> , 2009
	ZnO	Chemical reduction	ZnO pellet	Impedance	100 – 800 ppm		Kannan <i>et al.</i> , 2017

2.9.1 Humidity Sensing

Humidity is the characteristics of water vapor present in gaseous form (Yeo *et al.*, 2008). The existence of humidity in environment significantly impacts in many areas of life including industrial production processes and health, amongst others (T. Jiang *et al.*, 2006). Measurement of humidity level is necessary for many applications such as food production industries, agriculture (Yang Liu *et al.*, 2007), chemical (Khijwania *et al.*, 2005b), medical (Zamarreño *et al.*, 2010), electronics, semiconductors (Zhang *et al.*, 2008), civil, weather forecasting and home environment (Muto *et al.*, 2003) [3-7]. Thus, monitoring humidity conditions are important for a better quality of life and to improve operational and manufacturing processes in various industries (Kiasari *et al.*, 2014). Humidity sensors are characterized into two types, namely,

relative humidity sensors and absolute humidity sensors. The major difference being in the sensing units is that relative humidity sensor uses the unit of relative humidity (RH) which refers to a function of temperature, while the absolute humidity is determined as a function of pressure with the measurement unit of dew/frost point (D/F PT) (AS Ismail *et al.*, 2015). Changes in capacitive, resistive or thermal conductivity properties are generally used for humidity sensing (Sin *et al.*, 2012). In conventional electronic humidity sensors, the RH level is determined on the basis of changes in electrical conductivity or capacitance but at high humidity levels it causes electric leakages (Akita *et al.*, 2010). Optical sensors based on nanomaterials provide an alternative to conventional electronic transducers. Utilizing optical fibers as waveguides, information can be carried over a long distance and the transmitted signal is resistant to electromagnetic interferences (A. Lokman *et al.*, 2016).

There were numerous research works utilizing optical sensor for detection of humidity concentrations. A relative humidity sensor presented by Harith *et al.* (Z Harith *et al.*, 2017) utilized a simple intensity modulation sensing principle. In this work, a tapered plastic optical fiber (POF) coated with Al-doped ZnO nanostructures was characterized by using He-Ne laser as light source and the output was connected to photo detector coupled with lock-in amplifier as illustrated in Figure 2.20. The performance of the sensor was observed to achieve the sensitivity of 0.0386 mV/% relative humidity from 50% to 75%.

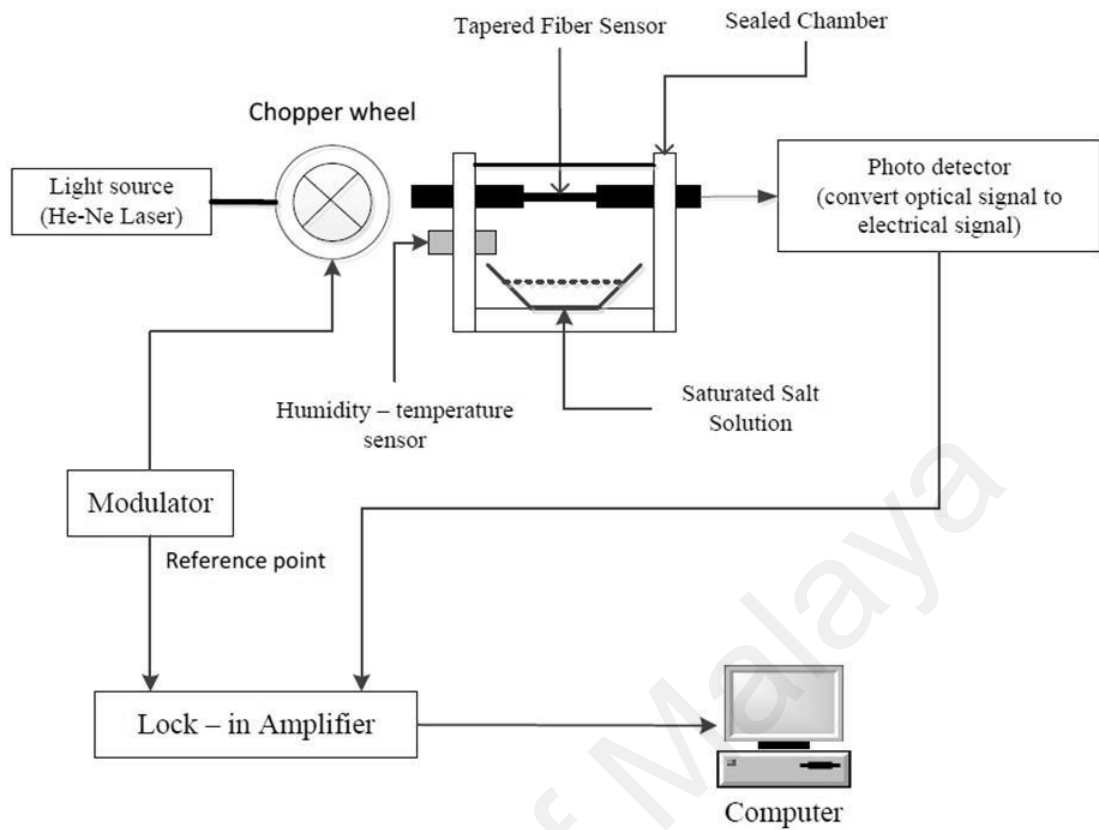


Figure 2.20 Experimental setup for humidity sensing using tapered POF coated with Al-doped ZnO nanostructures (Z Harith *et al.*, 2017).

Aneesh *et al.* (Aneesh *et al.*, 2011) demonstrated another work on humidity sensing which utilizing ZnO nanoparticles as sensing material coated on multimode optical fiber via sol-gel method. In this measurement, He-Ne laser operating at 632.8 nm was attached at one end of the fiber while a photo detector was connected at the other end coupled with data acquisition (DAQ) card as depicted in Figure 2.21. The sensing region was exposed to relative humidity concentrations inside humidity chamber while the output was measured by the photo detector. A linear sensitivity was observed at the rate of 0.0012 %RH for the measurement of humidity levels from 5% to 95%.

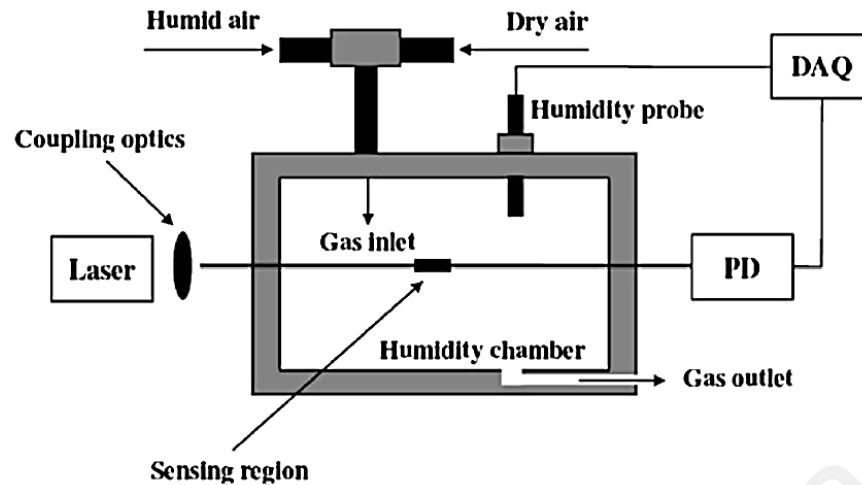


Figure 2.21 Experimental setup for humidity sensing with optical fiber coated with ZnO nanoparticles (Aneesh *et al.*, 2011).

Humidity sensing presented by Liu *et al.* (Yanjuan Liu *et al.*, 2012) utilizing thinned silica fiber coated with ZnO nanorods. The ZnO nanorods were well-arrayed grown on surface of the fibers with different diameters of 5 μm , 10 μm and 20 μm . Figure 2.22 shows the humidity experimental setup performed on the fabricated silica fiber coated with ZnO nanorods arrays. A laser source (wavelength: 644 nm) was used as a light source to the sensing system while an optical power meter was used to measure the output power of the system. The measurement was done at relative humidity levels from 10% to 95% at a constant temperature of 25 $^{\circ}\text{C}$. It was found that the 5 μm diameter silica fiber performed the best sensing towards humidity levels with the sensitivity of 0.014 %RH compared to the 10 μm and 20 μm of fiber diameters.

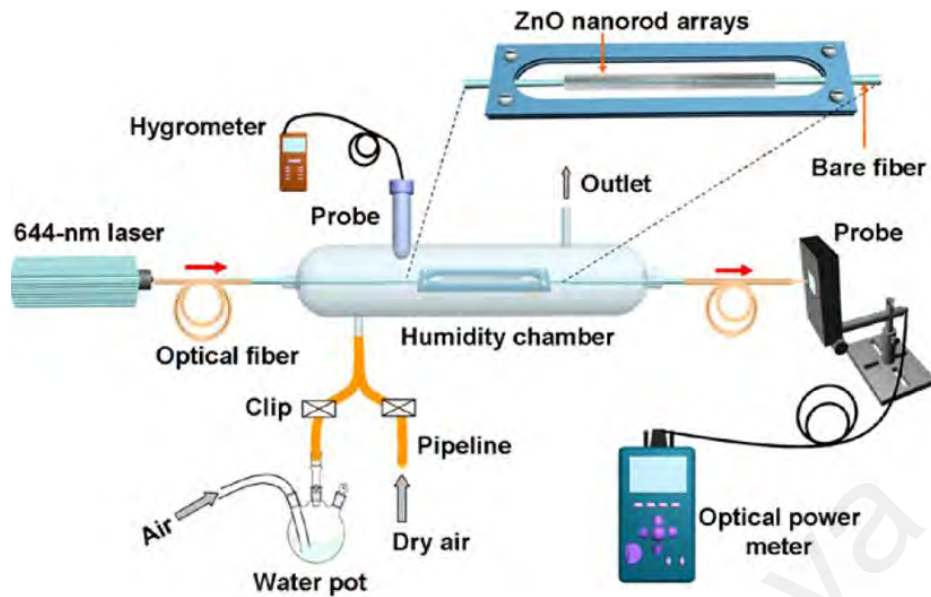


Figure 2.22 Experimental setup utilizing silica fiber coated with ZnO nanorods arrays for humidity sensing (Yanjuan Liu *et al.*, 2012).

The presented works show that the humidity sensing setup utilized high grade and costly optical equipment such as laser sources, high quality optical power meter, photo detector, special probe for the optical meter, data acquisition card for interfacing with computer and lock-in amplifier. This equipment limits its wide spread application and reduce its potential commercial value. The ease of operation and fabrication cost for a sensor device are important factors in order to increase the marketability of the device. Therefore, the utilization of cost-effective components is one of the alternatives in order to reduce the development cost of sensor device which will be presented towards the end of this research work.

2.9.2 Formaldehyde Vapor Sensing

Formaldehyde (HCHO) is a colorless and pungent-smelling gas which considered being a toxic air pollutant in both indoor and outdoor environment (Kannan *et al.*, 2017; Peng *et al.*, 2009). It can be found in adhesive such as urea-formaldehyde (UF) and phenol-formaldehyde (PF) resins used for productions of furniture, building materials and interior decorations (Feng *et al.*, 2013; Liteplo *et al.*, 2002; Peng *et al.*, 2009). The release of formaldehyde in indoor environment also can be found in various daily products such as cleaning agents, disinfectants, textiles, preservatives, photo-processing chemicals and cosmetics (Feng *et al.*, 2013; Kannan *et al.*, 2017; Liteplo *et al.*, 2002). At room temperature, formaldehyde is a gas and can be converted into other type of gaseous derivatives like trioxane. It can be dissolved easily in water (H₂O) which then converts into a diol (CH₂(OH)₂). An aqueous solution of formaldehyde is known as formalin. Pure formalin is a saturated solution of formaldehyde in water (approximately 37% by weight) (Dar *et al.*, 2016).

Formaldehyde is one of volatile organic compounds (VOCs) which is hazardous and become threat to human when the concentrations exceed a specific level (Leidinger *et al.*, 2014). According to World Health Organization (WHO), the safety threshold limit of exposure for outdoor should not exceed over 8 h for the concentration of 2 ppm while for indoor a maximum of 30 min on 0.08 ppm. (Choi *et al.*, 2013; Chung *et al.*, 2013; X. Jiang *et al.*, 2010; Jing Wang *et al.*, 2008). It has been confirmed by WHO that formaldehyde is teratogenic and it has been listed as human carcinogen by the International Agency for Research on Cancer (IARC) (Choi *et al.*, 2013; Salthammer, 2015; Jing Wang *et al.*, 2009; Xing *et al.*, 2016). It causes the “sick building syndrome” which results in acute health issues (Tran *et al.*, 2017). Several temporary symptoms have been recorded such as dizziness, headache, fatigue and irritation of eyes, nose, throat and skin (Burge, 2004; Liteplo *et al.*, 2002). The risk of asthma, nausea, allergy

and edema become greater when it is used together with protein (P. Zhou *et al.*, 2013). Prolonged exposure may cause damage to human body system such as respiratory system, central nervous system, blood and immune systems, pneumonia, bronchospasm and cancer (Hu *et al.*, 2011; Nuasaen *et al.*, 2014).

There are several detection methods of formaldehyde have been presented such as cataluminescence (K. Zhou *et al.*, 2006), spectroscopy (Werle *et al.*, 2002), chemiresistor (C.-Y. Lee *et al.*, 2006) and bio-sniffer (Mitsubayashi *et al.*, 2008). However, there is very limited study found on the formaldehyde vapor detection utilizing ZnO nanorods on optical fiber. Implementation of ZnO materials in detecting formaldehyde vapor has been presented by Peng *et al.* (Peng *et al.*, 2009) where ZnO nanorods were grown on ITO/glass substrate as shown in Figure 2.23. In this measurement, Xe-lamp was used as a light source. The detection was analyzed based on the change of photocurrent intensity when ZnO nanorods were exposed to formaldehyde on both with and without ultraviolet (UV) irradiation. It was observed that with UV light irradiation produced 120 times higher of response towards 1120 ppm of formaldehyde gas concentrations compared to without UV light irradiation.

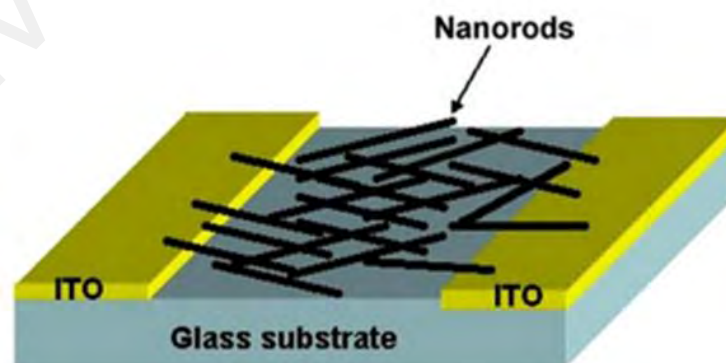


Figure 2.23 Schematic representation of the fabricated device structure for formaldehyde detection (Peng *et al.*, 2009).

In other work presented by Kannan *et al.* (Kannan *et al.*, 2017), the detection of formaldehyde vapor by ZnO nanoparticles was based on alteration of material impedance. The nanostructured ZnO was synthesized in a pellet form which used as sensing material. The fabricated samples were tested against formaldehyde vapor by exposing it to concentrations between 100 and 800 ppm at a constant room temperature. Complex impedance of the material was found responsive to the changes of formaldehyde vapor concentrations where charge transfer resistance was observed to decrease as the concentration increases. The pellet was also exposed to detect various gasses (ammonia, methanol, ethanol and propanol) and it was found that the fabricated ZnO pellet exhibits highest sensing response towards formaldehyde vapor compared to the others.

As reported in the literatures, the exposure of ZnO material to reducing gas such as formaldehyde change its material properties. In this case, the material impedance changed towards different concentrations of the vapor. This leads to the alteration of material complex conductivity in which indirectly affects its complex refractive index. Given the fact that ZnO has very good transparent properties (C.-F. Tang *et al.*, 2008), ZnO is proposed for the application of formaldehyde vapor sensing in addition to humidity sensing as discussed earlier.

2.10 Arduino as Data Acquisition Platform for Sensing Device

Today, Arduino has become an important element in numerous electronic design projects due to its practical capabilities and versatility (Rahman *et al.*, 2018). Arduino is an open source platform consists of hardware (microcontroller board) and software (processing language) (Galadima, 2014). It was originally used by designers to create electronic prototypes towards final small scale production due to low cost and ease of

use (Torroja *et al.*, 2015). There are several programmable platforms in the market apart of Arduino for example Raspberry Pi. Raspberry Pi is a small sized minicomputer which has inbuilt graphical processing unit (GPU) for display monitor (Patnaik Patnaikuni, 2017). Although it has sophisticated features, it is considered oversized for the usage of sensing application (León *et al.*, 2017). Arduino offers a suitable choice to serve as data processing platform for development of small scale sensing device. There are many Arduino boards available in the market such as Arduino UNO, Arduino PRO or Arduino MEGA. Arduino UNO possesses the basic hardware requirements to cope up with variety of communication protocols (Patnaik Patnaikuni, 2017). Figure 2.24 illustrates the layout of Arduino UNO platform. It is a microcontroller board which based on the ATmega328P (Oza *et al.*, 2018). It has 6 analog inputs and 14 digital input/output pins (6 of them can be used as PWM outputs). It has USB ports which can be connected to a computer to power up the platform. It also has an option to be powered up via power supply connector in the absence of USB connection. The specification detail of Arduino UNO systems is shown in Figure 2.25.

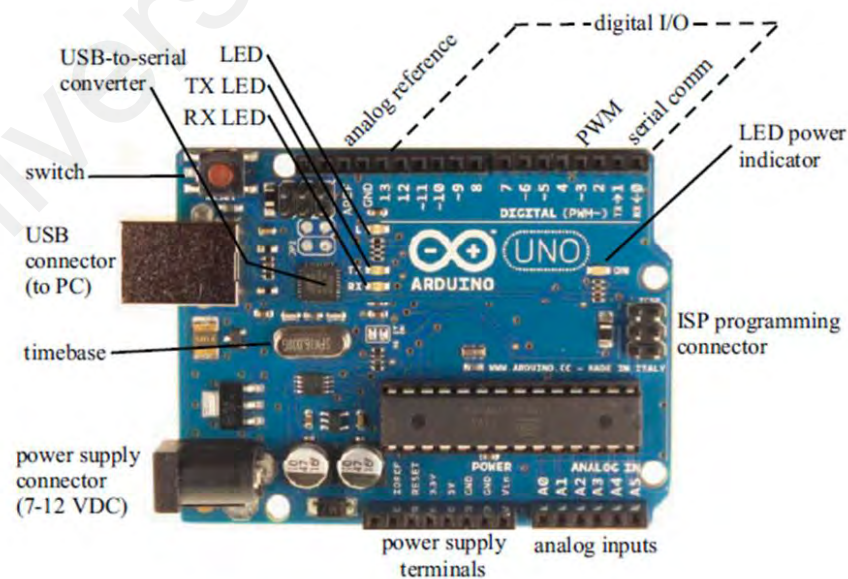


Figure 2.24 Arduino UNO R3 layout (Barrett, 2013).

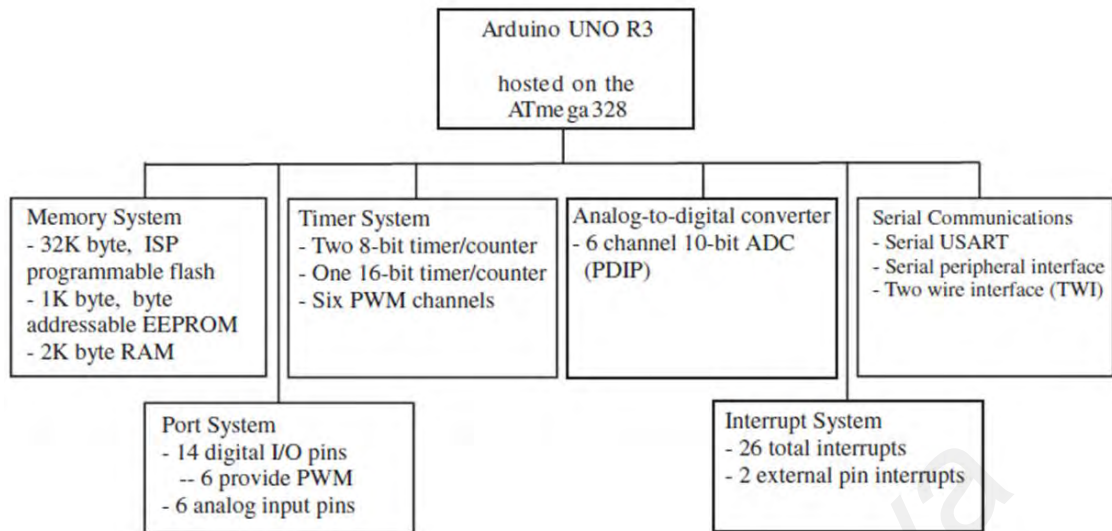


Figure 2.25 Arduino UNO R3 systems (Barrett, 2013).

Arduino UNO has capability to convert an analog input signal into a digital form via its built-in analog-to-digital converter (ADC) which operates with 10-bits of binary system (Arasu, 2017). In a sensor system, signal reading or acquisition from sensor output, data processing and analysis are the vital aspect (Arasu, 2017) so that the measurement reading can be accurately displayed and collected especially when used in critical monitoring system. In an optical sensing system, it is often associated with the usage of light as a sensing signal. The modulation of light intensity in response to change of physical parameters is determined and this usually measured by photo sensitive components such as photodiode. Generally, photodiode works as a current source that produces photocurrent (Sterckx, 2015). The amount of the photocurrent is depending on the amount of light intensity exposed to a photodiode in the event of sensing measurement. This photocurrent is then amplified and converted into a voltage form by an operational amplifier (op-amp) into suitable voltage level that can be read by Arduino platform. The voltage signal produced by an op-amp is usually in the format of

analog. Arduino uses its built-in ADC to convert the analog voltage signal into a digital format so it can be read by a computer for recording and displaying purposes.

2.11 Op-Amp for Signal Conditioning

Op-amp is an amplifier with a multi-stage high gain which normally has a differential input and a single-ended output (Fiore, 1992). Differential input means that one of the inputs produces a non-inverted output signal while the other one produces an inverted output. General symbol of an op-amp is shown in Figure 2.26 with V_{in+} and V_{in-} are the differential input. A single-ended output is labeled with V_{out} and op-amp is powered by supply rails labeled with $+V$ and $-V$.

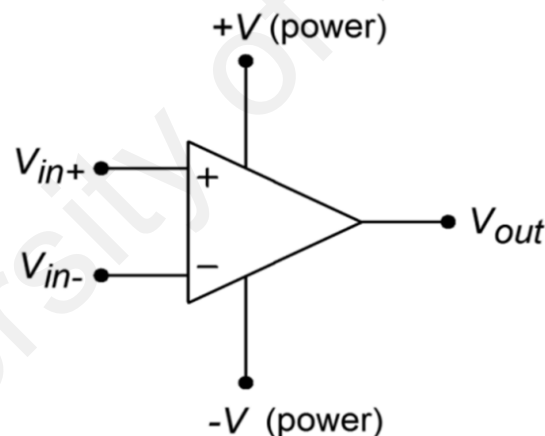


Figure 2.26 General symbol of an op-amp (Fiore, 1992).

Generally, op-amp has wide range of applications and it relies on the connection of its pinout. For example, op-amp can be used as an inverting amplifier, non-inverting amplifier, differential input amplifier, comparator, differentiator and integrator, voltage adder and many more (Carter *et al.*, 2001). The implementation of op-amp is depending on the purpose of signal conditioning of a system. In the application of sensing system,

the type of system output signal and the expected final output signal are essential to determine the type of op-amp to be used in the system. As explained earlier in Arduino part, an optical sensing system usually relies on light intensity measurement. Photodiode is commonly used in optical sensing system as photo detector to measure the intensity of the light at the output of the system. When measure the light, it produces photocurrent instead of voltage. The value of photocurrent can be as low as microampere level when the intensity of light is too low. Since a regular multimeter has no capability in measuring this small amount of current, an amplifier is needed to amplify the signal level that can be read by a sensing system.

When a photodiode used as a current source to an op-amp circuit, the photodiode must be connected to an inverting input (which has negative sign). This is due to photodiode produces negative photocurrent; therefore, the polarity has to be inverted to produce a positive voltage level. Figure 2.27 shows an equivalent circuit of the op-amp configuration where V_b , R_f , V_o , i_d and C_d is correspondingly referred to negative bias voltage, feedback resistor, output voltage, photocurrent and junction capacitance (Sterckx, 2015).

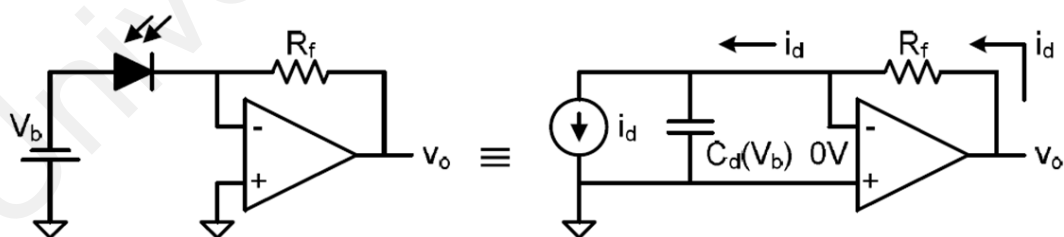


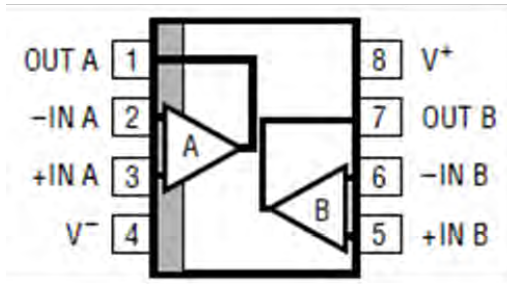
Figure 2.27 Equivalent circuit of the op-amp configuration with photodiode (Sterckx, 2015).

The output voltage (V_o) of the op-amp configuration can be expressed as (Sterckx, 2015)

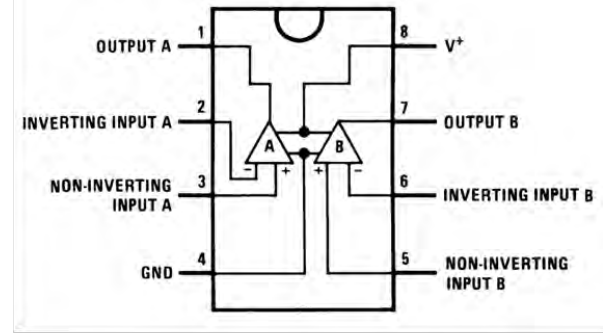
$$V_{out} = i_d \times R_f \quad (2.7)$$

Equation (2.7) explains that a suitable output voltage level for a sensing system can be obtained by varying the value of feedback resistor. The maximum amount of output voltage that op-amp circuit can yield is depending on model of op-amp available in the market. A consideration on power rails is important when selecting an op-amp. Most op-amp in the market needed both positive and negative power supplies. To simplify the sensing system configuration, positive voltage can be supplied by Arduino platform. However, the requirement of negative power supply makes a sensing system complicated where a separate negative voltage circuit is needed to power up an op-amp circuit. Therefore, the selection of suitable op-amp is important in order to realize a simple and compact sensing system.

Based on the research, there are two op-amp chip identified which can be operated with a single supply (positive and ground). They are LT1884 and LM358 which produced by Linear Technology Corporation (LinearTechnology, 2000) and Texas Instrument Incorporated (TexasInstrument, 2014) correspondingly. Their schematic diagram is shown in Figure 2.28 where the diagram of LT1884 and LM358 are depicted in Figure 2.28(a) and Figure 2.28(b) respectively. Both diagrams show they are having identical pinout configuration. In order to configure this op-amp to operate in a single supply mode for a sensing system, a photodiode is connected to the inverting input of the op-amp while ground terminal is connected to the non-inverting input. In this configuration, the op-amp chip can be powered up by a power supply terminal from Arduino platform without requiring any separate power supply thus simplify the configuration of sensing system.



(a)



(b)

Figure 2.28 Schematic diagram of (a) LT1884 (LinearTechnology, 2000) and (b) LM358 (TexasInstrument, 2014).

University of Malaysia

CHAPTER 3: GROWTH OF ZINC OXIDE NANOROD ONTO GLASS SUBSTRATE VIA HYDROTHERMAL SYNTHESIS METHOD

3.1 Introduction

The zinc oxide (ZnO) has excellent optical properties and thus it has attracted tremendous attention of researchers especially in sensing and optoelectronics applications (Gadallah *et al.*, 2013). ZnO material consists of zinc (Zn) and oxygen (O) which can be grown in numerous forms for various applications due to its low cost fabrication process, stability in thermal/chemical, radiation hardness as well as high transparency in visible range (Schmidt-Mende *et al.*, 2007). Due to these advantages, ZnO become one of the excellent choices to serve as sensitive element in optical sensor technology. There are various physical parameters can be sensed by ZnO layer especially in detecting vapors concentrations such as humidity, gases or chemicals. As explained in earlier chapter, intensity based sensor utilizes modulation of light intensity in measuring physical parameters. ZnO is well known of having refractive index of $\sim 1.9 - \sim 2.1$ (Bora *et al.*, 2014). When it is grown on a material that has lesser value of refractive index such as glass ($n_{glass} \sim 1.5$), it tends to induce leakage of light via the ZnO coating while the light propagating in the glass. The amount of light leakage by ZnO coating is depending on the physical structure and concentrations of the ZnO as well as the surrounding parameters that are being exposed to the ZnO layer as sensing element. In this chapter, the fabrication process of ZnO nanorods grown on glass substrate surface via hydrothermal synthesis method is presented. The optical characterization of the fabricated samples was subsequently investigated to analyze the effect of process growth time and coating length on light scattering by ZnO nanorods.

3.2 Growth of ZnO Nanorods via Hydrothermal Method on Glass Substrates

In this work, the growth of ZnO nanorods on glass substrates was done via hydrothermal synthesis method. This method requires two major steps which are seeding and growth processes as depicted in Figure 3.1. Prior to the synthesis procedure, the preparation of glass substrates first takes place.

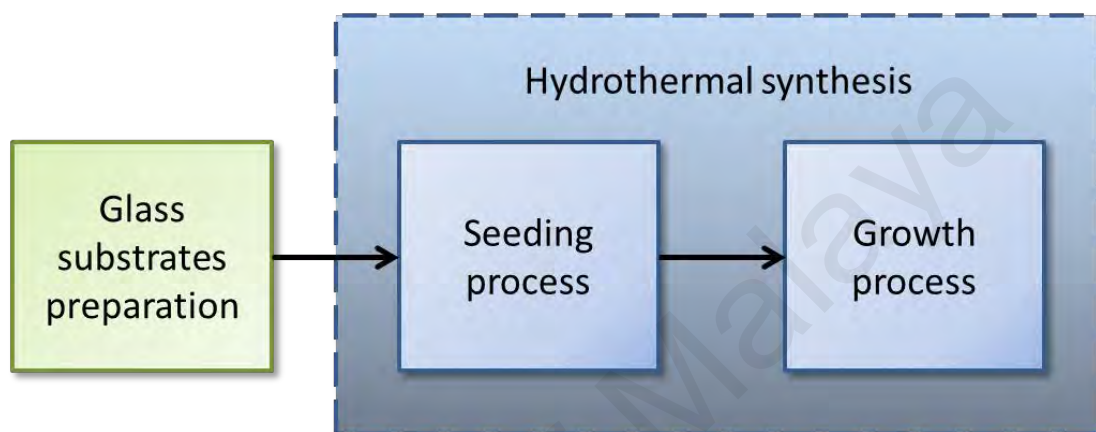


Figure 3.1 General procedures of ZnO nanorods synthesis via hydrothermal method.

3.2.1 Preparation of Glass Substrates

Figure 3.2 shows the steps involved in the preparation of the glass substrates before the synthesis process. The preparation procedures include the process of glass cutting, cleaning and masking. For this work, several glass substrates were prepared so that many combinations of ZnO nanorods growth conditions can be investigated.



Figure 3.2 Glass substrate preparation process.

Figure 3.3 shows the cutting procedure of the glass slides. Standard ground edges microscope glass slides with dimensions of 25.4 mm x 76.2 mm x 1 mm were used as substrates. Every glass slide was cut into several pieces of an approximate width of 15 mm each as depicted in Fig 3.3(a). Figure 3.3(b) shows how the glass was cut by using a glass cutter. The cutting process was done carefully to ensure each of glass substrate has identical dimension with smooth edge surface. Figure 3.3(c) shows the edge surfaces of the glass substrates after the cutting process. The edges of the glass substrates have to be as smooth as possible to ensure the consistency of the amount of light to be excited along the edges of the glass substrate. The final dimension of the glass substrate after the cutting process is shown in Figure 3.3(d). These glass substrates were used as platform where ZnO nanorods to be grown on its surfaces.

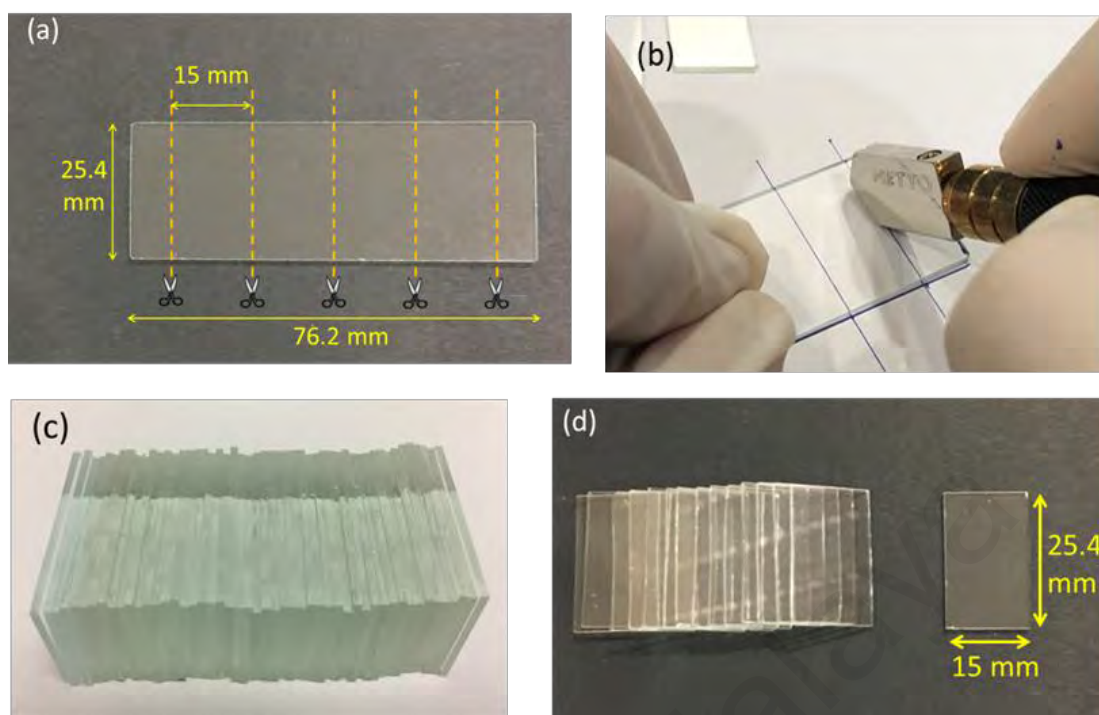


Figure 3.3 Glass slides cutting process. (a) Dimension of glass substrates to be cut from glass slide. (b) Glass slide cutting process with glass cutter. (c) The edges of the glass substrates. (d) Final dimension of glass substrate after cutting process.

The prepared glass substrates were then cleaned based on the procedure as described in Figure 3.4. The glass substrates were cleaned successively with a series of hydrochloric acid (HCl), sodium hydroxide (NaOH), soap water, acetone, ethanol and deionized (DI) water in ultrasonic bath respectively for 15 min each. This cleaning process is needed to ensure that the glass substrates are free from dirt, dust and stains on their surfaces. After the cleaning, the glass substrates were then dried in an atmospheric oven for 1 h at 120 °C.

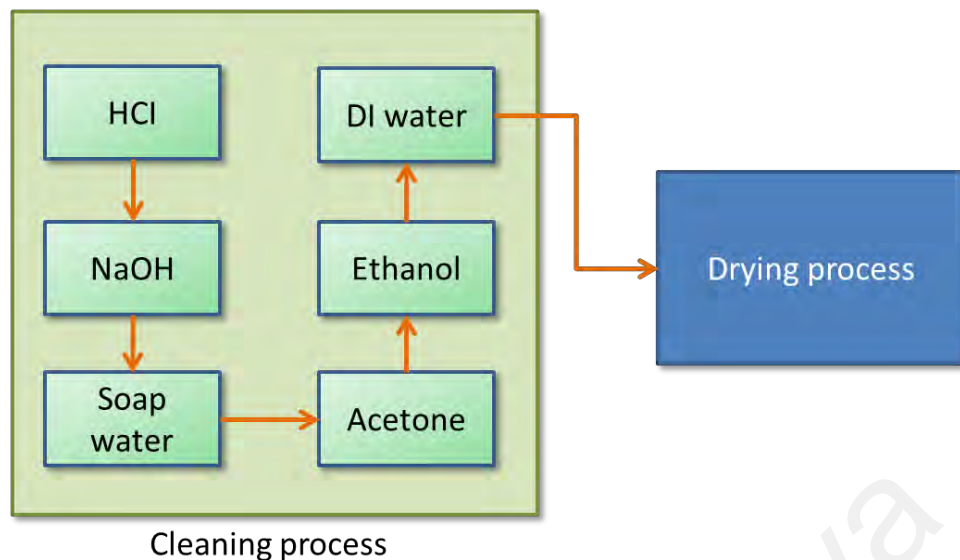


Figure 3.4 Glass substrate cleaning procedure.

After the drying process, the glass substrates were cooled down to room temperature and then masked with polytetrafluoroethylene (PTFE) tape with a triangular area on its surface exposed for depositing ZnO nanocrystallites as shown in Figure 3.5. In Figure 3.5(a), the PTFE tape was used in the masking process as it easily attached on the surface of the glass substrate without needing any adhesive. The existence of adhesive may affect the growth of ZnO nanorods due to chemical reaction during growth process. In this work, a triangular shape of ZnO nanorods coating on the glass substrate was proposed to analyze the effect of the coating length towards light scattering by ZnO nanorods. Therefore, a triangular area of 13 mm (L) x 13 mm (W) on the surface of every glass substrate was exposed as depicted in Figure 3.5(b). Figure 3.5(c) shows the final glass substrate masked with PTFE tape with triangular area exposed ready for the ZnO seeding process.

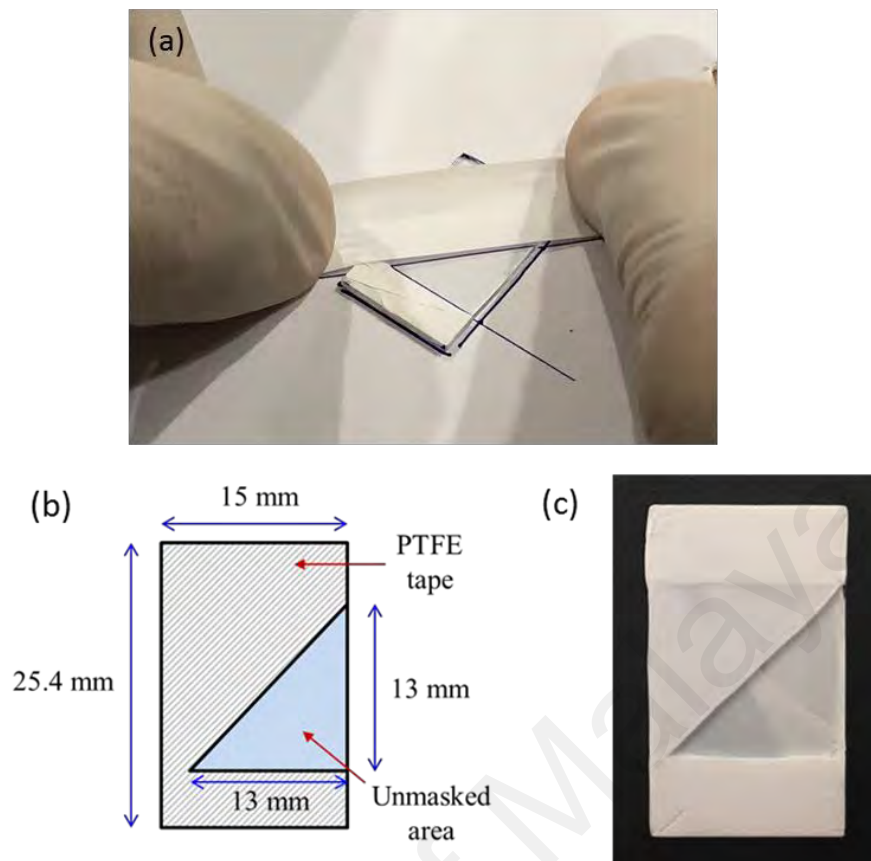


Figure 3.5 (a) Glass substrate masking process by using PTFE tape. (b) Dimension of the exposed triangular area. (c) Final masked glass substrate.

3.2.2 Seeding Process

Hydrothermal growth of ZnO nanorods are carried out first by seeding the glass substrates with ZnO nanocrystals followed by liquid phase epitaxy for the nanorods growth (Baruah *et al.*, 2009a; Kitsomboonloha *et al.*, 2009; Sugunan *et al.*, 2006). Seeding is the important steps in the synthesis process as it primarily affect the diameter, length and density of ZnO nanorods (Rafis *et al.*, 2017). There are three main steps involved in the seeding procedure which are the preparation of seeding solution, forming nucleation site on glass substrate and annealing process as shown in Figure 3.6.

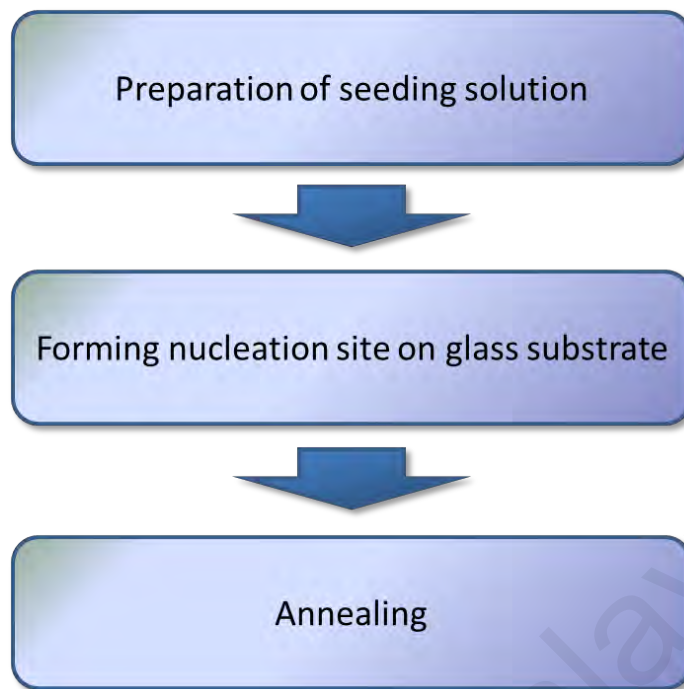


Figure 3.6 Procedures of seeding process on glass substrate.

In the first step of the process, 1mM concentration solution (Fallah *et al.*, 2013) was prepared by using 2.1949 mg of zinc acetate ($\text{Zn}(\text{CH}_3\text{COO})_2$) in 10 ml of ethanol as shown in Figure 3.7. The mixture was then sonicated for several minutes until the zinc acetate fully dissolved in the solution.

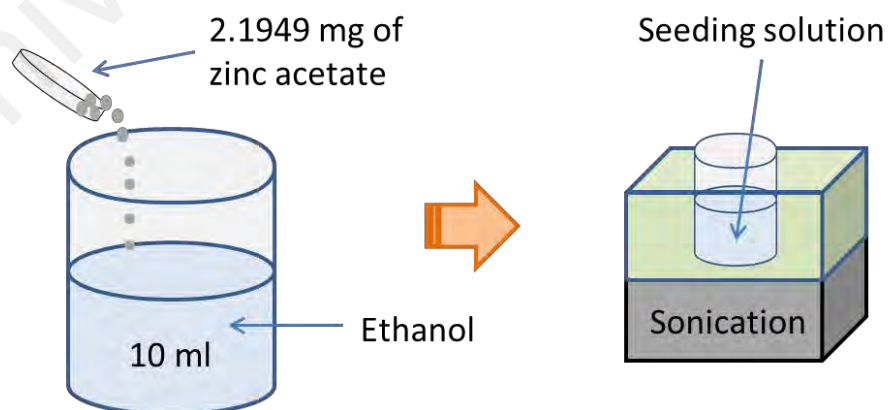


Figure 3.7 Preparation of seeding solution.

Figure 3.8 and Figure 3.9 illustrate the process of forming nucleation site on the surface of the glass substrate. In this work, the seeding process was carried by using drop and dry method which presented of having better uniformity (Rafis *et al.*, 2017). Briefly, the masked samples were placed on a hot plate at a fixed temperature of 70 °C as shown in Figure 3.9(a). By using a pipette, an amount of 50 μ l of zinc acetate solution was drop casted on the exposed surface of each glass substrates followed by air drying process. The entire process was repeated ten times. Figure 3.9(b) shows the procedure of dropping seeding solution onto the exposed surface of the glass substrates.

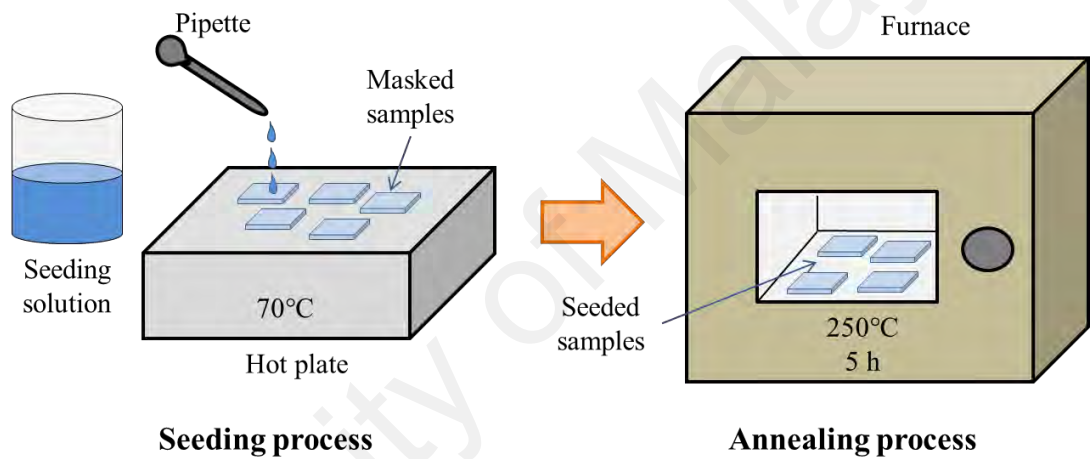


Figure 3.8 Masked samples seeding procedure.

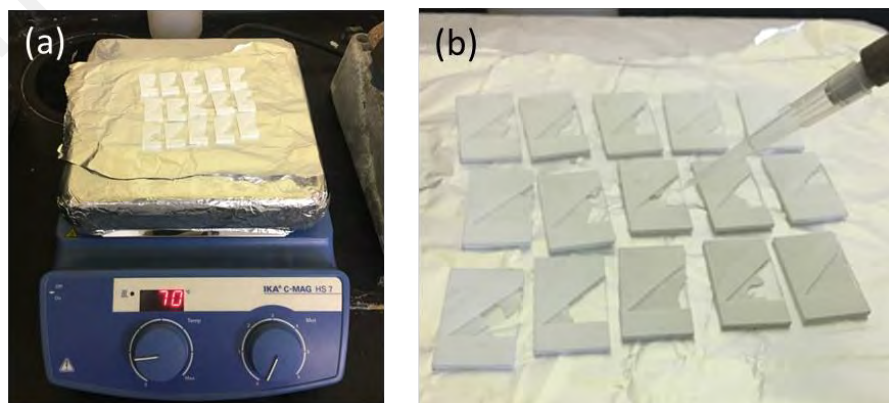


Figure 3.9 The process of seeding. (a) Masked glass substrates were heated on hot plate. (b) Drop and dry seeding process.

The seeded samples were then annealed in an atmospheric furnace as shown in Figure 3.10. During the annealing process, the temperature of the furnace was raised gradually before it reached the maximum annealing temperature of 250 °C. The glass substrates were then annealed for 5 h. At the end of the process, the temperature of the furnace was then gradually cooled down to room temperature before the glass substrates were taken out for subsequent hydrothermal growth of ZnO nanorods.



Figure 3.10 Annealing process in a furnace.

3.2.3 Growth Process

Figure 3.11 illustrates the procedure of growth process of ZnO nanorods. Briefly, a equimolar solution containing 10 mM of zinc nitrate hexahydrate ($\text{Zn}(\text{NO}_3)_2 \cdot 6\text{H}_2\text{O}$) and hexamethylenetetramine or HMT ($(\text{CH}_2)_6\text{N}_4$) with DI water was prepared (Baruah *et al.*, 2009b, 2009c; Kitsomboonloha *et al.*, 2009; Promnimit *et al.*, 2013). An amount of 1.18996 g of zinc nitrate and 0.56076 g of HMT were dissolved in 400 ml of DI water. This solution was used as a precursor for the ZnO nanorods growth.

Prior to the growth process, a stage setup for the samples was built in order to ensure a consistent and uniform distribution of the growth solution onto the surface of the glass substrates. As shown in Figure 3.11(a), several thin glass slides were used as stages to offset the seeded glass substrates in such a way that there will be some gap between the surface of petri dish and the seeded area of the glass substrates. The seeded glass substrates were then placed on the stages inside the petri dish where the seeded area of the glass substrates were facing downwards to the bottom of petri dish as shown in Figure 3.11(b). The samples were then dipped in the precursor solution and placed inside a growth chamber at 90 °C as shown in Figure 3.11(c).

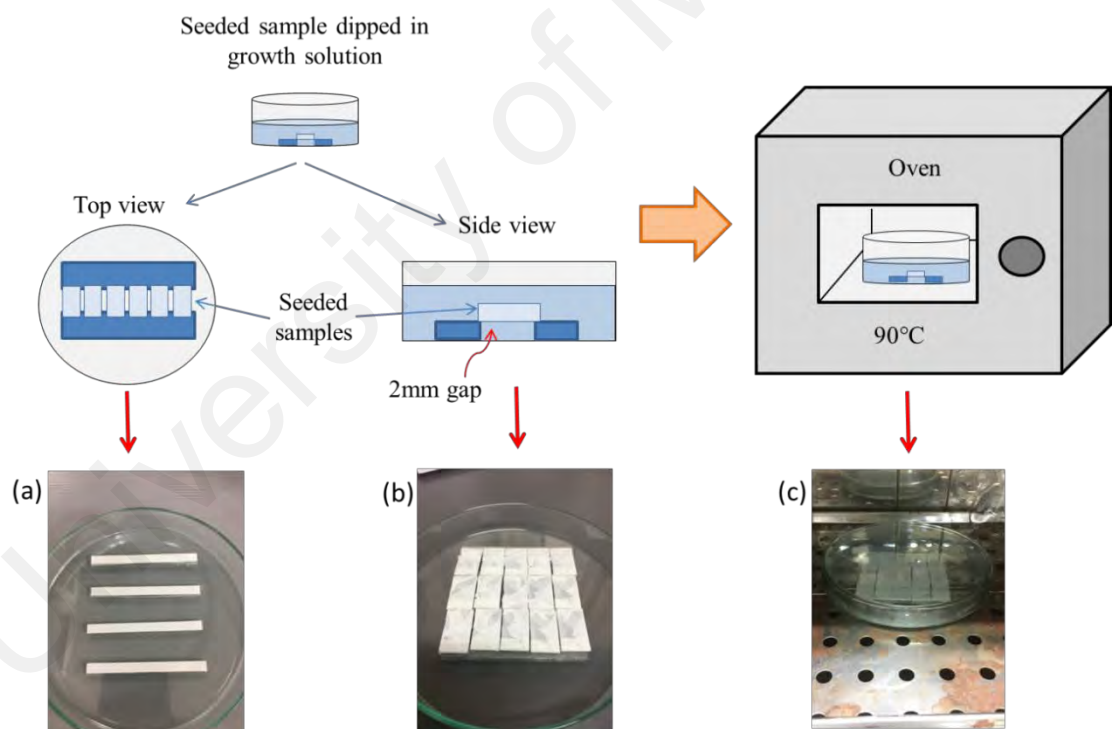


Figure 3.11 Procedure for growth process of ZnO nanorods. (a) Stages used for placing seeded glass substrates on petri dish. (b) Seeded glass substrates were placed facing downwards in petri dish. (c) Glass substrates dipped in precursor solutions and placed in an oven.

The duration for the growth time of the ZnO nanorods was varied for 5 h, 10 h and 15 h which were selected to cover all optimum growth conditions based on literatures (Bora *et al.*, 2014; Fallah *et al.*, 2013; Rahim, Lokman, *et al.*, 2016; Rahim, Manjunath, *et al.*, 2016). The solution was discarded and replaced with a new precursor solution every 5 h in order to maintain a constant growth rate of ZnO nanorods (Baruah *et al.*, 2009c). Figure 3.12 shows the final procedures in the fabrication process. At the end of the growth process, the glass substrates were retracted from the precursor solution and the masks were then carefully removed from the glass substrates. The glass substrates were then thoroughly rinsed with DI water to remove excessive mark at the non-coating area. The glass substrates were dried in an atmospheric furnace at 120 °C following by the post annealing process in the furnace at 350 °C for 1 h to remove any contaminations as well as electronic defect sites from the surface of ZnO nanorods (Bora *et al.*, 2017). The successful ZnO nanorods coated glass substrates at 5 h, 10 h and 15 h growth time are shown in Figure 3.13.

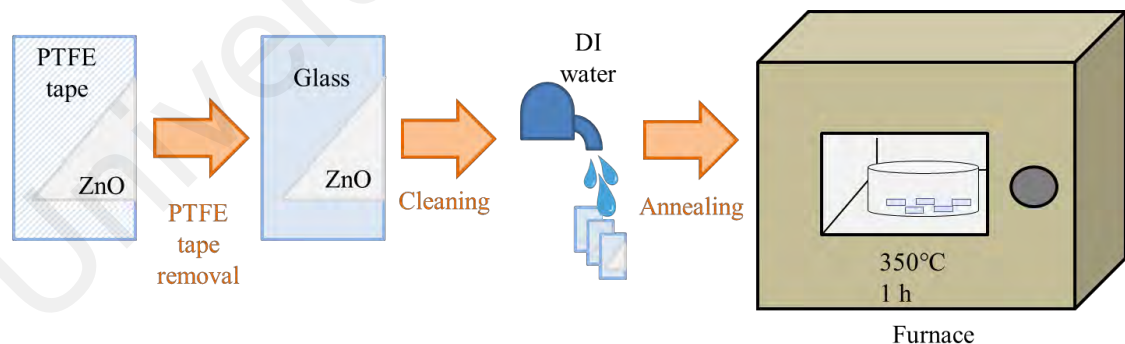


Figure 3.12 Final procedures after the growth process.



Figure 3.13 Successful ZnO nanorods coated glass substrates at growth time of 5 h, 10 h and 15 h.

3.3 Optical Image of ZnO Nanorods Layer on Glass Substrates

Figure 3.14 depicts the optical images of samples where the ZnO nanorods were successfully grown in triangular shape on glass substrates. The uniform coatings were observed throughout the glass substrates for the growth durations of 5 h, 10 h and 15 h as shown in Figures 3.14(a), 3.14(b) and 3.14(c), respectively. It was found that the density of the ZnO nanorods at the coating layer was the highest at growth duration of 15 h. The density was higher than that of 10 h and 5 h as observed from the optical images of Figure 3.14. It was observed that the growth duration of 15 h provides the brightest white coating layer on the glass substrates among all. For the sample with 5 h growth duration, it has slight transparent of coating layer than the other two. This indicates that the profiles of ZnO nanorods such as its diameter and length are changed as the growth duration increased from 5 h to 15 h which affect the density of the nanorods layer on the glass substrates.

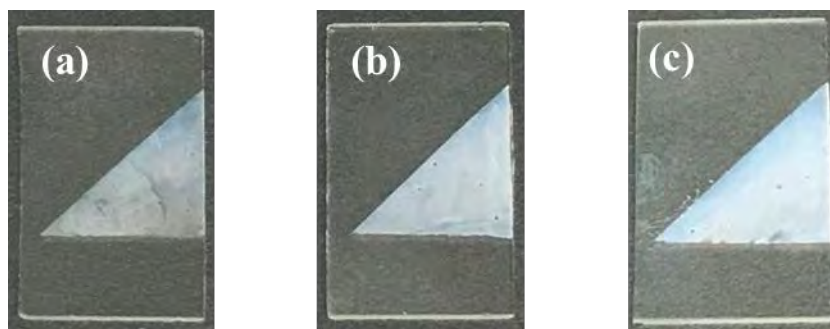


Figure 3.14 Uniform ZnO nanorods coating in triangular shapes on glass substrates for the growth durations of (a) 5 h, (b) 10 h and (c) 15 h.

3.4 ZnO Nanorods Characterization via FESEM

The microstructure of ZnO nanorods coating on glass substrates was characterized by scanning electron microscope (SEM, Hitachi SU5000 FE-SEM) operating at 20 kV. Figure 3.15 depicts the SEM images of the top view of typical ZnO coatings which were grown hydrothermally. It shows the hexagonal wurtzite ZnO nanorods structure. Figures 3.15 (a), (b) and (c) show the SEM images for growth durations of 5h, 10h and 15h, respectively. The width or diameter of the nanorods was observed to grow larger as the growth time increases from 5 h to 15 h. Figure 3.16 shows the cross-sectional SEM image of the ZnO nanorods. The nanorods grown on the glass substrates for growth durations of 5 h, 10 h and 15 h are shown in Figure 3.16(a), 3.16(b) and 3.16(c) respectively. It was observed that the nanorods have better orientation and longer in length size when its growth duration was increased from 5 h to 15 h.

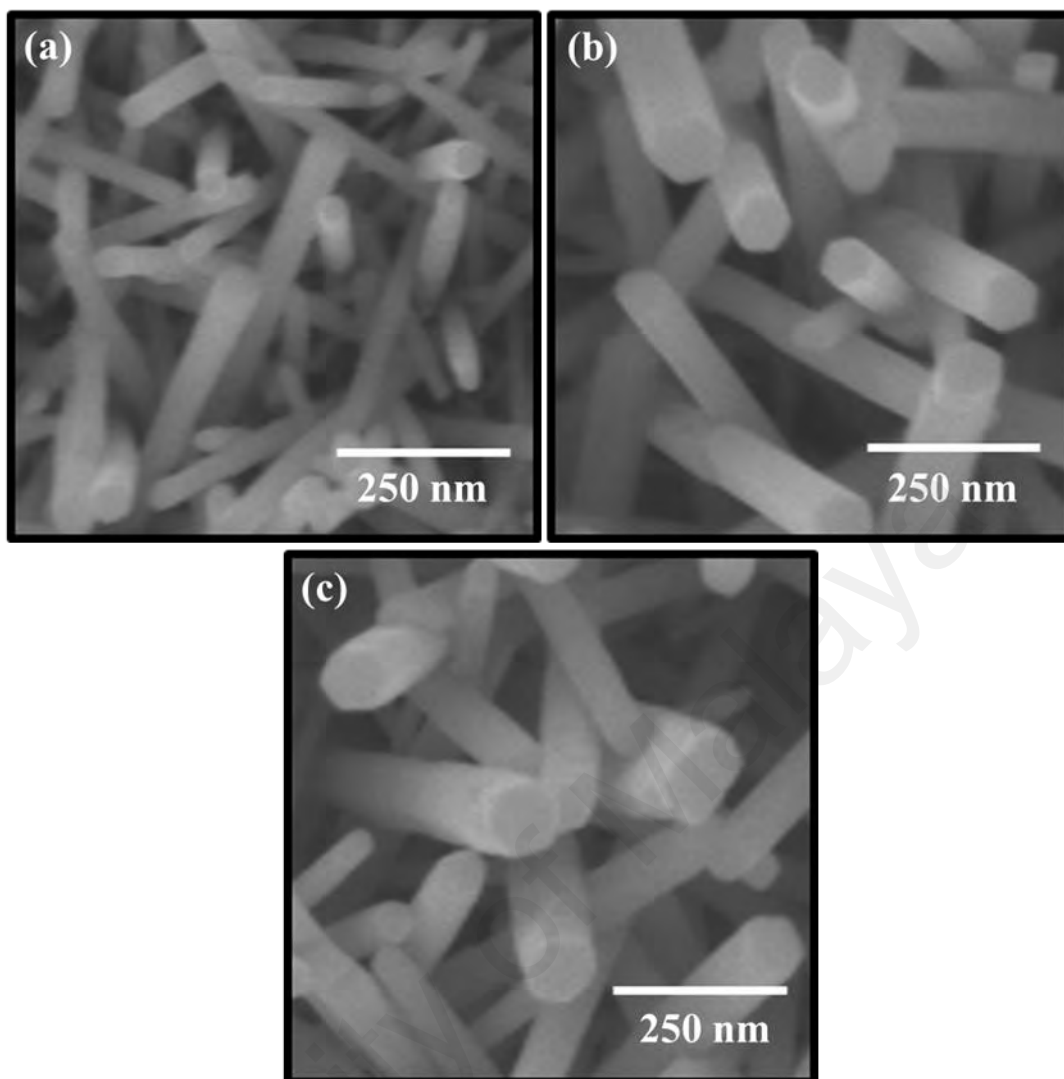


Figure 3.15 Top view of the ZnO nanorods grown on glass substrate for the growth durations of (a) 5 h, (b) 10 h and (c) 15 h.

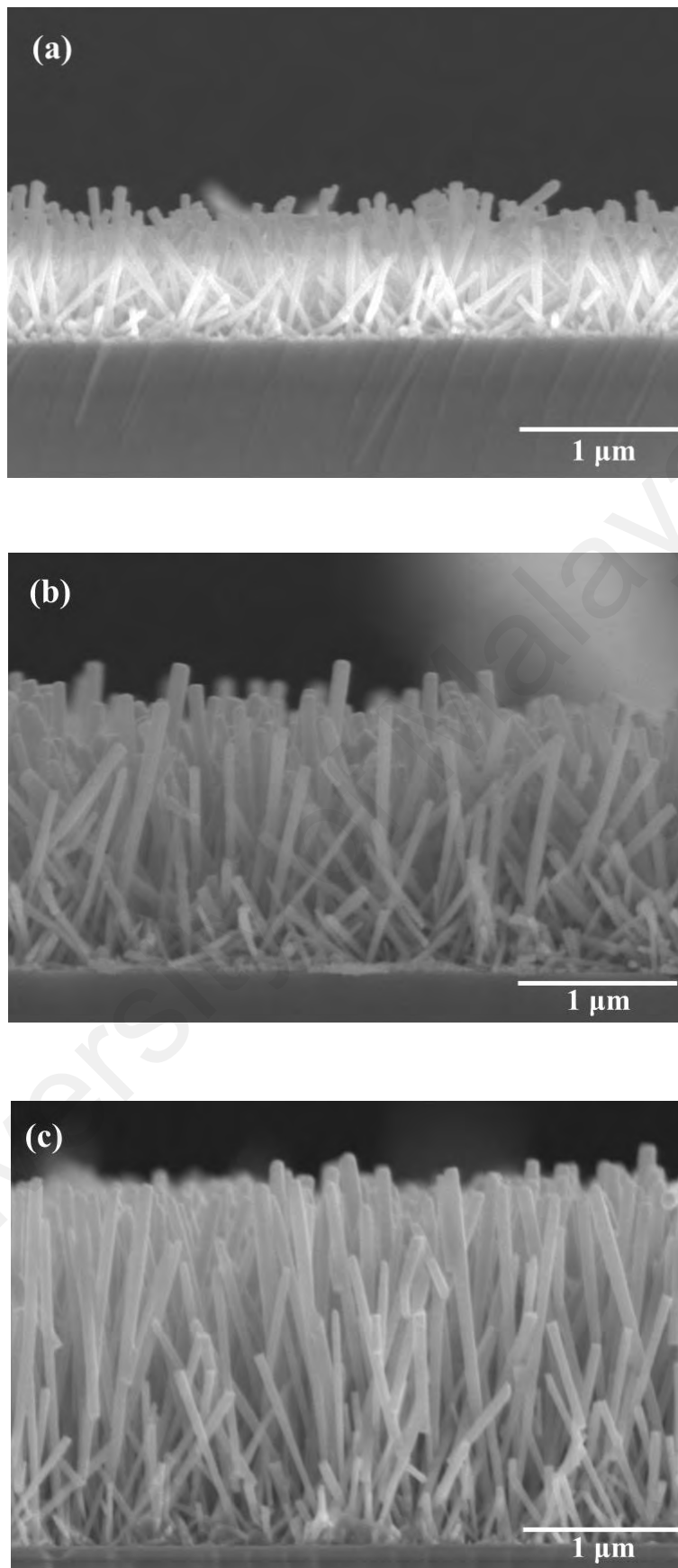
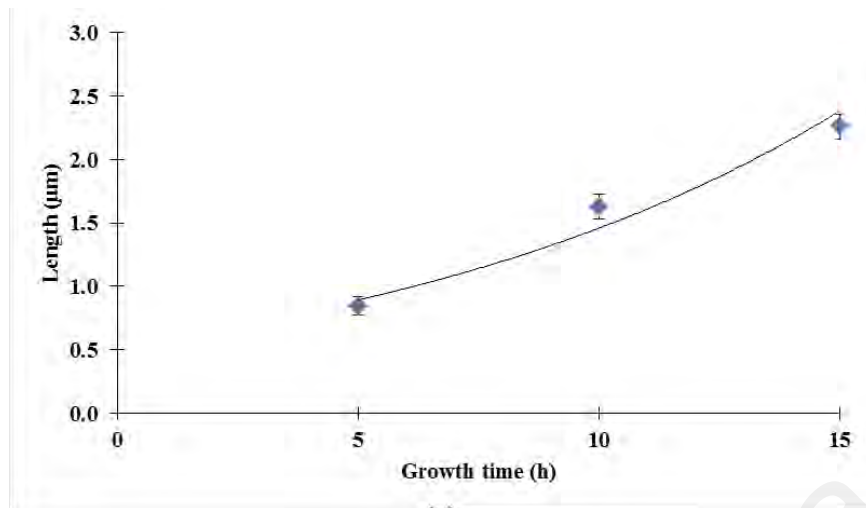
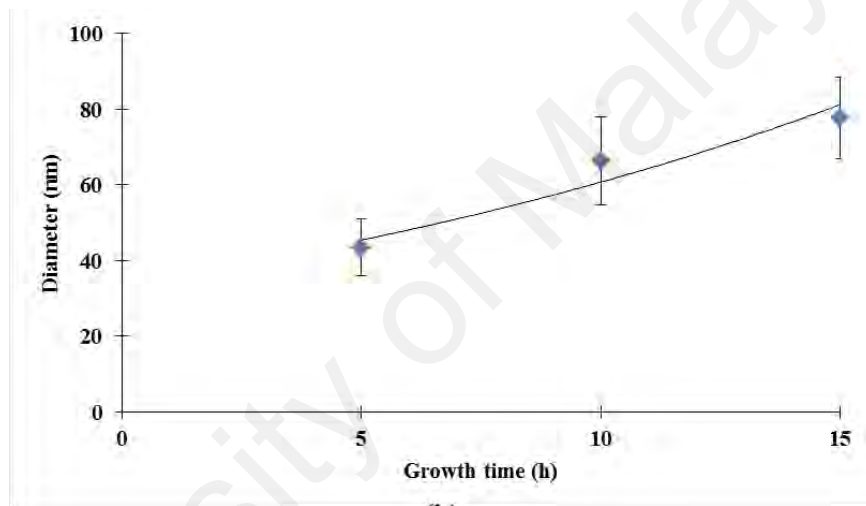


Figure 3.16 Cross sectional SEM image of ZnO nanorods on glass substrate for the growth durations of (a) 5 h, (b) 10 h and (c) 15 h.

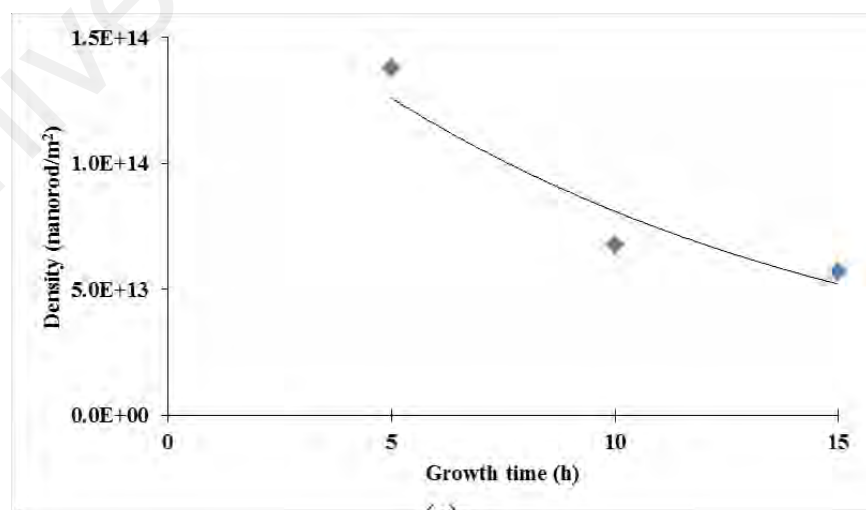
Figure 3.17 shows the comparison graph between growth time for the length, diameter and number of nanorod per unit area. The average length of nanorods were found to be 0.85 μm , 1.62 μm and 2.26 μm for the respective growth times of 5 h, 10 h and 15 h as shown in Figure 3.17(a). The average length of nanorods was obtained by measuring multiple nanorods on the same sample. It was observed that beside the length of the nanorods, the width also increases with the growth duration. In Figure 3.17(b) the trend of the nanorods width with growth time which increased from ~ 43 nm to ~ 78 nm for 5 h to 15 h growth times, is shown. It was also found that with increasing diameter of the nanorods, the density or number of nanorods per unit area decreases subsequently from 1.4×10^{14} nanorods/ m^2 to 5.7×10^{13} nanorods/ m^2 for respective growth times as shown in Figure 3.17(c). This behavior was due to coalescence process during nanorods growth process (Mohd Fudzi *et al.*, 2018). As nanorods growth longer and larger, some of the nanorods merged to form bigger nanorods.



(a)



(b)



(c)

Figure 3.17 The comparison graph between the growth time for the (a) length, (b) diameter and (c) number of nanorods per unit area.

Figure 3.18 shows the X-ray diffraction (XRD) pattern which confirms that the ZnO nanorods are highly crystalline and exhibit hexagonal wurtzite structure based on the powder diffraction standards (JCPDS) card no. 01-070-8070. The diffraction angle (2θ) of 34.4° was observed for the maximum XRD peak intensity which corresponds to the (002) plane of ZnO. This demonstrates that the grown ZnO nanorods are well aligned in c-axis and the preferential growth is along the [0002] direction.

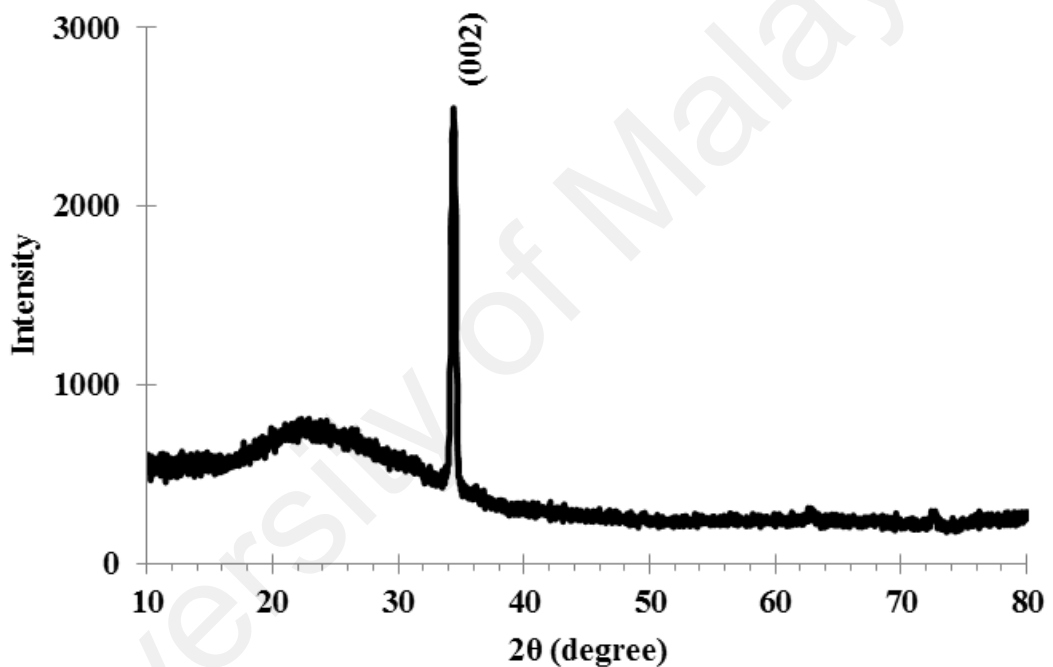


Figure 3.18 Typical XRD pattern of ZnO nanorods grown on glass substrate.

Figure 3.19 shows the energy dispersive spectroscopy (EDS) elemental analysis which disclosed that the top coating layer was consisted of Zinc and oxygen. The platinum (Pt) observed was due to the coating on the sample as procedure for SEM analysis. The carbon (C) was due to the usage of carbon tape to hold the sample in the procedure while Si and Ca existed in the EDS analysis were from microscopic glass slide (SiO_2 and CaO)

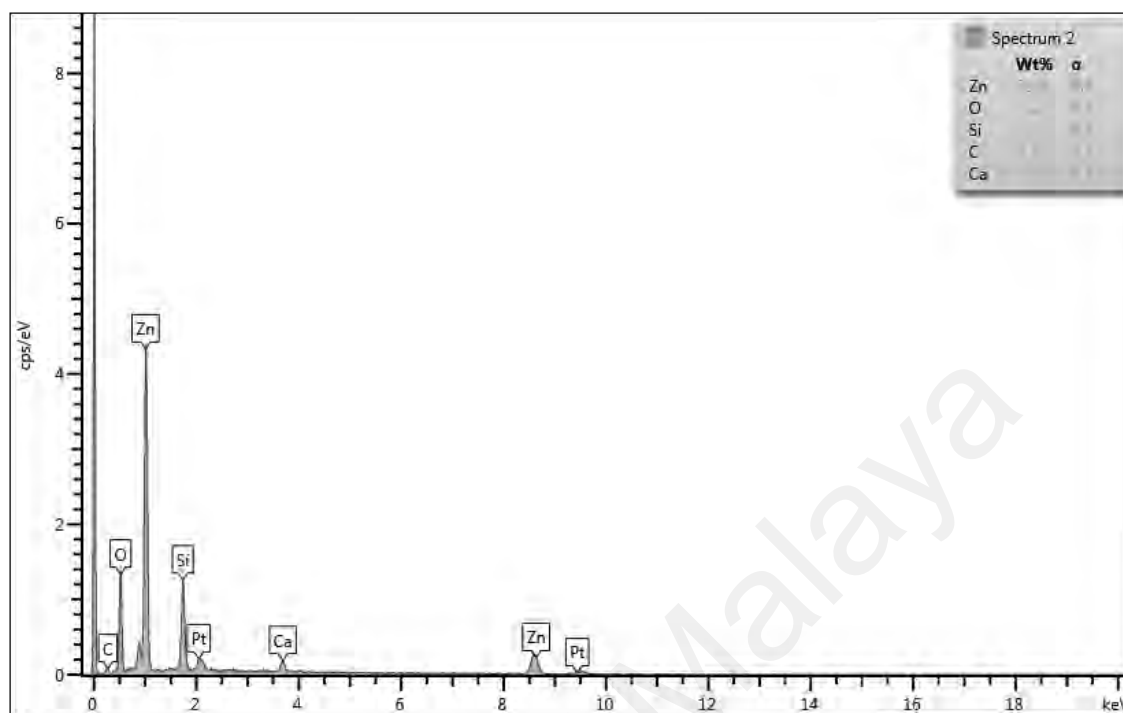


Figure 3.19 EDS spectrum of ZnO nanorods showing the peak of zinc and oxygen.

3.5 Optical Characterization of Glass Substrates Coated with ZnO Nanorods

Figure 3.20 shows an illustration of the setup for light scattering measurements on the fabricated samples. The ZnO nanorod coated glass substrates were placed on an automated translation stage controlled by Thorlabs APT-DC Servo Controller (Model no.: TDC001) and connected to a PC unit through graphical user interface (GUI). Thorlabs LED with 530 nm wavelength (Model no.: M530FI) was used as a light source which was controlled by Thorlabs LED driver (Model no.: LEDD1B). Green LED light source (530 nm) was chosen based on previous study by the group (Rahim, Lokman, *et al.*, 2016). In their study, three channels were tested (red, green and blue) and the effect of forward scattering for vapor sensing showed that green source produced the best sensing performance. The LED source was set as close as possible to the edge of the substrates that was aligned with a detector placed at the other end of the sample.

Thorlabs power meter (Model no.: PM100USB) with an input adapter (Model no.: S150C) ranging between 350 – 1100 nm with maximum power of 5 mW was connected through a polymer optical fiber (POF). The power meter was connected to a PC unit for data recording purposes. The power meter was connected to a PC unit for data recording purposes. The actual image of the optical characterization setup is shown in Figure 3.21.

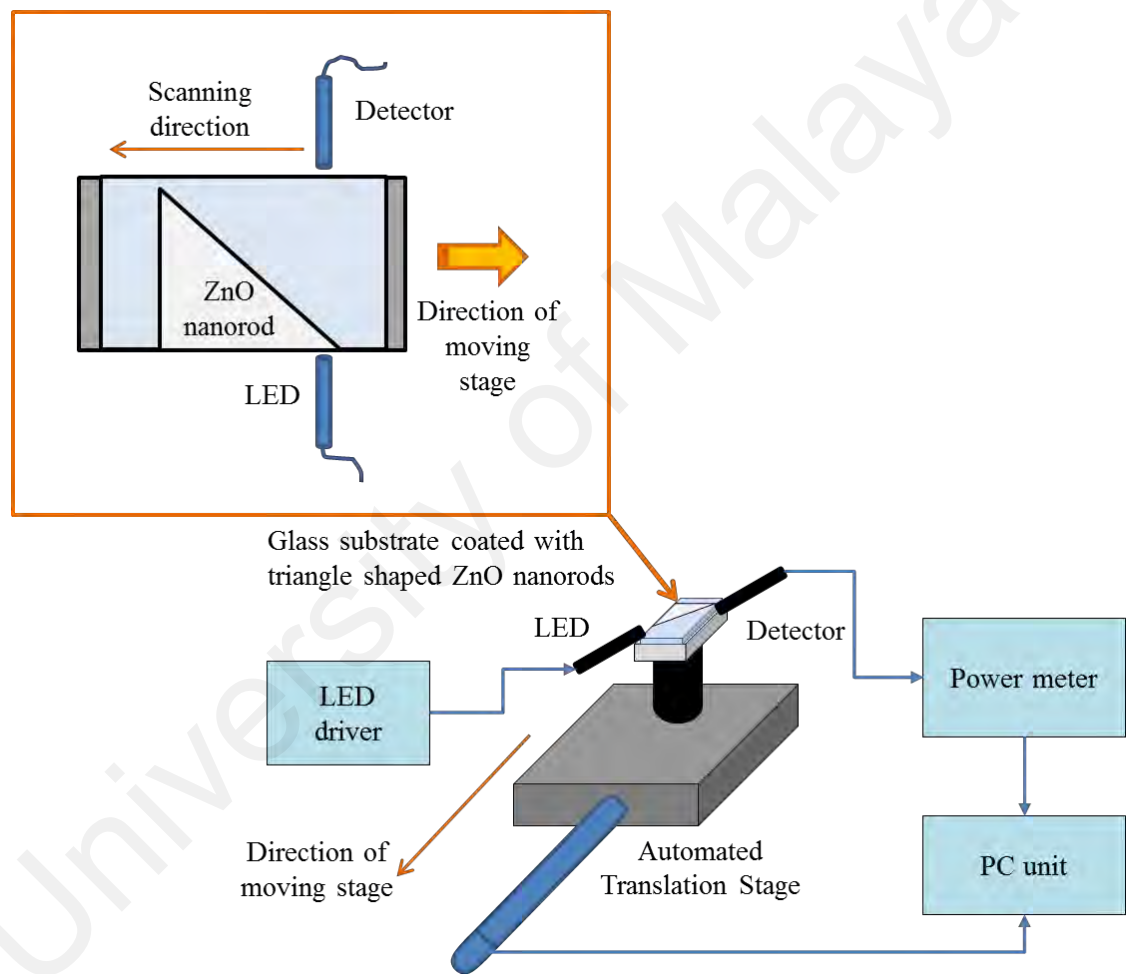


Figure 3.20 Schematic representation of the experimental setup for light scattering behavior of the glass substrate coated with ZnO nanorods. The inset shows the scanning direction of the light scattering measurement.

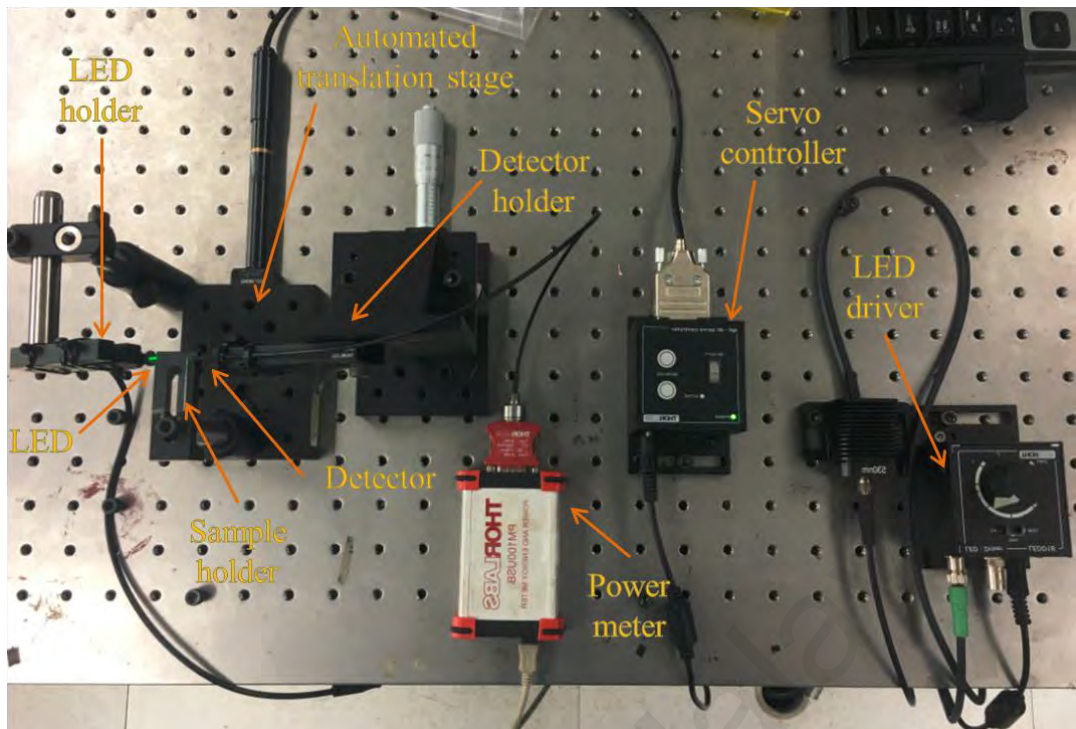


Figure 3.21 Actual setup for optical characterization.

In this experimental setup, the light source was placed at an incident angle of 50° close to the edge of the fabricated glass substrate. Therefore, the refraction angle for the light in the glass was about 30° . In this condition, the incident angle for the light at the interface between glass-air was 60° to achieve total internal reflection for both regions as shown in Figure 3.22. In this configuration, the loss mechanism can then be mainly attributed to scattering effects from the rods.

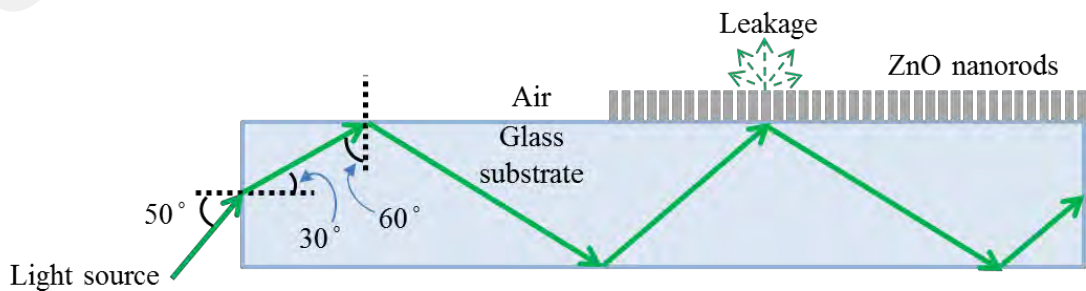


Figure 3.22 Incident angle of light source at the edge of glass substrate to achieve total internal reflection inside the glass substrate.

The measurement was done at standard level of humidity and temperature in the measurement room. As LED and detector were stationary and aligned at both sides of the sample, the output intensity power was measured and recorded by the power meter as the automated translation stage moved horizontally between the LED and the detector. As the automated translation stage moved, the sample was scanned throughout the edge of the glass substrate in such a way that the length of the ZnO coating on the light propagation between the LED and the detector varied from minimum to maximum as schematically represented in inset of Figure 3.20 and Figure 3.23. In this condition, the longer the ZnO coating length appear on the surface of the glass substrate along the light propagation path, the higher number of points of glass-ZnO interface interacted by the light while propagated in the glass substrate as depicted in Figure 3.24. As a result, the higher leakage of light scattered by ZnO nanorods observed thus reduced the output intensity level measured by the power meter.

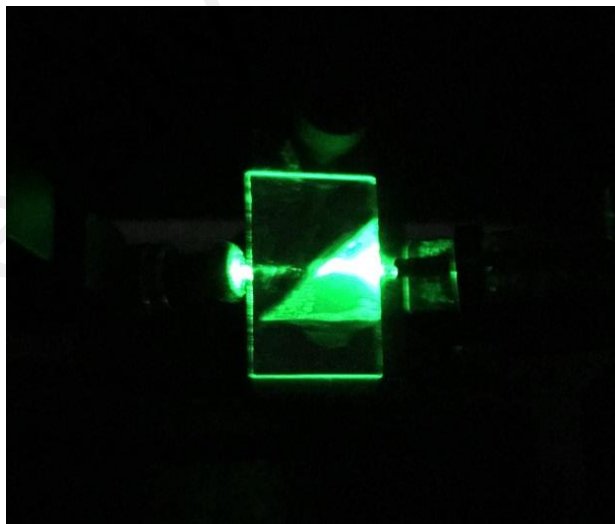


Figure 3.23 Light propagates inside the ZnO coated glass substrate via edge excitation.

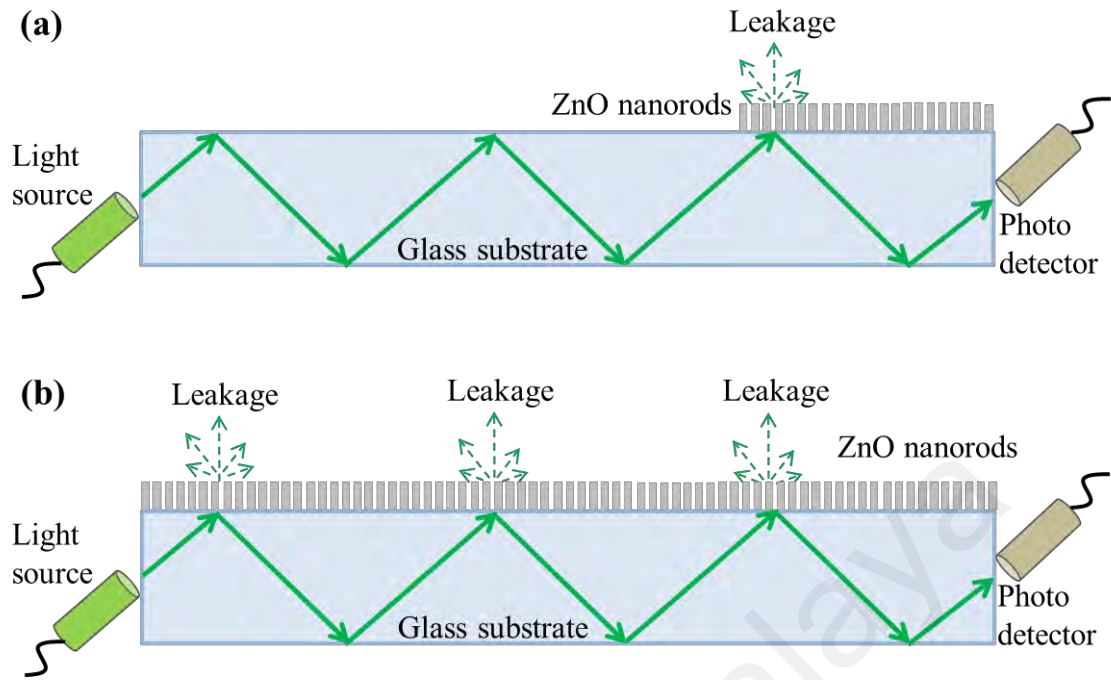


Figure 3.24 The leakage of light via ZnO coating at (a) shorter coating section and (b) longer coating section.

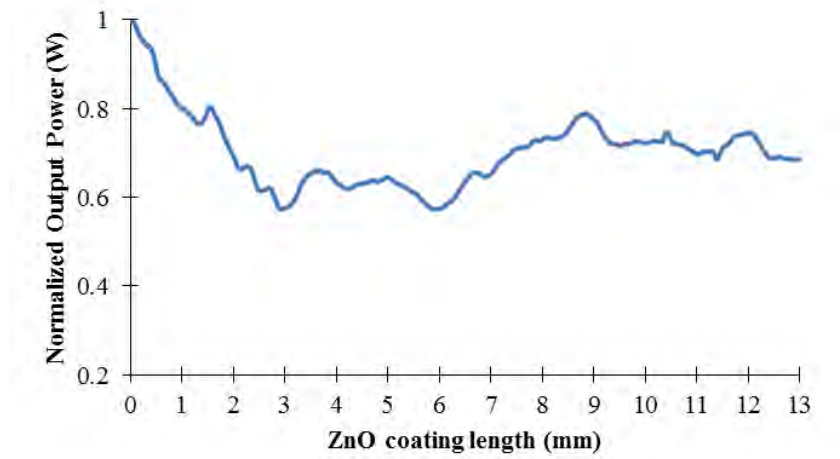
According to Beer-Lambert principle, the intensity of output light measured at the end of the propagation medium is expressed as (Hodgkinson *et al.*, 2012)

$$I = I_0 \exp(-\alpha x) \quad (3.1)$$

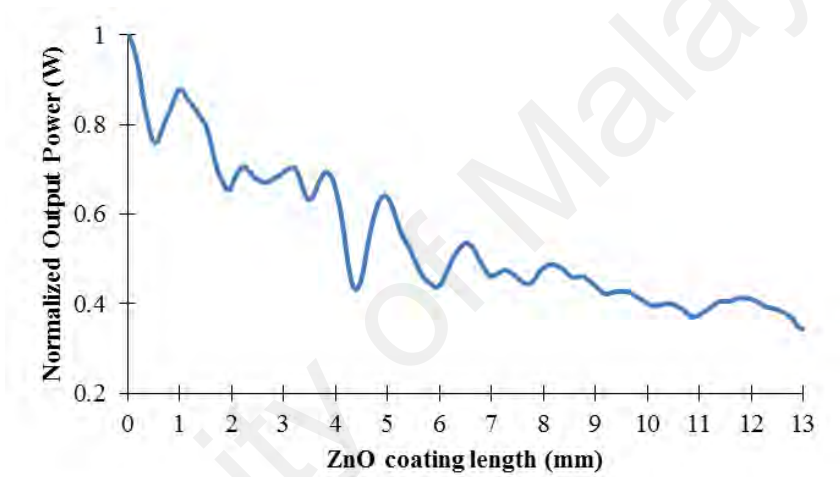
where the I_0 is the intensity of the input light signal, α is the absorption coefficient of the medium and x is the thickness of the medium which the light signal propagates from one end to another. In this work, α is represented by the scattering coefficient by the ZnO nanorods as it induces light leakage while the light propagating in the medium. The value of α would vary depending on the growth conditions of the ZnO nanorods. The value of x represented the length of the ZnO coating section along the width of

glass substrate which affects the rate of light leakage as the length changes. These two parameters contribute to the reduction of the light intensity captured at the output.

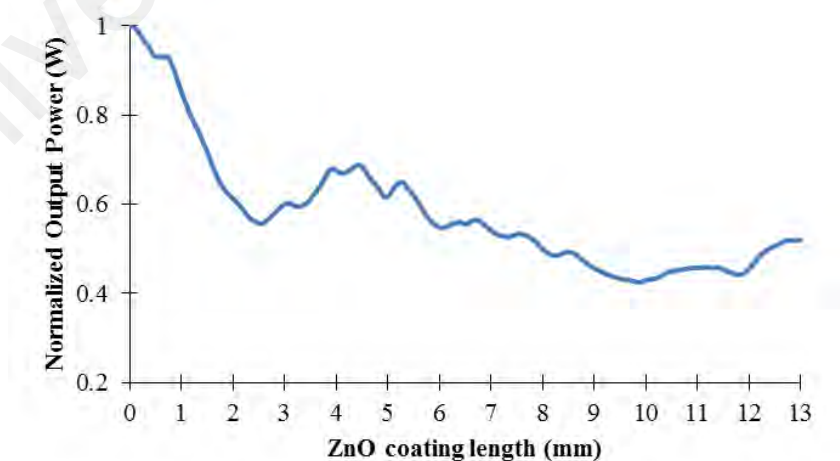
Figure 3.25 shows the output intensity power measured by the power meter scanning from 0 to 13 mm of the ZnO coating length on the glass substrates. The value for each sample was normalized with the optical power value measured at non-coated region. It was noted that in this condition the output power values were almost identical across all samples and can be set as reference. The normalization was done towards 1 W to keep the unit since it represented the output power. It was observed that the reduction of intensity was observed on all growth durations. Figure 3.25(a) shows the output intensity measured for the growth duration of 5 h and found that the intensity loss was the lowest among others. The intensity loss for sample with growth duration of 10 h was slightly higher than the one with 15 h as shown in Figure 3.25(b) and Figure 3.25(c) respectively. It was noted that the measurement of output power shows fluctuation as the coating length increased during the measurement. This condition was affected by two factors; the uniformity of the coating and the edge surface condition of the glass substrate where the light was excited. Although the uniformity of ZnO coating on all fabricated glass substrates was visually good with unaided eye, there were still non-uniformities at certain area on the coating thus affect the consistency of the light leakage by the ZnO nanorods. The inconsistencies of the scattering were also contributed by the condition of the surface of the glass edge during the cutting process. Since the glass cutting process was done manually, the smooth edge surface is not 100% achievable. Uneven glass edge surface still occurred and affected the amount of light which excited inside the glass substrate. However, the effect of the ZnO coating lengths still can be observed by the trend of the scanning results of the samples where the intensities of the output decay as the lengths increased. This trend was observed on all samples grown with different processing times.



(a)



(b)



(c)

Figure 3.25 Optical characterization of the ZnO coated glass substrate on coating length variation for the growth duration of (a) 5 h, (b) 10 h and (c) 15 h.

As observed from graph in Figure 3.25, it was noted that the amount of light leakage by the ZnO nanorods not only dependent on the length of the ZnO coating section but also affected by the growth time. This is because growth time changes the nanorods physical structures such as length, diameter and density. Here a first order scattering model is considered (Fallah *et al.*, 2013) where total scattering is considered as a superposition of scattering from each rod. Hence, over a distance dx of propagation the intensity (I) is reduced as (Fallah *et al.*, 2013)

$$\frac{dI}{dx} = -C_{sc}\rho_v I \quad (3.2)$$

where C_{sc} is the scattering cross section and ρ_v is the rods density per unit volume, $\rho_v = \rho_a/l$, and l is the average rods length. The scattering cross section of one rod depends strongly on the rods diameter, shape and length.

It is also worth mentioning that both forward scattering as well as backward scattering by nanorods influences the intensity losses. Forward scattering contributes to increasing light leakage while backward scattering lowers the leakage of light. With higher rod density and longer rods, backward scattering would dominate and thus improved trend can be observed compared to lower density of nanorods or lower nanorod lengths. Therefore, slightly higher output power was observed on the sample with 15 h growth maximum ZnO coating length as compared to 10 h.

Figure 3.26 shows the comparison of the output intensity of the glass substrates coated with ZnO nanorods for different growth durations measured at variation of coating lengths. The regression lines were generated by the software to examine the relationship between normalized output power and the ZnO coating length. It was found that the rate of output intensity reduction as the ZnO coating varied from 0 to 13 mm to be the highest on glass substrate coated with 10 h growth time which is at -0.0437

W/mm. The rate was lower for the other two samples with growth time of 5 h and 15 h which at -0.0057 W/mm and -0.0323 W/mm, correspondingly. This shows that the sample with 10 h growth time has higher scattering effect by the ZnO nanorods which induced higher leakage of light than the sample with 5 h and 15 h.

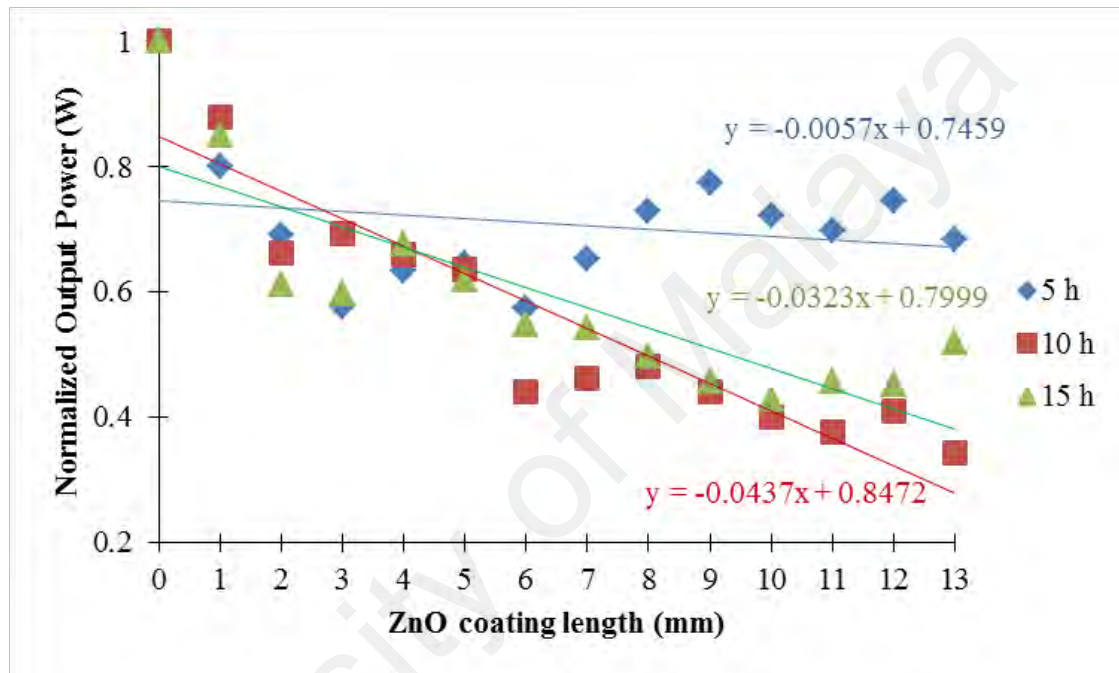


Figure 3.26 Optical measurements of the ZnO nanorods coated on glass substrate for the output intensity measurement at different lengths of ZnO coating.

In relation to the intensity losses presented earlier, light scattering coefficient of each sample was analyzed from the output intensity power with respect to the input incident power. The responses of the scattering coefficient with respect to the ZnO nanorod coating lengths are shown in Figure 3.27. The effect of the ZnO coating length (L) on the scattering coefficient (α) can be derived from Eq. (1) by substituted x with L as

$$\alpha = \frac{-\ln(I/I_o)}{L} \quad (3.3)$$

We observe from Eq. (6) that α is inversely proportional to the length of the ZnO coating, L , which indicates that α reduces as the length of the ZnO coating increases in the light transmission path. However, the output intensity (I) also reduces as the length of ZnO coating increases due to higher leakage by forward scattering of nanorods as it interacted with multiple point of glass-ZnO interface. Therefore, the value of α is expected to be constant throughout the respective length of coating. Figure 3.27 shows the scattering coefficient of the fabricated samples at different coating lengths. At the beginning of the ZnO nanorod coated substrate, the value of α for all the samples were at the peak which indicates the highest leakage of light due to the starting of forward scattering by nanorods. As the length of coating varies, the scattering coefficient responses on all samples were slowly stable and consistent towards the end of the coated layer. There were some fluctuations in the coefficient values observed at certain length of coatings on the samples due to non-uniformities in the coating as explained earlier. The values of α on all samples begin to be consistent from the middle towards the end of coating. Therefore, the average α for each growth time were calculated to be at 0.05, 0.1 and 0.08 for the growth time of 5 h, 10 h and 15 h correspondingly, as shown in Figure 3.28.

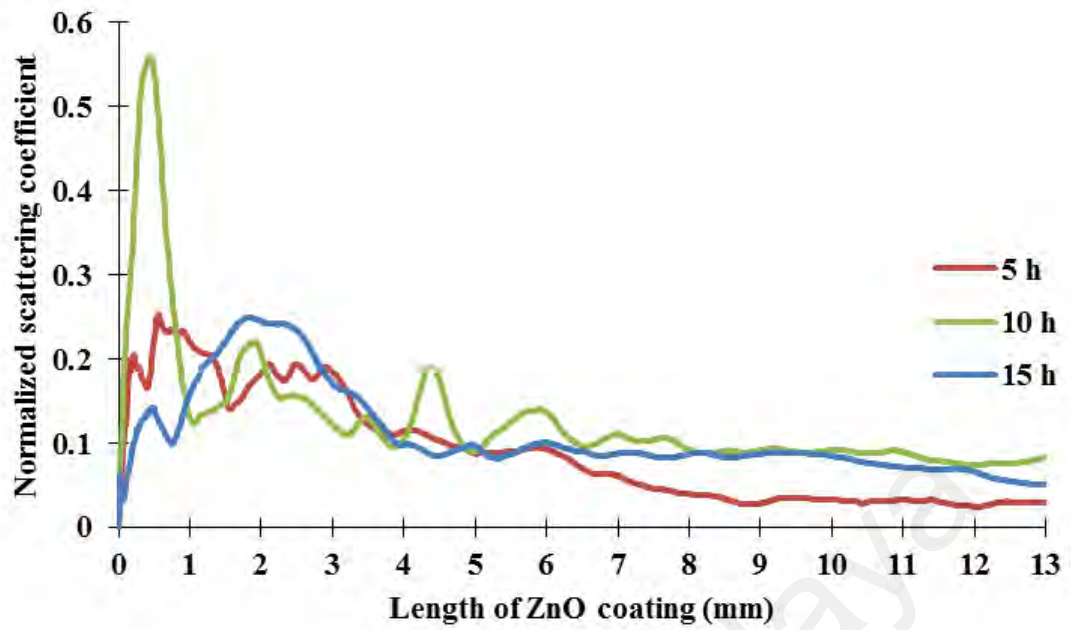


Figure 3.27 Optical measurements of the ZnO nanorods coated on glass substrate for the scattering coefficient at different lengths of ZnO coating.

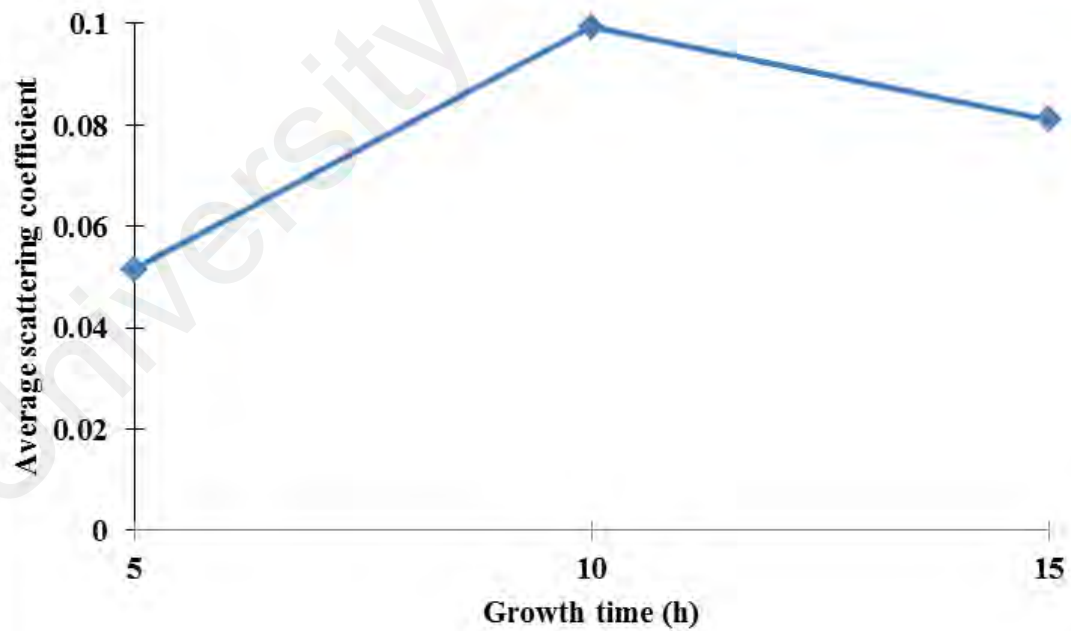


Figure 3.28 Average scattering coefficient for glass substrate coated with ZnO nanorods at 5 h, 10 h and 15 h growth times.

3.6 Measurement of Forward and Backward Scattering by ZnO Nanorods

In this section, the measurement of the forward and backward scattering by ZnO nanorods is presented as shown in Figure 3.29. This measurement was performed to observe the effect of growth time on forward and backward scattering by ZnO nanorods. As discussed in the previous section, both forward and backward scattering by the ZnO nanorods affect the output intensity of the guided light in the glass substrate measured at the end of the medium. Theoretically, backward scattering would dominate as the growth time increases. Figure 3.30 shows the experimental setup for the measurement for both forward and backward scattering. Forward scattering measurement was done by placing a white light source at the bottom of the glass substrate. The light was shined through the ZnO nanorods coating and a light detector was placed in an angle of 45° opposite to the tips of ZnO nanorods as shown in Figure 3.30(a). The setup for the measurement of backward scattering is shown in Figure 3.30(b). For backward scattering measurement, the source light was placed at the opposite of the tips of ZnO nanorods and the light detector was placed beside the light source at an angle of 45° .

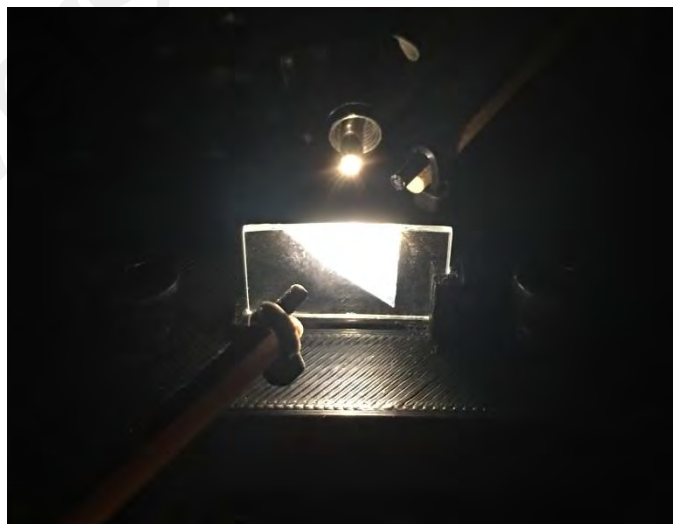


Figure 3.29 Measurement for light scattering by ZnO nanorods.

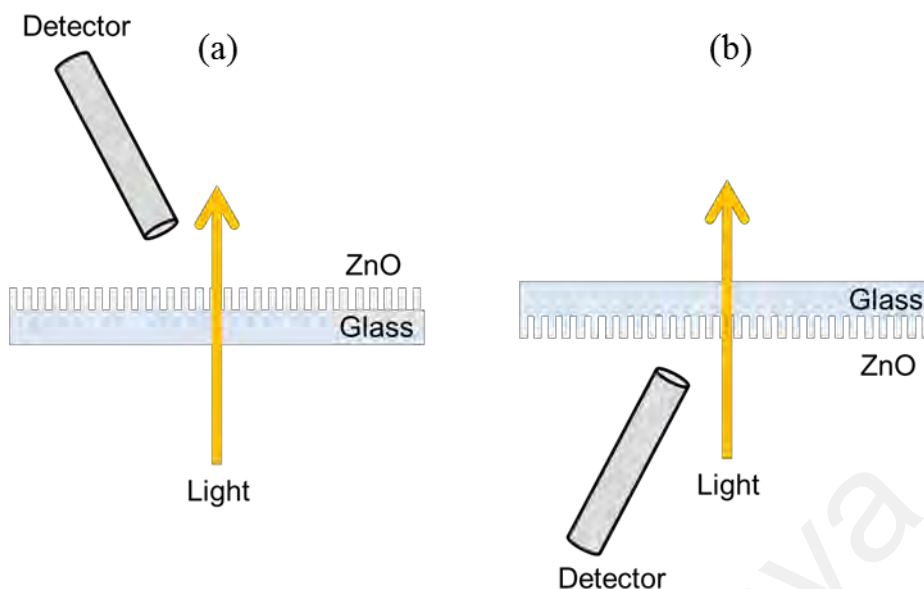


Figure 3.30 Experimental setup for light scattering by ZnO nanorods measurement for (a) forward and (b) backward.

Figure 3.31 shows the forward scattering by ZnO nanorods measurement recorded for three different samples with growth durations of 5 h, 10 h and 15 h each. It was observed that all three samples were having similar trend where the forward scattering reduced as the growth time increased from 5 h to 15 h. It was optically observed in Figure 3.14 of the previous section that the physical ZnO coating on glass substrate with 5 h growth time possesses the most transparent as compared to the other two. Therefore, higher forward scattering was observed at 5 h and subsequently reduced when the growth time prolonged to 10 h and 15 h correspondingly.

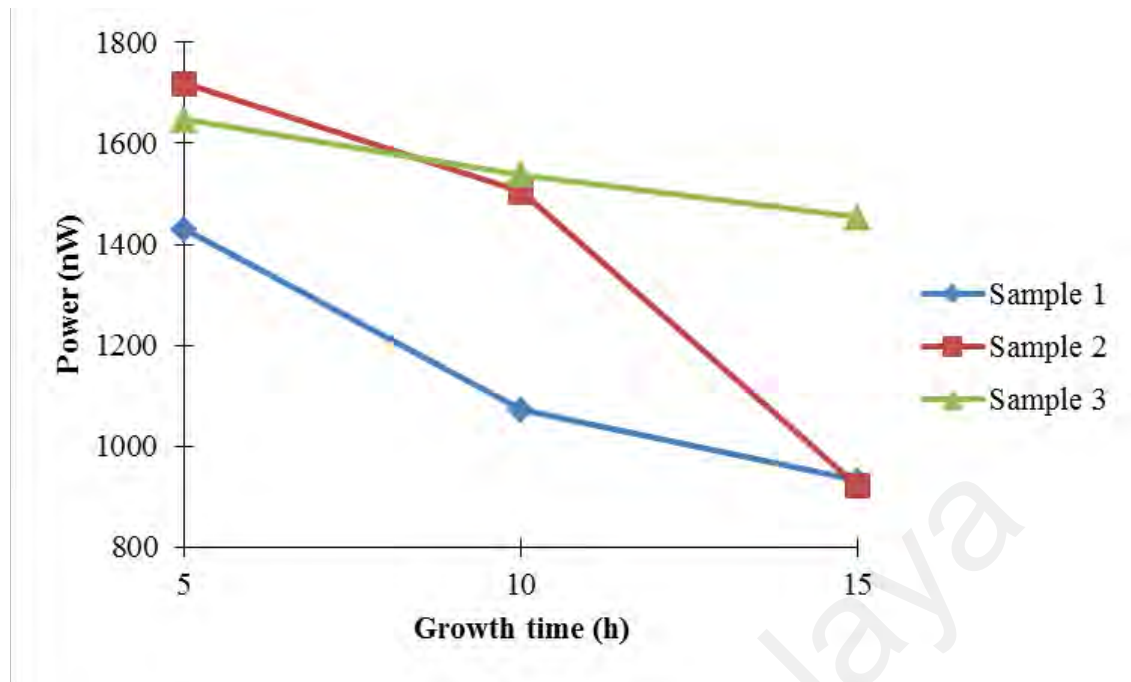


Figure 3.31 Forward scattering of the ZnO nanorods at growth durations of 5 h, 10 h and 15 h.

The measurement of backward scattering on the same tested samples is shown in Figure 3.32. It was found that the backward scattering by nanorods increases as the growth time increased from 5 h to 15 h for all three samples. This shows that at higher growth duration, the higher amount of light reflected by the ZnO nanorods. It was worth mentioning that the trend of backward scattering has a direct relationship to the forward scattering as presented earlier. Growth time changed the structure of the ZnO nanorods in which at longer growth rate caused backward scattering to dominate. Thus, backward scattering increased subsequently the reduction of forward scattering observed on all tested samples.

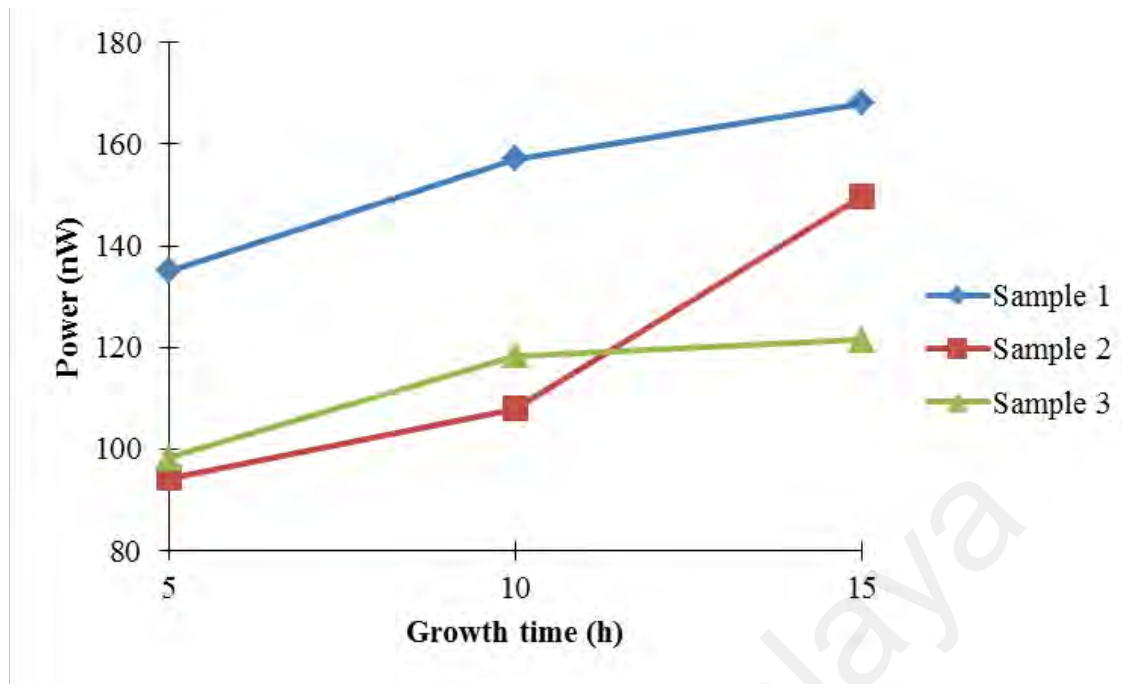


Figure 3.32 Backward scattering of the ZnO nanorods at growth durations of 5 h, 10 h and 15 h.

3.7 Summary

ZnO nanorods were fabricated in triangular shaped via hydrothermal method on glass substrate at growth durations of 5 h, 10 h and 15 h. It is found that the longer ZnO coating length exhibits higher leakage of light due to multiple interaction points of travelled light at glass-ZnO interface. This work also reported the amount of light leakage dependent on the growth times. The ZnO nanorods profiles such as length, diameter and density changed by different growth time which affected the scattering patterns of the nanorods. The sample coated with 10 h growth time exhibited the highest scattering loss via ZnO nanorods as compared to 5 h and 15 h. The successful fabricated samples with the variations of coating length and growth time will be further characterized in the next chapter for the analysis of dynamic range maximization model towards humidity sensing.

CHAPTER 4: MAXIMIZATION OF OPTICAL DYNAMIC RANGE FOR HUMIDITY SENSING BY CONTROLLING GROWTH OF ZINC OXIDE NANORODS

4.1 Introduction

The unique properties of ZnO in optical, magnetic, electrical and mechanical characteristics makes it an attractive choice of material for various applications such as in gas and chemical sensors, superconductors, photocatalysis, optoelectronic devices, biomedical, agricultural applications, amongst others (Chauhan *et al.*, 2016; Kulkarni *et al.*, 2015). It is commonly used as gas sensitive elements due to the changes in conductance upon the adsorption of gas molecules on the surface (Suchorska-Woźniak *et al.*, 2016). In humidity sensing application, ZnO nanostructures have high surface to volume ratio which enhances the potential for the adsorption of water molecules on its surfaces (P. Bhattacharyya *et al.*, 2007). Most of optical humidity sensor studies were done on optical fibers, either silica or polymer type, where one-dimensional ZnO nanostructures such as nanorods were grown on the curved surface of the optical fibers. Growth of nanorods on flat surfaces such as glass substrate (Umar *et al.*, 2009) provides better control during the growth process thus increase the surface area for humidity sensing (S.-B. Wang *et al.*, 2012).

Although the growth of nanorods on flat surface of glass substrate promises better uniformity compared to curved surface, the physical nanostructures of ZnO are difficult to consistently achieved at all times. Despite the synthesis was done under similar growth conditions, the sensitivity of the growth process causes inconsistencies of the nanorods physical dimension from batch to batch process. Therefore, it could lead to inconsistencies in sensing performance although the device is optimized on specific growth parameters such as growth time, temperature or concentrations.

This chapter presents the analysis of optimum operating condition of the fabricated sensor device which delivers promising sensing device performance regardless of growth conditions or surface coverage. This signifies that the device would perform at its best sensing performance as long as it meets the optimum working conditions. However, the ZnO nanorods growth time and coverage area are required to be first determined in order to realize the optimum working conditions. Thus the effects of the length of the coated ZnO nanorods depending upon the hydrothermal growth time are studied explicitly to better understand the system response over the desired limits of operation. Maximizing the effective scattering/attenuation coefficient of the nanorods layer does not necessarily result in the best performance particularly when considering intensity modulation. Instead, one needs to maximize the dynamic range of operation between two limits (i.e. dry condition or normal room humidity and maximum achievable level in the case of study) to achieve higher sensitivity.

4.2 Humidity Characterization

In order to maximize the dynamic range of the sensor device, the humidity sensing behavior was first conducted on the fabricated samples with respect to ZnO coating lengths and growth durations. In this work, the previous fabricated glass substrates coated with triangular shaped of ZnO nanorods layer were used as sensing device. Figure 4.1 shows an illustration of the top view of the setup for humidity measurements with the fabricated glass substrate. The similar equipment setup in Figure 3.18 was used in this experiment so that the ZnO nanorods coating length can be varied during the humidity characterization. In order to create humid environment, the experimental setup was placed inside a humidity chamber with the dimension of 0.35 m x 0.22 m x 0.23 m. A hygrometer was mounted on the wall of the chamber as a

reference to determine the actual humidity level inside the chamber during the experiments.

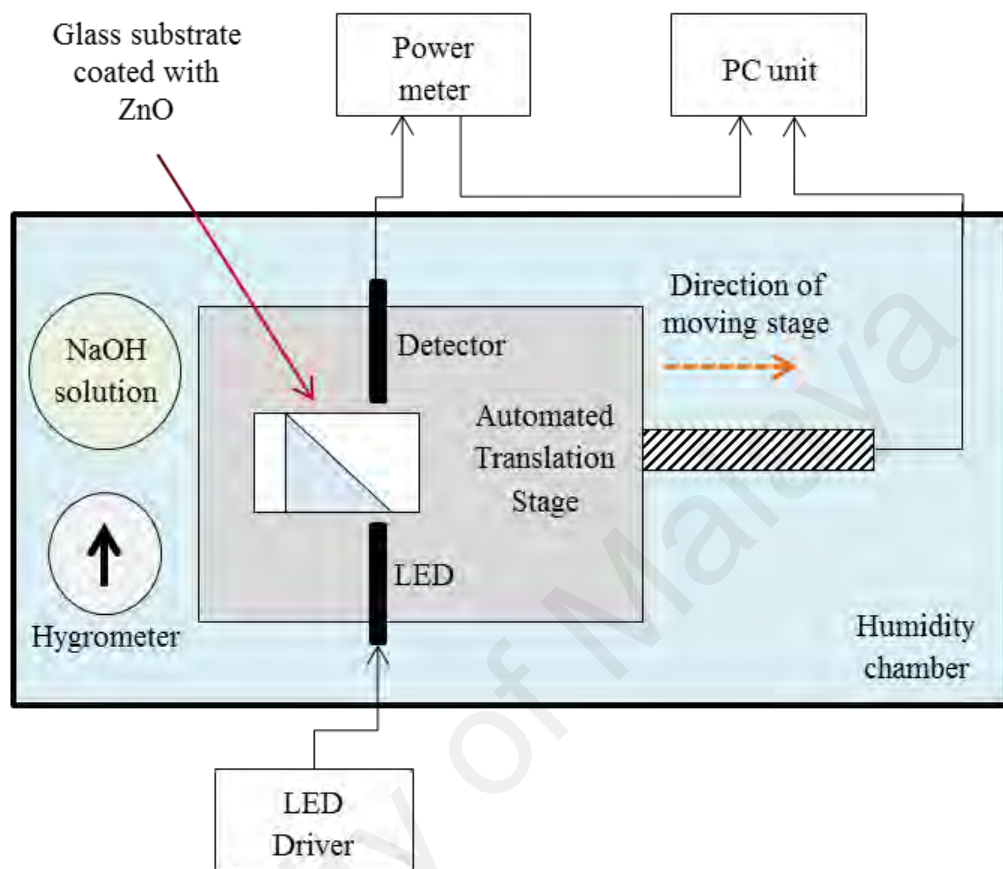


Figure 4.1 Schematic representation of the experimental setup for humidity testing.

The fabricated ZnO coated glass substrate was placed on the automated translation stage in between the aligned LED and detector. The humidity level of the chamber was increased from 50% (room level) to 80% at a constant temperature of 25 °C by placing a mixture of sodium hydroxide (NaOH) and water inside the chamber. The lid of the chamber was then closed and the humidity level of the chamber was monitored. The output intensity power of the fabricated sample was recorded at every 5% as the humidity increased from 50% to 80%. The measurement was done at four different locations on the glass substrate by sweeping the automated translation stage

along the edge of glass substrate to cover the variation of coating length of ZnO nanorods layer. The coverage for the coating lengths in this experiment were done at 1 mm, 4 mm, 7 mm and 10 mm as shown in Figure 4.2. The measurement was repeated for all samples grown with different processing times. The sensing response for each samples were then analyzed by comparing the power of the output intensity at every recorded humidity levels with respected to the 50% RH.

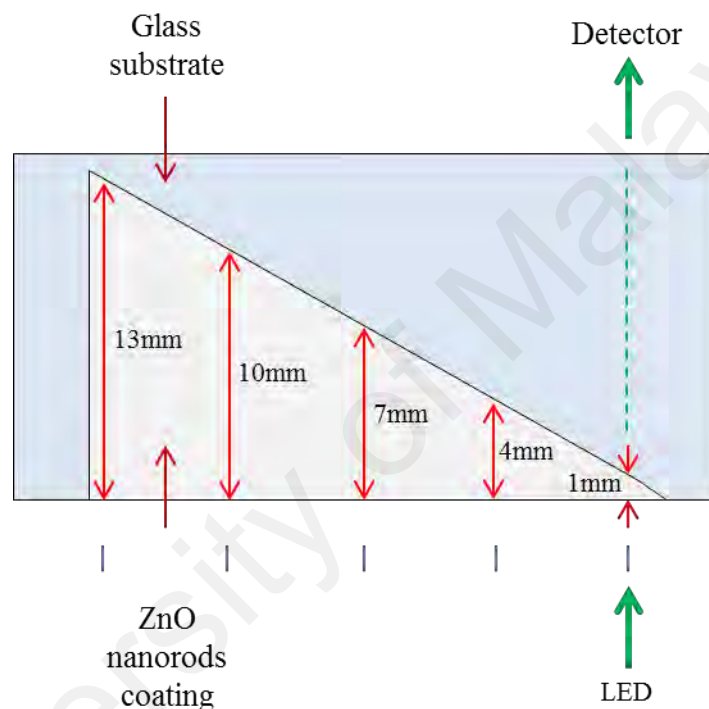


Figure 4.2 Four different coating lengths coverage for humidity characterization.

Figure 4.3 shows the sensing response of the fabricated devices towards humidity measured at four different coating lengths. The value of optical transmission difference (ΔT) represented the amount of light transmitted by the sensor device when the humidity was varied from 50% to 80% RH levels. The ΔT was obtained by the amount of optical power reduction at every length of ZnO coating with reference to non-coated region on all samples. On the whole, the results show the sensing response

increases with the increment of ZnO coating length. However, it was found that the sensing response for the sample with 5 h growth time was unstable especially at the shorter coating length in between 1 mm and 7 mm as shown in Figure 4.3(a). This behavior was due to the structure condition of ZnO nanorods structure grown under this growth duration. From the SEM images in previous chapter, it was observed that there was a very thin layer of ZnO coating when it was grown for 5 h compared to longer growth times. The growth of ZnO nanorods under this processing time shows some parts of the coatings were not properly grown where the length of the nanorods were short and not well uniformed. Therefore, inconsistencies reading were observed on this sample. In spite of that, it eventually showed improvement and significant sensing trend when the coating length increased to 10 mm. On the other hand, the samples grown for 10 h and 15 h which correspondingly presented in Figure 4.3(b) and Figure 4.3(c) show better sensing stability and consistency. This is due to better elongation of ZnO nanorods compared to 5 h. It was found that both samples (10 h and 15 h) showed significant sensing response of having higher intensity loss when the coating length increased from 1 mm towards 10 mm. Among all the samples, the highest sensing responses were found to be consistent at 10 mm of coating length when tested at the highest achievable humidity. This shows that the longer length of ZnO coating section provides larger sensing surface thus significantly enhances the sensing response and its sensitivity.

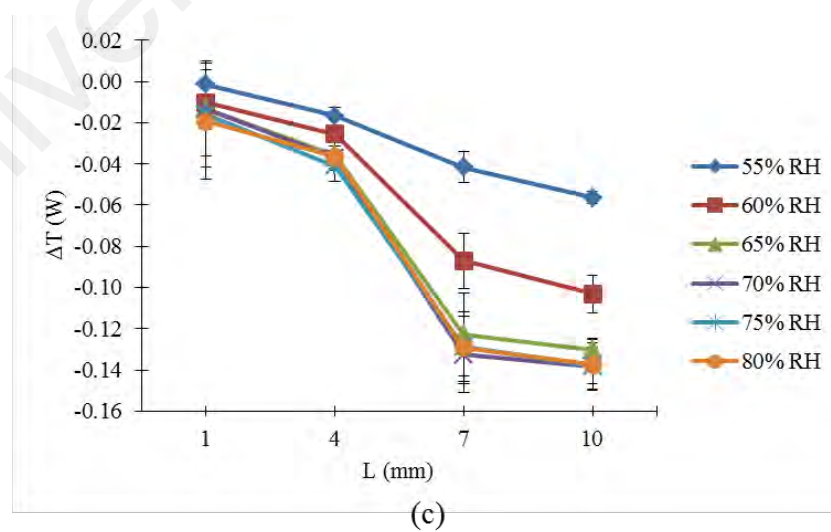
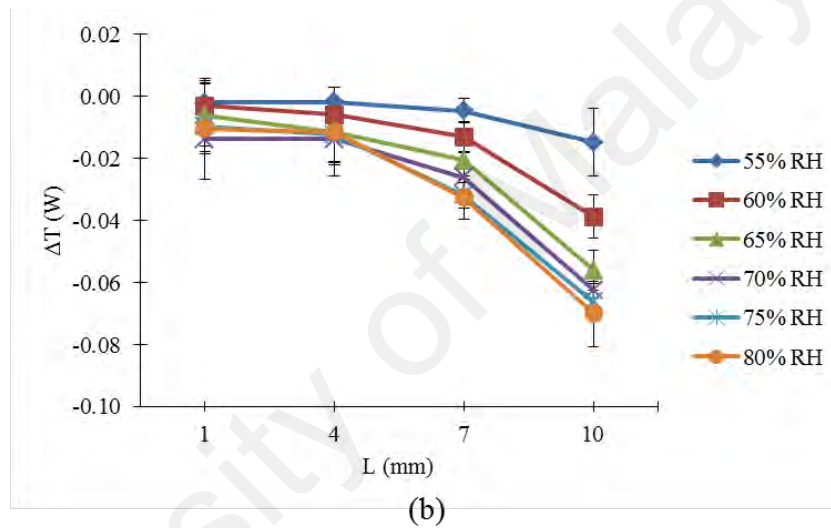
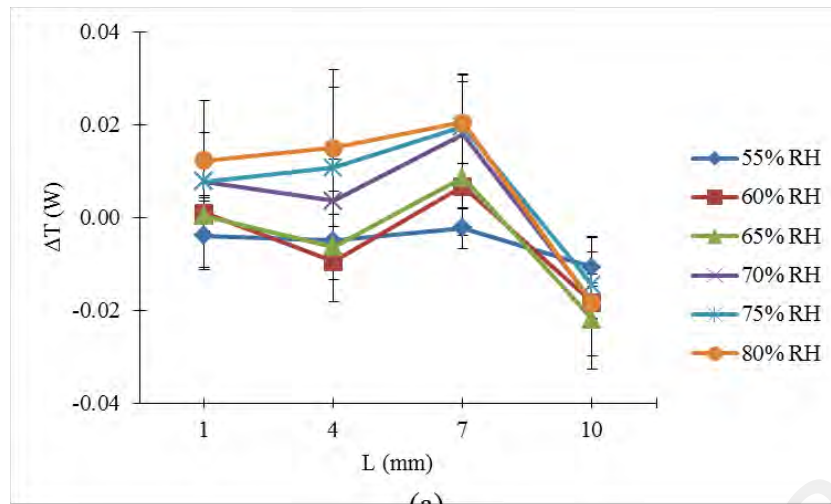


Figure 4.3 The response of humidity sensing on fabricated glass substrates at growth durations of (a) 5 h, (b) 10 h and (c) 15 h.

The results presented show that the presence of humid environment induced higher leakage of light via ZnO nanorods when it is used as sensing sensitive material. Generally, the detection mechanism by ZnO nanorods towards humidity is based on two approaches. The main contribution to this sensing mechanism is established by the adsorption and desorption process of water molecules on the surface of ZnO nanorods (Kim *et al.*, 2005). Adsorption is the process of adhesion of atom, ions or molecules from a gas, liquid or dissolved solid onto a surface. This process forms a thin layer of adsorbate (for this case is water molecules) on the surface of adsorbent (ZnO nanorods). Water molecule is commonly considered as adsorbate on the surface of semiconductor as it is consistently present at ambient condition and influence significantly on electronic properties and surface stability (Ye *et al.*, 2013). Figure 4.4 illustrates the schematic diagram for adsorption of water molecules on ZnO nanorods surface. ZnO is one of metal oxide materials which has ability to adsorbs water molecules physically and chemically (Morimoto *et al.*, 1970). Although at atmosphere level, it chemisorbs water molecules to form groups of surface hydroxyl (OH) on which further water molecules are adsorbed physically through hydrogen bonding (Nagao, 1971). ZnO surface contains varying proportion of O^{2-} , O^- , Zn^+ and Zn^{2+} ions depending on non-stoichiometry degree which acts as active area for adsorption process of water molecules (Sengupta *et al.*, 1979).

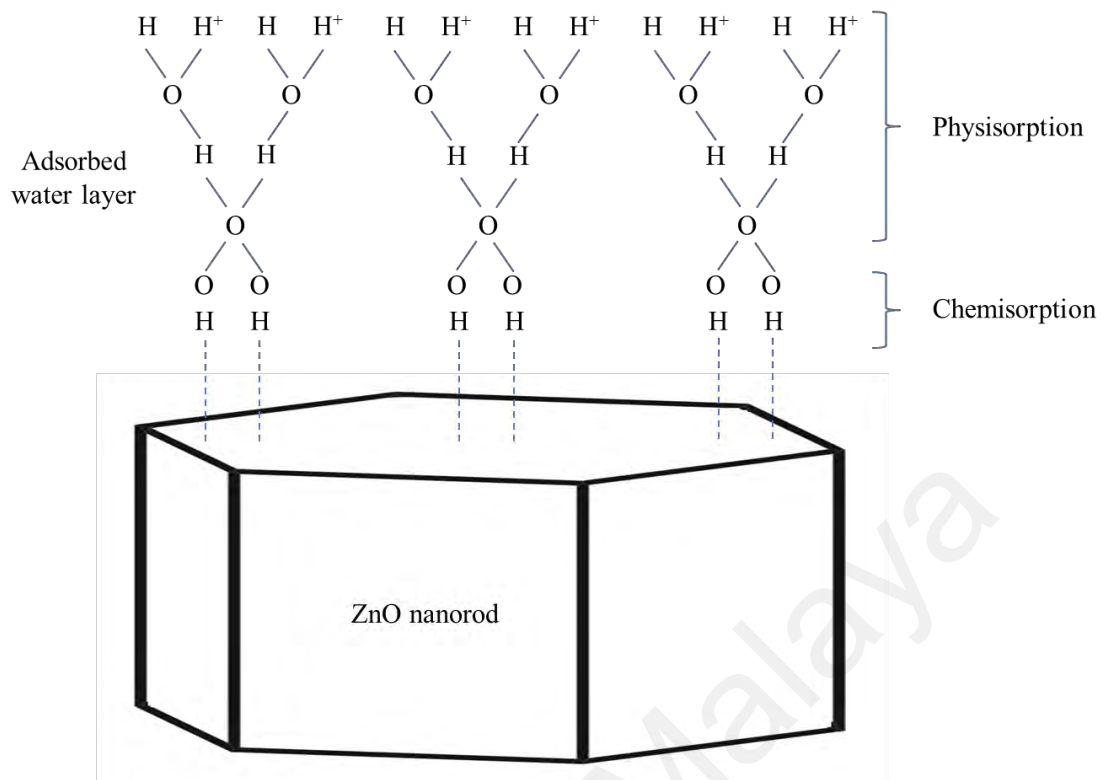


Figure 4.4 A schematic diagram for adsorption of water molecules on ZnO nanorods surface.

In the case of adsorption process onto the surface of ZnO nanorods, there were several works reported that the changing in electrical conductivity of the material was observed in response to the adsorbed water molecules on its surface (D. Bhattacharyya *et al.*, 1977; Zuraidah Harith *et al.*, 2015; Horzum *et al.*, 2011; Salah *et al.*, 2014). Rackauskas *et al.* (Rackauskas *et al.*, 2017) explained in the study that oxygen which adsorbed on the surface of ZnO becomes negative charged (O^- , O_2^- or O^{2-}) and extracts electrons from ZnO surface. This phenomenon will caused the surface region that losses electrons become surface charge depletion layer thus affect the effective conduction channel of the material (Rackauskas *et al.*, 2017). The changes in electrical conductivity of a material (ZnO) altered its complex refractive index which subsequently changes the scattering patterns of the material.

Since light is an electromagnetic wave which is having oscillating electric field, it is known that the refraction index (n) is direct proportional to dielectric constant (ϵ_r) of a medium which expressed as

$$n = \epsilon_r^{1/2} \quad (4.1)$$

In an oscillating electric field, the dielectric constants are having frequency dependence and its complex function is expressed as (Bass *et al.*, 1995)

$$\epsilon(\omega) = \epsilon'(\omega) + i\epsilon''(\omega) \quad (4.2)$$

where ϵ' and ϵ'' are the real and imaginary part of dielectric constant, respectively. As the dielectric constant has frequency dependence complex number, the index of refraction would also have its complex expression. The complex refractive index (N) can be expressed as (Bass *et al.*, 1995; Bohren *et al.*, 2008)

$$N = n + iK \quad (4.3)$$

where K is the imaginary part of complex refractive index. Therefore, by substituting Equations (4.2) and (4.3) into (4.1), the relation between the complex refraction index and complex number of dielectric function can be written as (Bohren *et al.*, 2008)

$$(n + iK)^2 = \epsilon' + i\epsilon'' \quad (4.4)$$

In optical properties of a material, conductivity (σ) is closely related to dielectric function (ϵ). The electric current density (J) and electrical displacement field (D) in frequency domain are correspondingly given as (Bohren *et al.*, 2008)

$$J(\omega) = \sigma(\omega)E(\omega) \quad (4.5)$$

$$D(\omega) = \varepsilon(\omega)E(\omega) \quad (4.6)$$

Both Equations (4.5) and (4.6) are linked to electrical field vector (E). From the equations, the conductivity in terms of imaginary part of complex dielectric function is expressed in the following equation

$$\sigma(\omega) = \omega \cdot \varepsilon''(\omega) \quad (4.7)$$

Hence, the complex dielectric function of a material can now be written in a function of conductivity as

$$\varepsilon(\omega) = \varepsilon'(\omega) + i \frac{\sigma(\omega)}{\omega} \quad (4.8)$$

It is noted that according to Equation (4.4), the changing of the conductance value of a material affect the value of its complex refraction index. In semiconductor materials, the value of conductance varies depending on the doping process of the materials. In the context of utilization of ZnO as a sensing material for humidity detection, the conductivity of the material diverges upon the amount water molecules adsorb by the surface of nanorods. This resulting an alteration of its complex refraction index thus changes the optical properties of the ZnO nanorods in response to the detection of humidity concentrations. As the optical properties change, the scattering patterns of the nanorods are subsequently modified.

Besides the alteration of ZnO electrical properties, the variation of the surrounding refractive index of nanorods also contributes into optical scattering behavior. In general, the refractive indices of air and water are known to be 1.00 and 1.33 correspondingly. In the presence of humidity concentrations, the refractive index of humid air varies in the range between 1.00 and 1.33 (Mehrabani *et al.*, 2011) as shown

in Figure 4.5. The variation of the refractive index of humid air (n_{humid_air}) surrounding the ZnO nanorods affected the light scattering at the interface between ZnO and air. Due to this condition, it contributes into light intensity change in response to humidity concentrations.

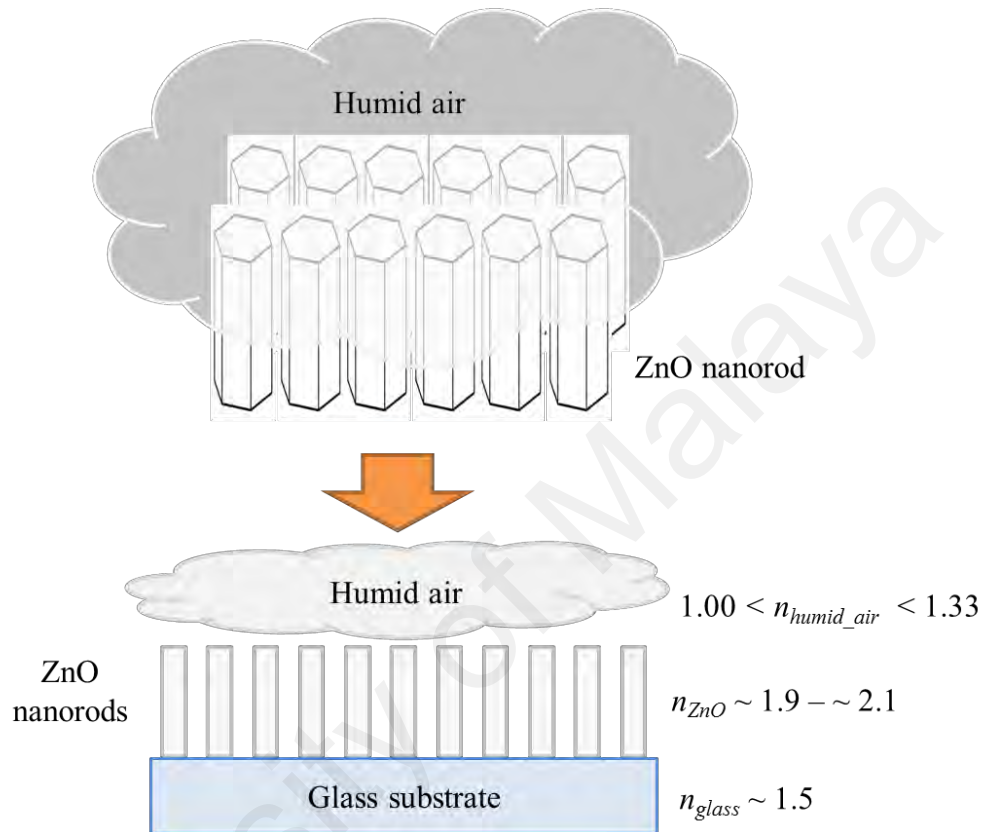


Figure 4.5 Refractive index of air varies towards humidity concentrations.

As explained earlier, since the humidity sensing is based in the adsorption and desorption process by the surface of ZnO nanorods, the surface area of the nanorods play an important role to determine the performance of the sensing device. The larger surface of the ZnO nanorods enhances the adsorption of water molecules on its surface thus improved the sensitivity of the sensor device (Bhattacharya *et al.*, 2015). The surface area of the ZnO nanorods is determined by its length and diameter which are varied by the growth processing time. In Chapter 3, the length and diameter of the nanorods were both increased as the growth time increases from 5 h to 15 h. The changing in nanorods size reflects the sensing performance of the fabricated samples.

Figure 4.6 summarizes the humidity response for the samples which grown at 5 h, 10 h and 15 h. The result indicates that the glass substrate grown with 15 h has the highest sensing response compared to both 5 h and 10 h at all ZnO coating lengths (1 mm to 10 mm). This shows that the glass substrate coated with ZnO nanorods at longer growth time which has larger surface area induced higher leakage of light in detecting the humidity concentrations. In the presence of humidity, typically it reduces both forward and backward scattering schemes. The responses of the sensor show that the backward scattering are found to be dominant as the growth time increased from 5 h to 15 h. Thus, a reduction of transmitted light was observed with the increasing of humidity levels. In this result, it was found that the glass substrate coated with 15 h growth time produced the highest humidity sensing response where the ΔT was observed at -0.1374 W. The ΔT values for the glass substrate with 10 h and 5 h were respectively lower and measured at -0.0699 W and -0.0184 W. All these values were measured at humidity concentrations of 80% RH and at the coating length of 10 mm.

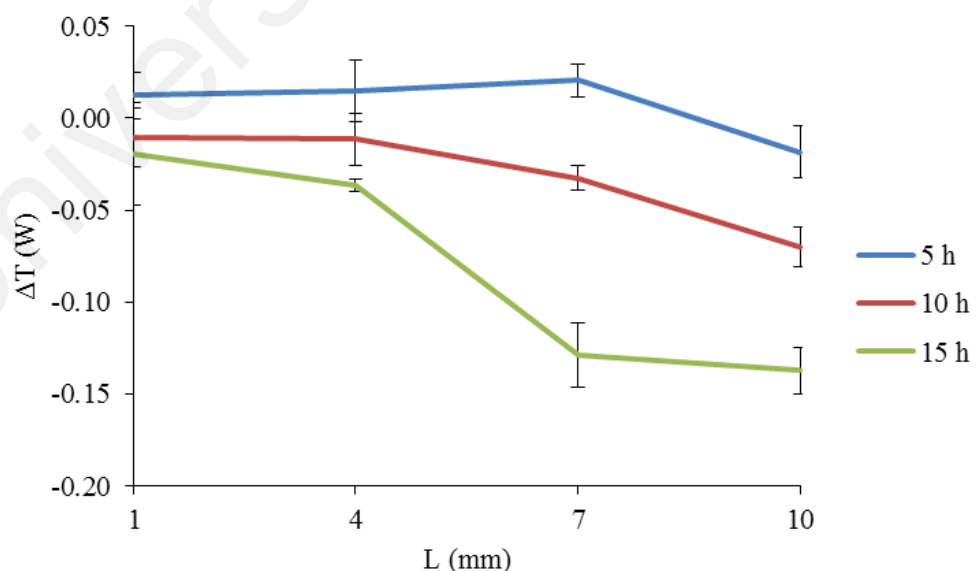


Figure 4.6 Comparison of humidity response at 80% RH concentrations for samples with different processing time.

Although the results presented earlier shown that the highest humidity response was observed on the coated glass substrate fabricated with the combination of ZnO growth condition of 15 h (growth time) and 10 mm (coating length), it does not necessarily mean that the mentioned ZnO growth settings are the optimum. This is due to the value of sensing response is not easily being replicated at all times as variation in physical structures of nanorods occurs from batch to batch fabrication process. Despite the fact of having several devices fabricated in the same batch, the variations are still exist between the samples. This can be seen as depicted in Figure 3.17 where there are slight variations in terms of nanorods length and diameter across all growth times. The deviation trend was also observed in the previous work by Bora et al. (Bora *et al.*, 2014) which the diameter of the ZnO nanorods significantly shows large variations at every growth durations. The deviation happened due to the sensitive synthesis process and this affects the sensing performance of fabricated devices from one to another. Meaning that, similar sensing response may not be achievable although they are fabricated under the same growth parameter. Besides, it is worth mentioning that a device that is fabricated with different combinations of growth setting may perform with the same amount of sensing response of a specific growth condition.

The data in Figure 4.6 shows that there were similar sensing responses can be achieved by different growth conditions. In this work, the growth condition of ZnO nanorods is based on two parameters which are the growth time and the length of coating segment. Therefore, these parameters can be dynamically varied in order to obtain a similar sensing response. Figure 4.7 shows the humidity sensing with two different growth combinations of ZnO nanorods exhibited approximately same amount of sensing response. The sample fabricated with growth time of 10 h and coating length (L) of 7 mm had obtained an amount of -0.0326 W while the sample with growth time of 15 h and coating length of 4 mm was having a total response of -0.0366 W. This

graph indicates that although the sample was grown at shorter growth time, the longer coating section provides more interaction of ZnO nanorods towards humidity. Thus, it has similar light scattering amount with the sample that having longer growth time but shorter coating region.

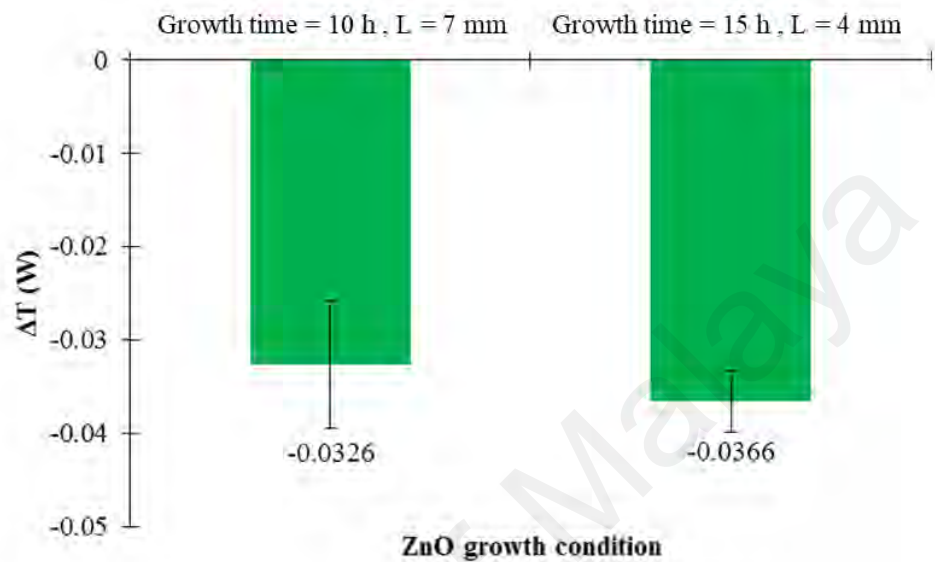


Figure 4.7 Sensing responses on two different growth combinations of ZnO nanorods.

Despite the fact that the growth time or coating length can be used reference for achieving an optimum sensing response, it may not be an effective method in determining a standard reference for maximum sensing response of sensor device. Therefore, an analysis on optimum working condition of fabricated sensing device by maximizing the optical dynamic range is needed to achieve higher sensitivity towards humidity sensing.

4.3 Dynamic Range Maximization Model

To realize the analysis, the proposed ZnO nanorods coating grown in triangular shape on glass substrate was shown in Figure 4.8. The main purpose of the triangular form is to serve the variation of the ZnO coating length (L) along the propagation

medium between the light source (LED) and detector as they move along edges of the glass substrate.

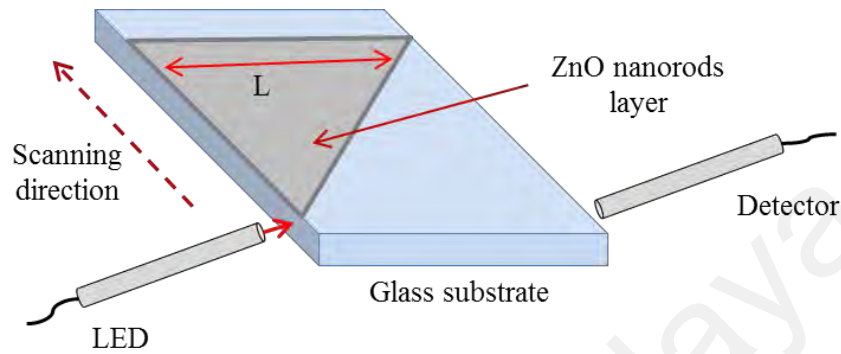


Figure 4.8 Schematic representation of the fabricated device including the detection scheme.

Figure 4.9 shows the proposed model where uniform ZnO nanorods grown on a glass substrate is considered. The coating length is L and the nanorods forward scattering coefficient is α . A light source is applied at one end of glass substrate while the output is measured by a light detector at the other end. Light guided in the glass substrate is assumed to decay exponentially due to forward scattering by the ZnO nanorods. The transmittance, T measured by the output detector is expressed as (Husain *et al.*, 2013),

$$T = \frac{I}{I_0} = \exp(-\alpha L) \quad (4.9)$$

where I_0 is the intensity of the light entering the medium or sample while I is the intensity of the light leaving the medium.

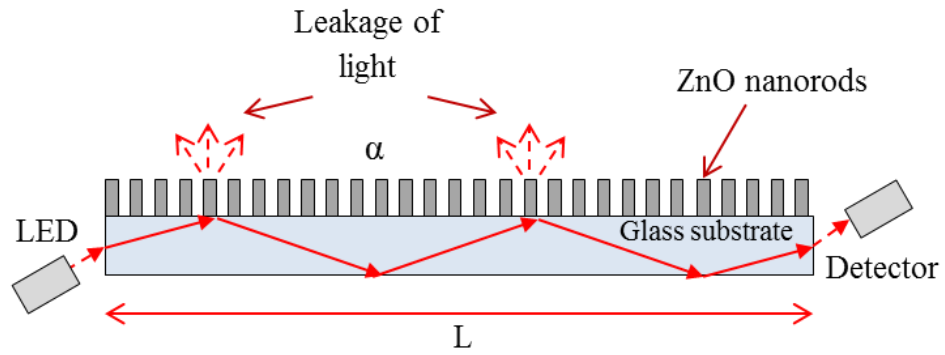


Figure 4.9 Schematic representation of the sensor showing the substrates coated with ZnO nanorods.

Figure 4.10 schematically represents the transmittance for two different limits: maximum humidity (T_{max}) and minimum humidity (T_{min}). With rise in humidity levels, the effective index of the medium surrounding the nanorods increases, leading to a more prominent contrast in the refractive index differences between the ZnO rods and the medium. The forward scattering coefficient is expected to increase with a subsequent reduction in transmittance of light.

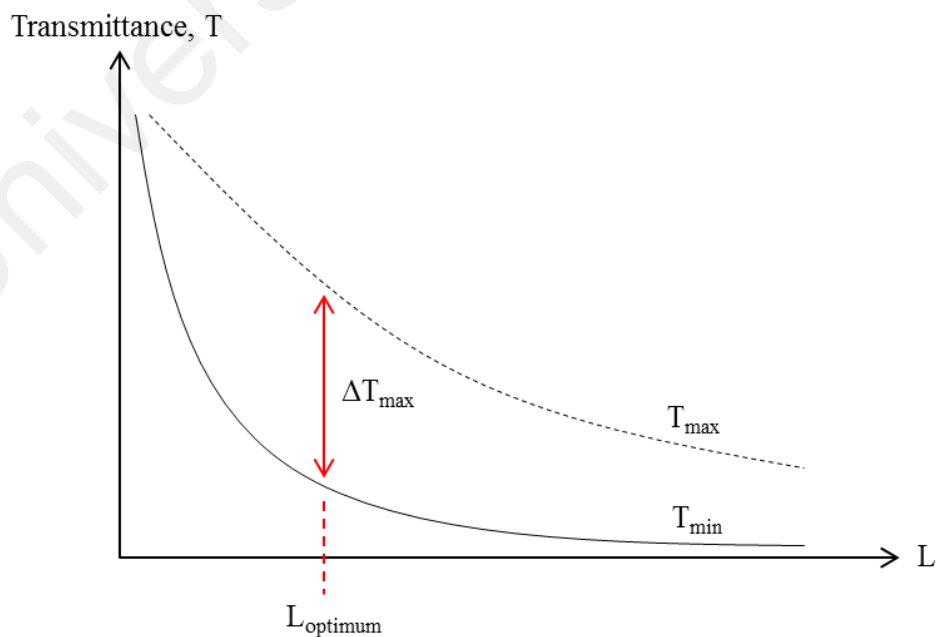


Figure 4.10 The dynamic range analysis for the optimum sensor device.

As shown in Figure 4.10, the target here is to control the length of the ZnO coating and scattering coefficient in order to maximize ΔT , which is the difference between the optical transmissions, T_{max} and T_{min} ,

$$\Delta T = \exp(-\alpha_1 L) - \exp(-\alpha_2 L) \quad (4.10)$$

where α_1 and α_2 are the scattering coefficients of the nanorods for the cases of maximum humidity and minimum humidity levels, respectively. To generalize the analysis, two normalized coefficients are introduced: normalized length, $Z = \alpha_2 L$ and normalized scattering coefficient, $\zeta = \alpha_2 / \alpha_1$. Therefore, Equation (4.10) can be simplified as

$$\Delta T = \exp\left(-\frac{Z}{\zeta}\right) - \exp(-Z) \quad (4.11)$$

The normalized length, Z_{max} , which results in a maximum dynamic range (ΔT_{max}) is derived from the derivative of Equation (4.11) with respect to Z

$$Z_{max} = \frac{\zeta \ln(\zeta)}{\zeta - 1} \quad (4.12)$$

and the maximum dynamic range as a function of ζ is

$$\Delta T_{max} = \zeta^{-\frac{1}{\zeta-1}} - \zeta^{-\frac{\zeta}{\zeta-1}} \quad (4.13)$$

The contour plot shown in Figure 4.11 depicts ΔT variation with respect to changes in Z and ζ . The dashed line represents Z_{max} calculated from Equation (4.12). Increasing the value of ζ (which depends only on scattering of light from the nanorods) both Z_{max} and ΔT_{max} increases. This means that as humidity levels increase, ζ becomes lower as α_1 increases. This results in reduced T value which can be translated as the loss of light intensity upon exposure to humidity. That does not necessary indicate increase in the length L as Z depends on α_2 (scattering at lower humidity limit). Hence, in the experimental part, both ZnO segment length L and scattering are varied.

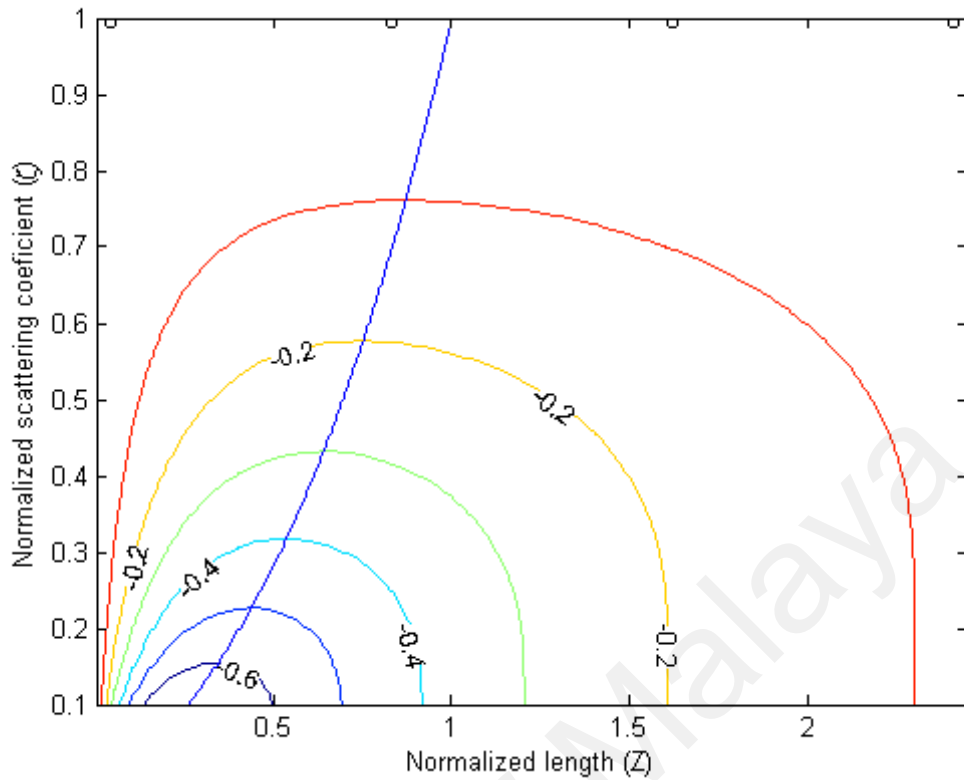


Figure 4.11 Contour plots for the dynamic range (ΔT) versus the normalized length (Z) and normalized scattering coefficient (ζ). The blue line running down from $Z = 1$ to 0.25 represents the values of $Z_{Optimum}$ obtained from Equation (4.12).

For the correlation with practical approach, more samples with the same growth condition were fabricated and characterized against similar humidity experiment in order to obtain more dynamic data between the two growth parameters. All the results were then recorded and analyzed. The values of α with respect to L were utilized in the dynamic range investigation of the fabricated device for humidity sensing experiments. α as in Equation (3.3) represents α_2 in the hypothetical model (Equation (4.10)), and thus the values of normalized length (Z) can be calculated and introduced as one of new scattering coefficients as discussed earlier in Equation (4.11). In the humidity sensing experiment, it was observed that the optical transmittance (T) was reduced as the humidity level increased from 50% to 80%. The reduction of transmittance was due to

an increase in α as the humidity increases consequently resulting lower power intensities captured by the power meter. The value of α at maximum humidity level represents α_1 in theoretical model; thus, the second scattering coefficient of the model which is the normalized scattering coefficient (ζ) can be determined. Since ζ is the ratio of α_2 to α_1 , therefore the value of ζ reduces as the humidity level increases. Henceforth, these two new scattering coefficients were used in subsequent analysis as discussed in the hypothetical model.

Figure 4.12 depicts the 3D contour plot for the dynamic range investigation of the fabricated samples. The contour plot demonstrates the relationship between the normalized length (Z) and normalized scattering coefficient (ζ) used to achieve the maximum dynamic range (ΔT) of the fabricated devices. The running down valley represented the value of ΔT . In the 2D version of graph as shown in Figure 4.13, darker blue and darker red regions indicate the lowest and highest values of ΔT , respectively. It was found that the optimum ζ for the highest achievable humidity level is ~ 0.3 which demonstrates that the scattering coefficient of ZnO nanorods increases by $\sim 233\%$ when the humidity level changed from 50 % to 80 %. The maximum response of the fabricated samples towards humidity sensing for the combination of growth conditions (growth time and length of coating segment) appears to form a valley running from Z value of ~ 1.42 (50% humidity level) to ~ 0.23 (80 % humidity level) of the graph where the most noteworthy ΔT was observed to be at ~ -0.38 . This number represents the reduction of the transmittance by $\sim 38\%$ in response to 80 % of humidity level with respect to 50 %. There are some incomplete data in the graph (darker red region) which was not obtained throughout the measurements. However, the data in the graph was good to show the formation of valley line which represents an ideal operating condition for fabricated sensor device towards humidity sensing. This implies that the optimum response for humidity sensing device can be achieved without being dependent to a

particular growth time and coating area but as long as the combinations of these growth conditions are tuned and meet the optimum point of operating condition, the device should be able to perform the sensing at its best.

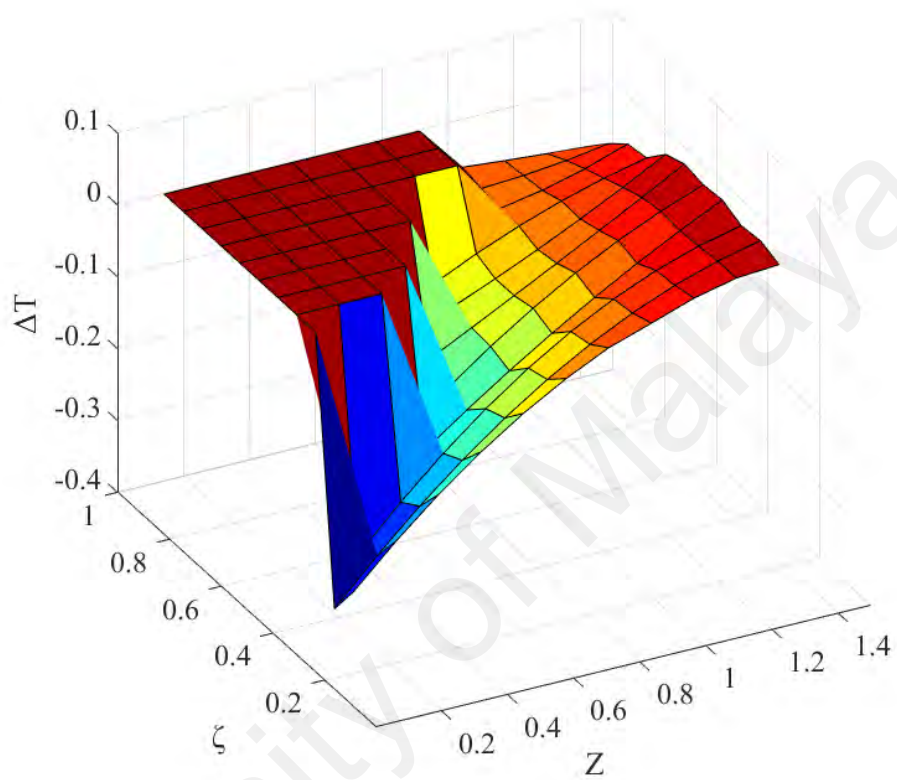


Figure 4.12 3D contour plot for dynamic range analysis.

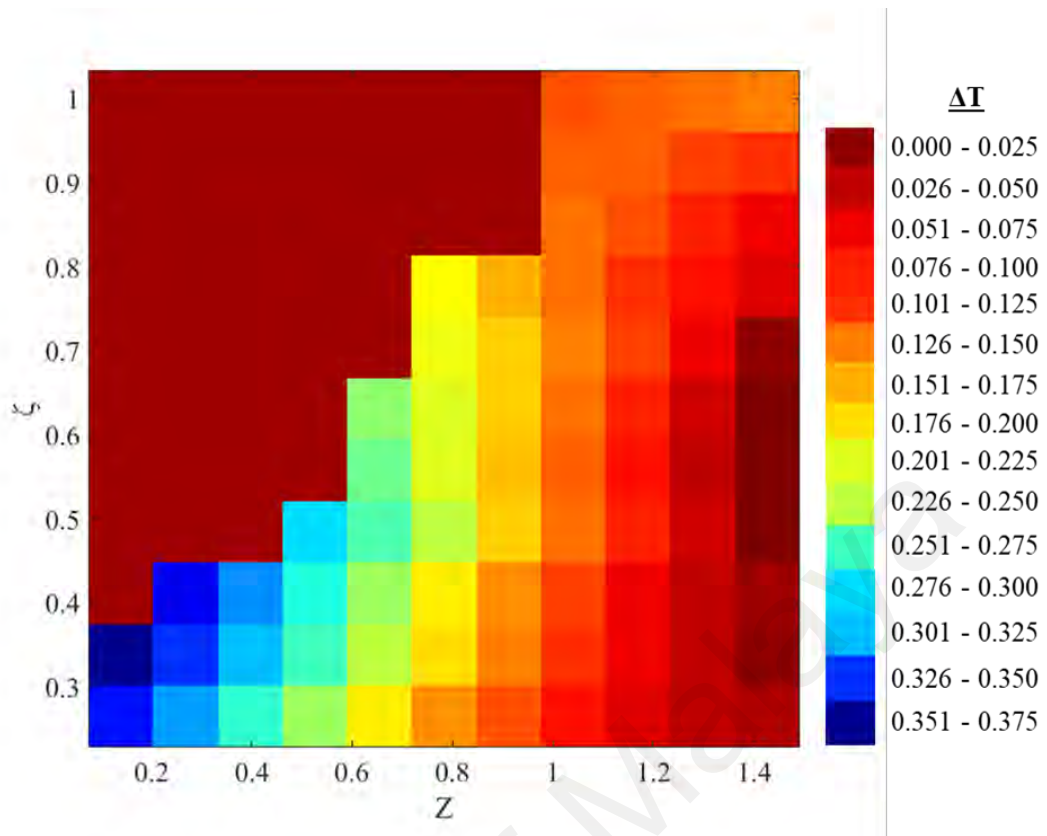


Figure 4.13 Experimental contour plots for the dynamic range (ΔT) versus the normalized length (Z) and normalized scattering coefficient (ζ).

In comparison to the hypothetical model presented earlier, the value of ΔT in Figure 4.11 was observed to be in between -0.3 and -0.4 matching very well to the experimentally determined value of ~ 0.38 . The trend line of optimum working condition demonstrates the Z value from ~ 1 (50% humidity level) to ~ 0.6 (80% humidity level) for the hypothetical model which shows the comparative trend of response between theoretical predictions and experimental observations. The slight discrepancies between theoretical and experimentally observed sensing characteristics are expected since the theoretical model was derived based on first principles approximation which considers uniform growth of ZnO nanorods, scattering coefficient of ZnO nanorods (α) and length of ZnO coating (L). There are several other parameters

that should be considered to refine future analysis as a second order approximation model such as incident angle and wavelength of light source could be accommodated.

The presented dynamic range model can be used as reference set for the development of sensing device in subsequent topic. In order to realize an integrated humidity sensing device, the fabrication of new glass substrate with fixed size of ZnO nanorods layer is needed. The fabricated sample will then be correlated with the dynamic range model to assess the state of its operating condition.

4.4 Fabrication of ZnO Nanorods Coating onto Glass Substrate for the Development of Humidity Sensing Device

Three glass substrates were prepared for the fabrication of ZnO nanorods by using the similar synthesis process as presented in Chapter 3. For these samples, fixed dimension of 10 mm x 10 mm of coating layer was proposed based on the previous humidity experiment which shown the maximum sensing response observed at 10 mm of coating length throughout all growth durations. Three growth durations of 5 h, 10 h and 15 h were covered in the fabrication process. In order to create a square shaped of the coating, the same PTFE tape was used to mask the samples as shown in Figure 4.14.



Figure 4.14 Sample masked with PTFE tape with square area exposed for ZnO coating.

The similar seeding and growth procedures were repeated for this fabrication process. Figure 4.15 shows the successful coated samples with square shaped ZnO nanorods layer. The optical images of samples grown with 5 h, 10 h and 15 h growth times are shown in Figure 4.15(a), Figure 4.15(b) and Figure 4.15(c) respectively. It clearly can be observed that the sample with 15 h has the densest ZnO nanorods coating as compared to 5 h and 10 h. The sample with 5 h has the least density of coating since the coating layer was more transparent than the others.

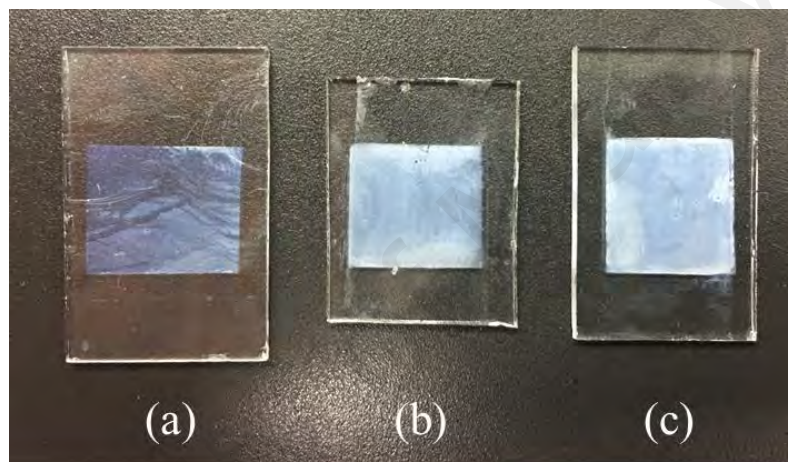


Figure 4.15 Successful glass substrate coated with square shaped ZnO nanorods for growth duration of (a) 5 h, (b) 10 h and (c) 15 h.

These fabricated samples were then experimentally characterized against humidity concentrations. The same experimental setup as shown in Figure 4.1 was used for the characterization except the measurement was done at a fixed position (no moving stage). The light source was excited at the same incident angle to the center edge of the glass substrate so that the light travels through the middle of the ZnO coating as depicted in Figure 4.16. All samples (5 h, 10 h and 15 h) were tested and the responses against humidity were recorded at 50% and 80% of RH concentration levels.

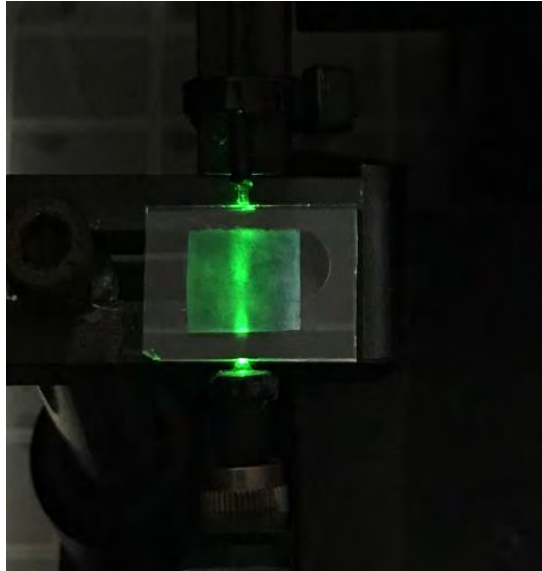


Figure 4.16 Humidity measurements on the new fabricated samples at fixed position of stage.

Figure 4.17 shows the response of the fabricated samples against humidity at 80% of RH level with respect to 50%. It was observed that the sample with 15 h growth time produced the highest sensing response towards humidity concentrations in comparison to 10 h and 5 h, respectively. Correspondingly, the amount of transmittance power reduction was found to be at -0.2977 W, -0.2134 W and -0.0535 W for the samples with growth time of 15 h, 10 h and 5 h as shown in Figure 4.18. The sensitivity of the detection for the sample with 15 h growth time exhibited the highest with the value of -0.0099 W/% followed by 10 h at -0.0071 W/% and 5 h with -0.0018 W/%.

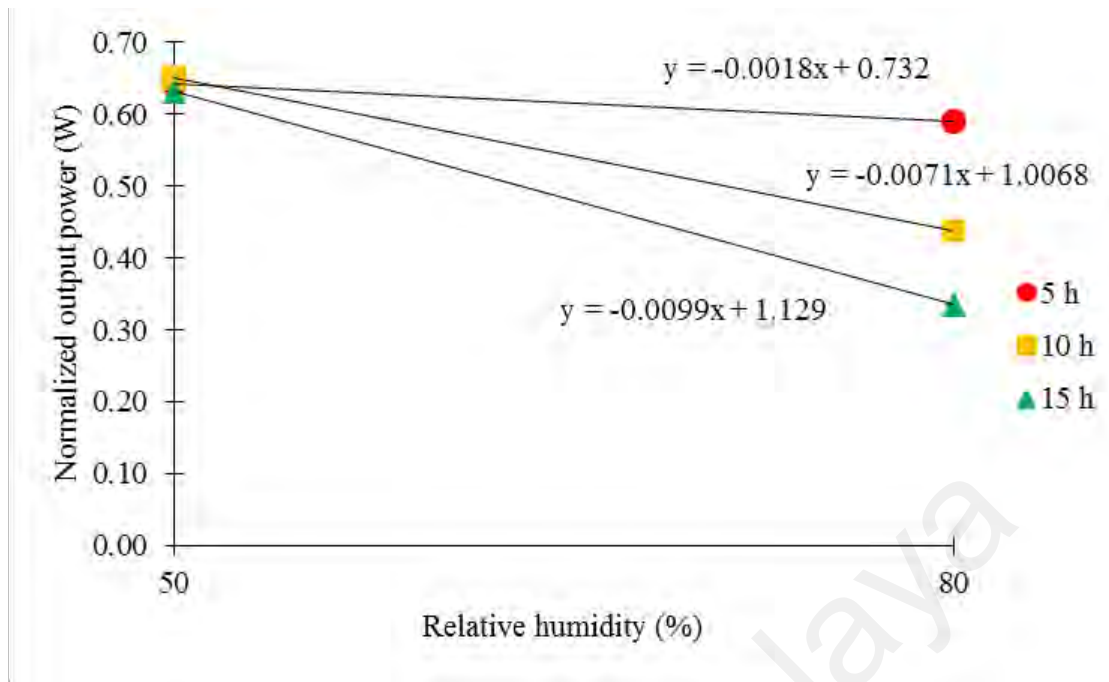


Figure 4.17 Humidity sensing response of fabricated samples for humidity concentration between 50% and 80% of RH.

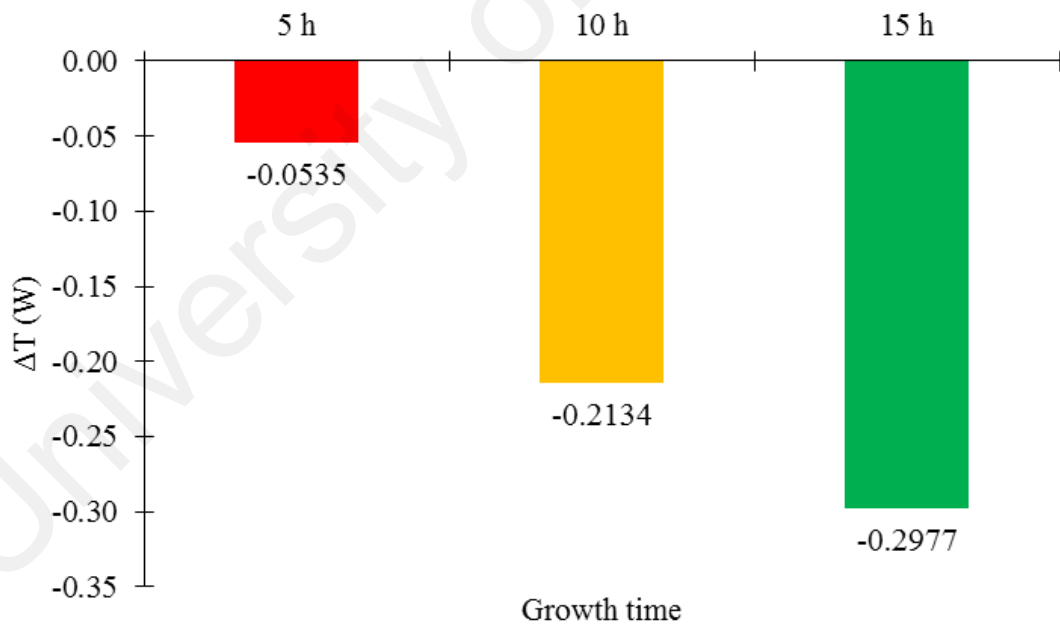


Figure 4.18 Transmittance reduction of fabricated samples measured at 80% of RH.

The values of normalized length (Z) and normalized scattering coefficient (ζ) from the new fabricated samples from humidity characterization were analyzed and correlated to the theoretical model as shown in Figure 4.19. It was found that all three samples were having the value of Z closer to each other where they were fallen in between 0.42 and 0.46. However, the values of ζ were found to be dominant on the sample of 15 h which has the value of 0.4185. The values are subsequently higher for 10 h and 5 h with 0.5193 and 0.8356 respectively. The smaller the number of ζ shows that higher scattering amount by ZnO nanorods at maximum tested humidity level. Therefore, this justifies the sample with 15 h growth time has the highest sensing response compared to the others. It was also observed that the operating state of this sample lied closed to the optimum working condition line as presented in the theoretical model.

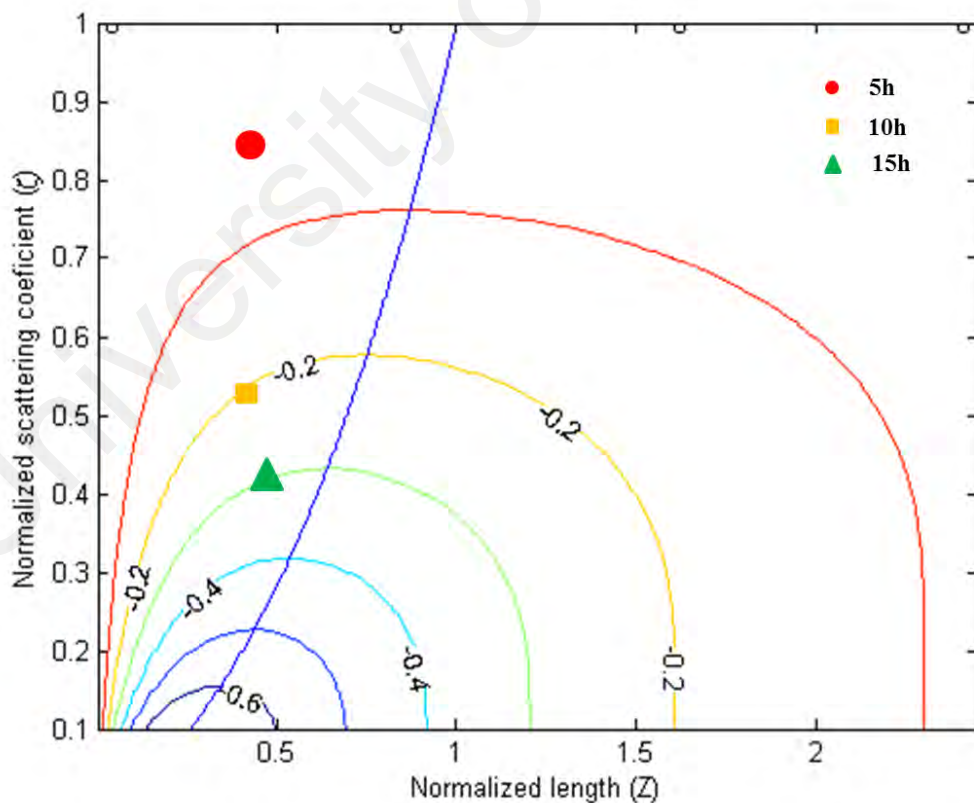


Figure 4.19 Correlation between the fabricated samples with theoretical approach for humidity characterization.

Since the sample with 15 h growth time exhibited the highest sensing response among all, this sample will be used for the integration of ZnO based humidity sensing device in the next chapter. Prior to the integration work, the sample was first characterized by the same SEM machine operating at 20 kV. Figure 4.20 shows the SEM images of the ZnO coating, whereby hexagonal wurtzite ZnO nanorods growth can be observed. Figure 4.20(a) shows the top view of nanorods and average diameter of the nanorods was found to be ~ 78 nm. Figure 4.20(b) shows the cross-sectional SEM image of the ZnO nanorods, showing the preferential growth of ~ 2.32 μm long nanorods on the substrate.

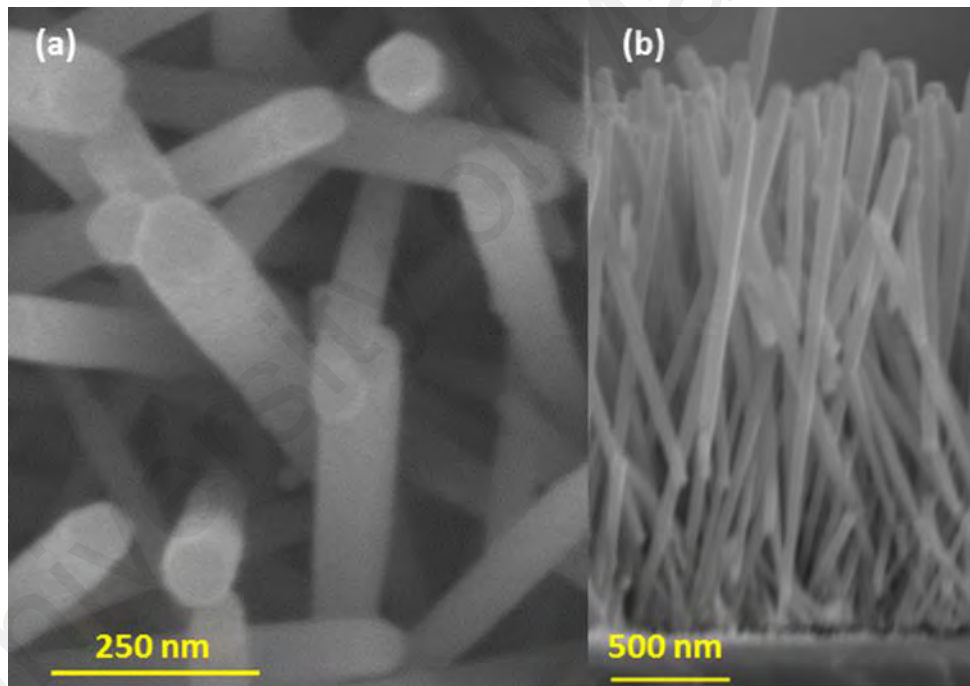


Figure 4.20 SEM micrographs of (a) top and (b) cross sectional of ZnO nanorods grown on glass substrate.

4.5 Summary

The present study demonstrated the maximization of dynamic range for ZnO nanorods coated on glass substrate for humidity sensing application with controlled growth duration and length of ZnO coating. The study was performed theoretically and correlated with experimental approach to identify the optimum operating condition for the fabricated sensing device to work at the best sensing performance. The experimental results were matched reasonably well to the first order approximation model. The investigation revealed that the best sensing performance of any fabricated sensing device can be accomplished by achieving the optimum operating condition, independent of ZnO nanorods growth parameters or coating area.

The final samples for the development of an integrated ZnO based humidity sensing device were successfully fabricated. The samples were characterized with humidity sensing and analyzed towards theoretical model. It was observed that the sample with 15 h growth time produced the highest sensing response. According to theoretical dynamic range model, the 15 h sample was lying nearly to the optimum operating condition region which makes the device performed better than the others. Therefore, the sample was used for the integration of ZnO based humidity sensing device which presented in the subsequent chapter.

CHAPTER 5: ZINC OXIDE NANORODS COATED GLASS SUBSTRATE BASED SENSING DEVICE

5.1 Introduction

Over the years photonics has been almost an ideal technological platform in the development of high-performance sensors for both physical and chemical quantities (Perrone, 2018). Optical based sensing system possesses exceptional merits over electrical transducers for example insusceptible to electromagnetic disturbance (B. Lee, 2003), withstand to chemical erosion (Giallorenzi *et al.*, 1982) and waterproof capability (Saito *et al.*, 1987). Optical sensor has been widely used in various areas especially in people's daily life safety applications. Environmental condition monitoring (Choudhury, 1998) system such as humidity (Ascorbe *et al.*, 2017), temperature (Leal-Junior *et al.*, 2018), chemical vapors (acetone, ethanol and methanol) (Mulyanti *et al.*, 2017) or gas (Bogue, 2015) is essential to assure the health of human is not at risk. Besides that, it is also important in order to maintain an optimum comfortable working environment for workers (Shaharon *et al.*, 2012).

Although optical based sensors offer numerous advantages over electrical based sensor device, they are usually associated with high cost, complexity in operation and requires high operational power (Rafis *et al.*, 2017). The employment of advance optical equipment in the sensing setup such as laser source, optical power meter, spectrum analyzer as well as mechanical precision apparatus raised the total development and operational cost of the sensing system. This restricts wide application of optical sensor and it is not cost-effective for commercialization. Therefore, the simplicity in operation and the cost of the sensor development must be taken into serious consideration when designing a sensor device.

In this chapter, the fabrication and integration of a simple humidity sensor that employs ZnO nanorods as the sensing element in Arduino platform is presented. The complete sensor device is composed of a commercial light-emitting diode (LED), ZnO nanorods coated glass substrate as the sensing element, and a photodiode to detect the scattered light from the nanorods. The usage of Arduino platform for signal processing and calibration is introduced. Utilizing intensity-modulated/direct-detection (IM/DD) based sensing, the sensor device is experimentally demonstrated towards humidity and formaldehyde vapor concentrations.

5.2 Integration of Zinc Oxide Based Sensor Device

Several steps were involved in process of developing an integrated ZnO based sensing device as illustrated in Figure 5.1. Considering the fabrication of glass substrate coated with ZnO nanorods was done in previous work, the integration process started with the design and fabrication of the sensor body. The sensor body is used to precisely position the basic sensor components such as fabricated glass substrate, light source and detector. In the second step, all these components were assembled on the fabricated sensor body. The subsequent process was the development of the receiver circuit. In this process, electronic components such as operational amplifier, resistors, and capacitor were involved in order to acquire a suitable voltage level for the sensing system. The sensor system was then combined by integrating the completed sensor body and receiver circuit becoming one compact sensing device. In the final step, the integrated sensing device was characterized against humidity and formaldehyde vapor to validate the performance of the sensor device.

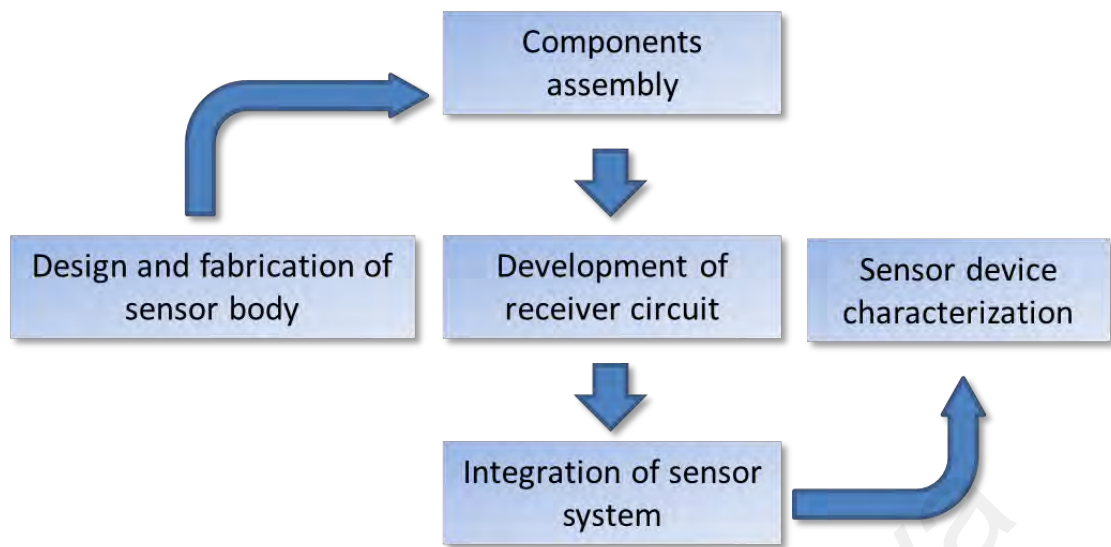


Figure 5.1 Development process of integrated sensing device.

5.2.1 Design of Sensor Assembly

In order to realize a cost-effective humidity sensor device, a commercial green LED with a central wavelength of 517.5 nm (bandwidth: 5 nm) was utilized as light source and a photodiode with model number of SFH203P (OSRAM, 2015) was used as light detector. A 3D printer was used to fabricate the body of the sensor device. The sensor body design was modeled using 123D Design software (Autodesk). Polylactic acid (PLA) filament was used as 3D printing material. The fabrication of the sensor device body was optimized to achieve precise position of the sensing material (sample coated with ZnO nanorods), the LED and the photodiode. The sensor body was divided into three sections, namely LED holder, sample holder and photodiode holder. As shown in Figure 5.2, the horizontal surface was fabricated with a dimension of 25 mm × 15 mm to accommodate the coated sample. The holder for the LED with diameter of 5 mm and length of 9 mm was placed at one end of the sample, while at the other end the holder for the photodiode with diameter of 5 mm and length of 5 mm was located. The position of the LED was set as close as possible to the edge of the glass substrate with a

small aperture window of 1 mm (diameter) while the photodiode with the same aperture setup was placed at the edge opposite the LED. The LED was set at an incident angle of 50° yielding the refraction angle of the light in the glass to be $\sim 30^\circ$. In this condition, according to Snell's Law, the incident angle for the light at the glass-air interface is approximately 60° , achieving total internal reflection for the light propagating through the glass limiting the light intensity losses solely to scattering from the sensing material (ZnO nanorods). A printed circuit board (PCB) of a receiver circuit for the sensing system was proposed to be integrated underneath the sensor body to realize a compact sensing system.

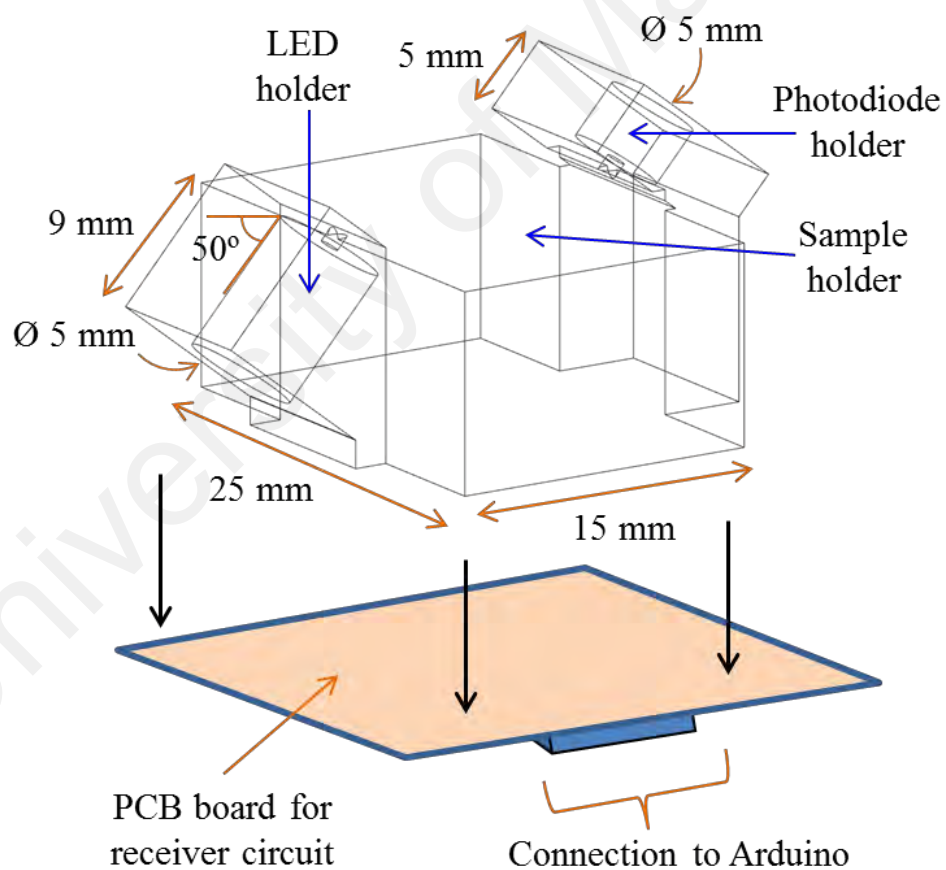


Figure 5.2 Schematic representation of integration of the optical sensor board (Orthographic view of the sensor body model).

Figure 5.3 shows the successful fabricated sensor body via 3D printing. The sensor body was printed with black color PLA filament in order to eliminate stray light being reflected back into the sensing system. The view of front, top and side of the sensor body were shown in Figure 5.3(a), Figure 5.3(b) and Figure 5.3(c), correspondingly. On the side view image of the sensor body, the aperture window of 1 mm in diameter for the LED and photodiode were successfully created for light excitation from LED to the edge of the glass towards the photodiode.

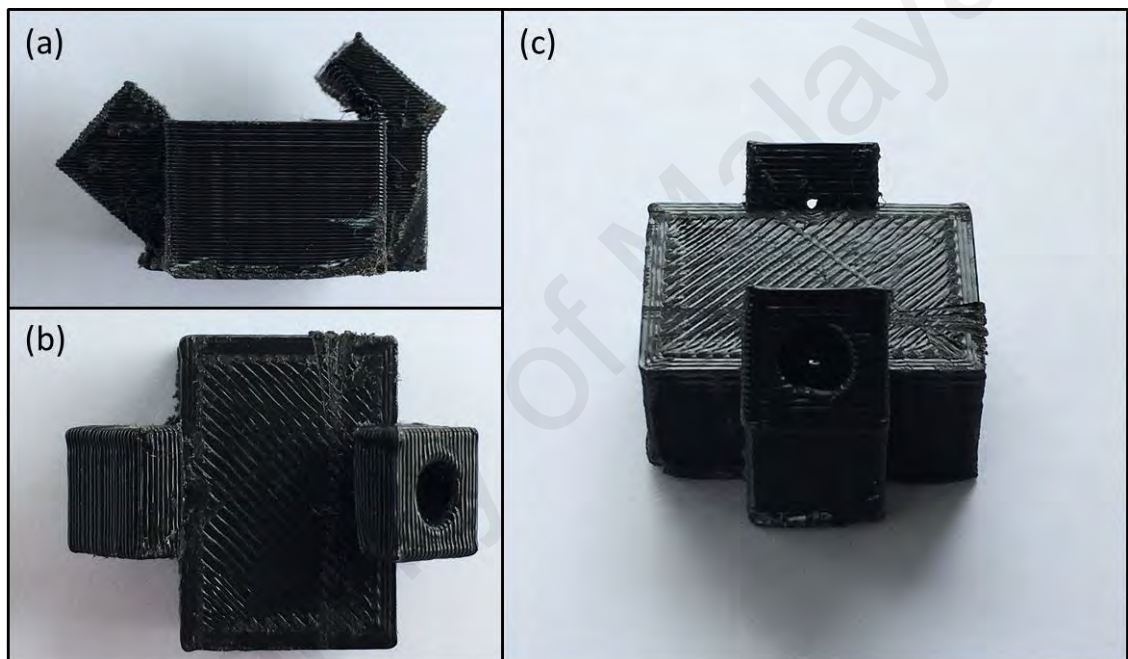


Figure 5.3 The (a) front, (b) top and (c) side view of the fabricated sensor body via 3D printing.

In addition to the sensor body, two covers were fabricated by using the same 3D printer. These covers were used to conceal both end of LED and photodiode to block the light transmitted by the body of the LED or ambient light from entering the photodiode. This is to ensure a stability of the sensor device when measuring humidity in a standard environment condition. The design of the cover for the LED and photodiode is shown in Figure 5.4. Each cover was fabricated with the dimension of 10 mm in diameter and 3

mm of height. The inner part of the cover has a cylindrical hollow with the diameter and height of 7 mm and 1.5 mm correspondingly. This small hollow was meant to fit the base of both LED and photodiode. At the bottom surface of the cover, a rectangular shaped of hole with the dimension of 5 mm x 1 mm x 1.5 mm was fabricated to fit the terminal pins for both LED and photodiode. Figure 5.5 depicted the successful fabricated cover.

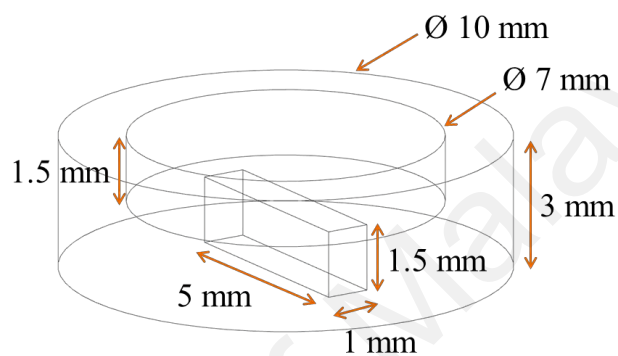


Figure 5.4 Schematic representation of the LED/photodiode cover dimension.



Figure 5.5 Fabricated cover for LED/photodiode.

5.2.2 Receiver Circuit of Sensor System

In the proposed sensing system, the green LED used as light source has minimum forward voltage (V_{fmax}) and maximum forward current (I_{fmax}) of 3.2 V and 20 mA, respectively. With the +5 VDC supply (V_s) from Arduino board, a resistor (R_s) of 100 Ω is connected in series with the LED in order to limit the current to the safe level for driving the LED. This is to protect the LED from burning. The value of I_{fmax} was obtained at 18 mA as calculated by Equation (5.1).

$$I_{fmax} = \frac{V_s - V_{fmax}}{R_s} \quad (5.1)$$

During the operation of the sensor device, light travels through the sample and ZnO nanorods coated region. At the output, light is collected and converted by the photodiode to a linearly proportional current. Due to the use of a small aperture to block the stray light, the intensity of light captured by the photodiode is very low. Therefore, a simple transimpedance amplifier (TIA) was used to convert the output current of the photodiode into a suitable processing voltage for the Arduino based sensing system (Sterckx, 2015). Figure 5.6 shows the schematic diagram of the receiver circuit, which employs a LT1884 op-amp chip (LinearTechnology, 2000) which is dual rail-to-rail output device with pico-amp input precision. The output voltage of the op-amp can be expressed as

$$V_{out} = R_f \times I_d \quad (5.2)$$

where R_f and I_d are the feedback resistor and photocurrent, respectively. Note that a feedback capacitor, C_f is included for stability purposes (Sterckx, 2015). This capacitor has no influence on the measurement, since at low frequencies (changes in humidity are very low frequencies), almost the entire I_d flows through R_f . The output of the Op-Amp chip can yield at least 4.7 V when loads are no more than 1 mA (LinearTechnology, 2000). As it is impossible to measure the small photocurrent with a regular multimeter,

R_f was varied in reality to obtain a suitable output voltage level for the sensor system. The feedback resistor used in the circuit is set to $7.8\text{ M}\Omega$ in order to obtain an output of 1.9 V at 50% of the RH level (room condition). The inputs of the Op-Amp should be field effect transistors in order to operate like an ideal Op-Amp. The resistance of bipolar junction transistor inputs would be too low in comparison to an R_f of $\text{M}\Omega$ proportions. The nominal voltage level of 1.9 V (with tolerances for both upper and lower side of the range) at ambient conditions was sufficient for humidity sensing since the output voltage is expected to decrease as the humidity increases, due to the increase of the refractive index of surrounding of the ZnO nanorods. The selected Op-Amp chip has several advantages such as high input impedance compared to R_f , and the ability to operate with the voltage supply that is available in the Arduino board. In this system, Arduino Uno R3 board is used to provide the supply voltage for the receiver circuit (+5 VDC). The output voltage from the receiver circuit is sent to Arduino for signal processing before it being transferred to computer for recording and display.

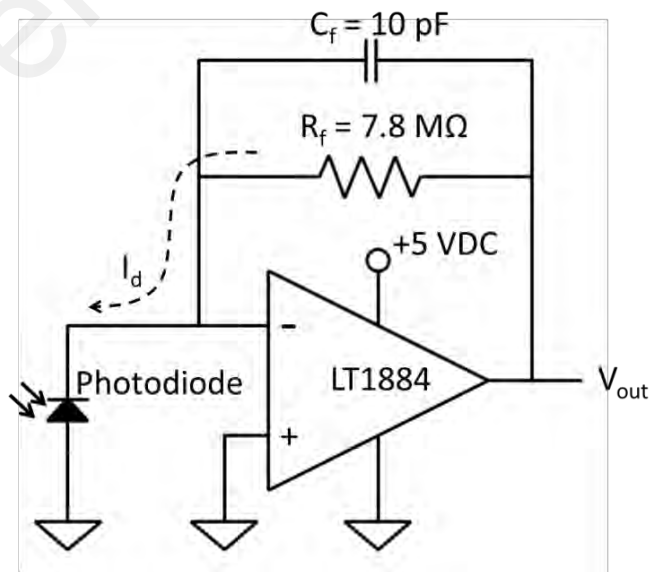


Figure 5.6 Schematic diagram of transimpedance amplifier (TIA).

5.2.3 Device Assembly

The complete integrated ZnO based sensor device is shown in Figure 5.7. The overall dimensions of this sensor device are 45 mm (L) × 25 mm (W) × 40 mm (H) as shown in Figure 5.7(a). Figure 5.7(b) depicts the top view of the sensor device where the sample coated with ZnO nanorods was placed on the horizontal surface and fixed by glue. The LED was mounted inside the LED holder and placed as close as possible to the edge of the sample, while the photodiode was mounted inside its holder, opposite to the LED. It is shown that light from the green LED was directed through a small aperture window placed directly in front of the LED. As light travels inside the glass substrate, it interacts with the ZnO nanorods as the sensing element at the glass-ZnO coating interface before reaching the photodiode which is placed at the other end of the glass substrate. A simple transimpedance amplifier circuit with LT1884 chip was placed underneath the sensor body which served to convert the photocurrent of the photodiode to an appropriate voltage level that could be processed by Arduino board as illustrated in Figure 5.7(c).

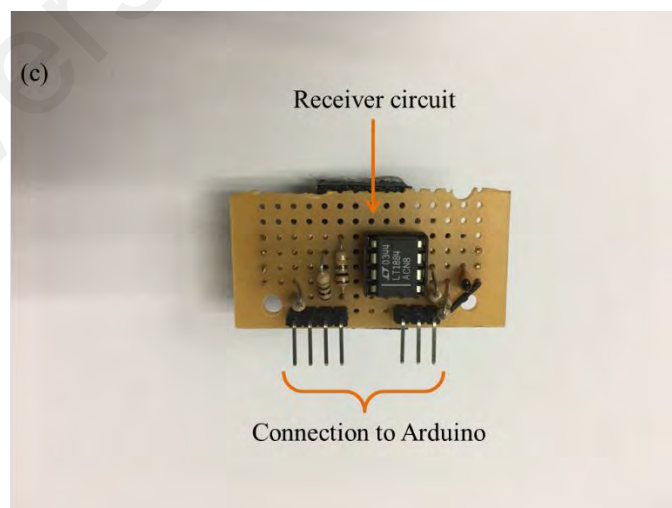
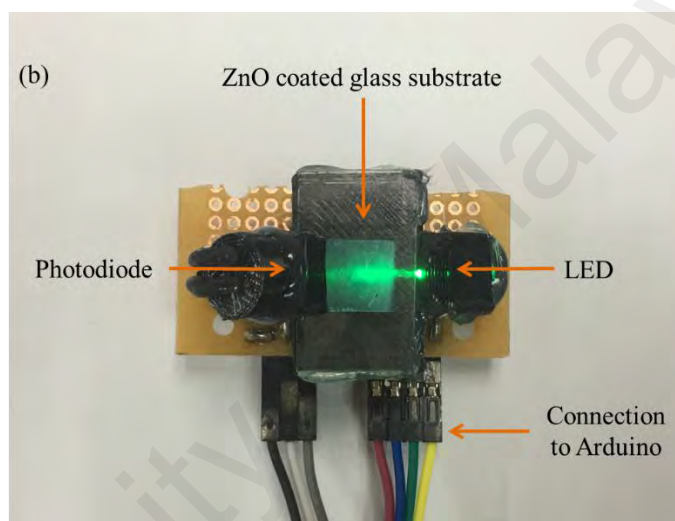
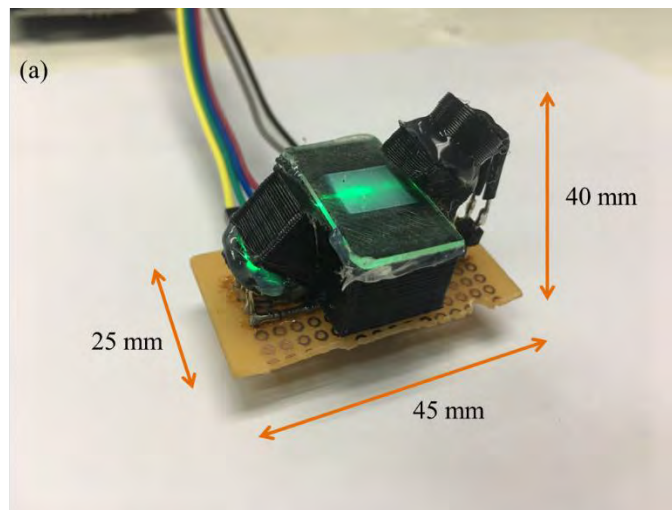


Figure 5.7 (a) Orthographic view, (b) top view, and (c) bottom view of the fabricated humidity sensor device integrated with op-amp circuit.

5.2.4 Receiver Circuit to Arduino Controller Board Interface

Figure 5.8 shows the interface wiring diagram for the connection of the receiver circuit and Arduino controller board. All electronic components on the PCB board of the receiver circuit were powered by the Arduino platform. This eliminates the necessary of having additional voltage power supply circuit for these components thus simplify the sensor device system. The LED was powered from the digital pin D13 and GND. The digital pin was configured in HIGH state which produced an amount of +5 V when it turned ON and will be at 0 V when it is in OFF condition. On the receiver circuit, the amplifier was powered by +5 V supply and GND from the Arduino platform which connected to the V+ and V- of the amplifier chip, respectively. The amplifier has capability to operate with single power supply, thus it can use GND terminal instead of negative voltage supply. The amplified output signal from the amplifier was connected to the analog pin A0 which is used to read the analog voltage from the amplifier. The analog voltage was then processed and converted by the built-in analog-to-digital converter (ADC) of the Arduino into digital form that can be read by a computer. The Arduino board was connected to a computer via USB cable for voltage supply to the Arduino board and data recording as well as display.

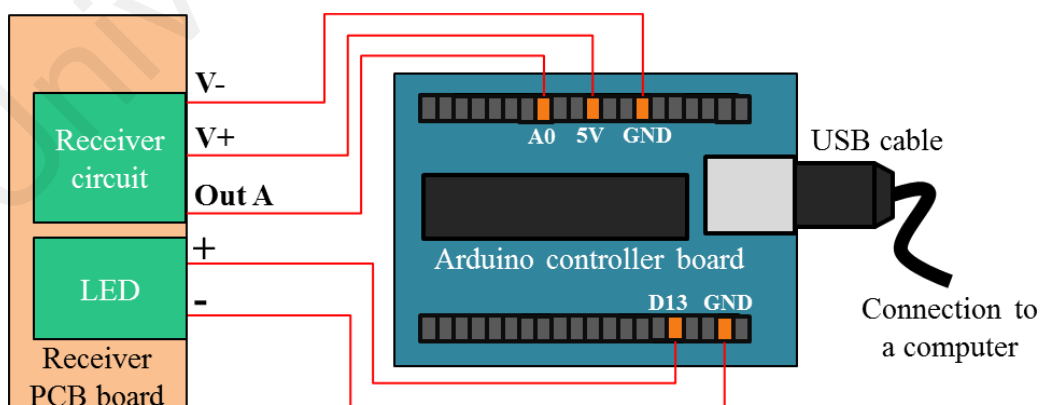


Figure 5.8 Wiring diagram for the connection between receiver circuit and Arduino platform.

5.3 Humidity Sensing Experiment

Figure 5.9 illustrates the experimental setup used for humidity measurement with the fabricated sensor device. A humidity sensing chamber (0.23 m × 0.18 m × 0.15 m) was used for all the experiments. The fabricated sensor device was placed inside the chamber and connected to Arduino platform coupled to a computer for data collection. A hygrometer was mounted on the chamber wall throughout the experiment to serve as a reference for the actual RH level inside the chamber. Figure 5.10 shows the actual images of humidity experiment performed on the sensor device. The front and top view of the experiment setup are shown in Figure 5.10(a) and Figure 5.10(b) respectively. In this experiment, the fabricated sensor device was tested with the RH level ranging from 35% to 90%. This range was chosen based on literature reports about the humidity level of the indoor air environment which, normally, should be within the range of 40% - 70% in order to minimize the spread of viruses and bacteria (Alsmo *et al.*, 2014). This range complied with the acceptance range according to Malaysia Industry Code of Practice on Indoor Air Quality (2010) (Arifin *et al.*, 2015). Shaharon and Jalaludin suggested the RH level should be maintained in between 40% and 60% for the optimum comfortable working environment (Shaharon *et al.*, 2012). Therefore, the lower threshold of the RH level was tested at 35%. A measurement range of up to 90% RH is suitable to monitor the air condition in order to prevent possible corrosion of electronic components that could be a fire hazard for enclosed environments (Jali *et al.*, 2019). In order to cover the lowest achievable RH level in the measurement, silica gel was used to lower the RH level inside the chamber to ~35% before it was replaced with wet tissue to raise the RH level to 90% of RH level at a constant temperature of 25 °C. The measurement was recorded at every 5% of RH level and repeated several times for reliability performance analysis.

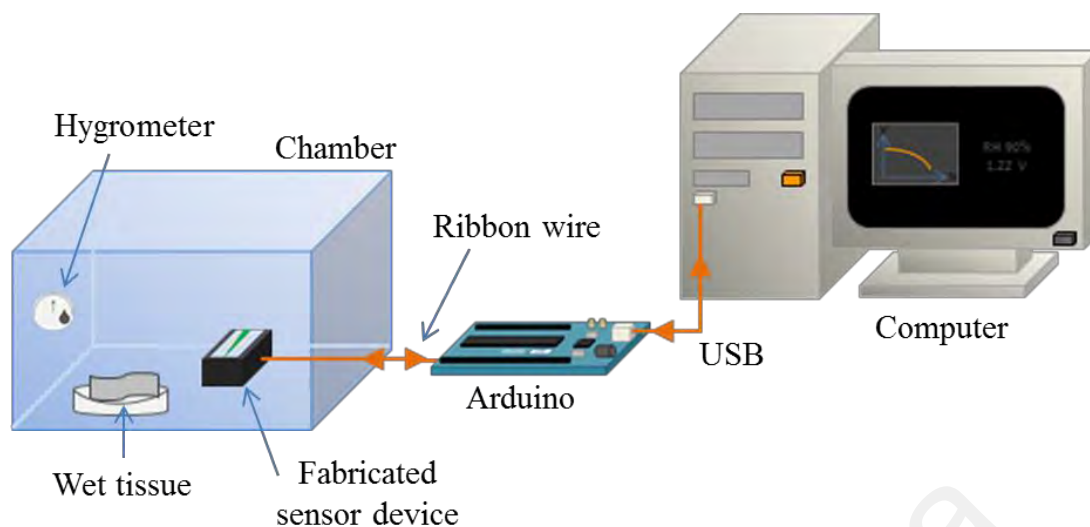


Figure 5.9 Schematic representation of the experimental setup used for humidity sensing.

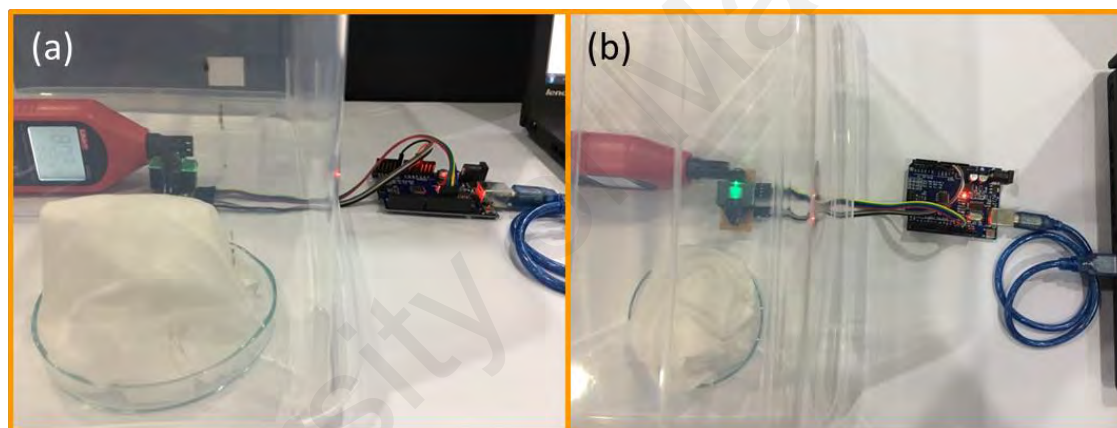


Figure 5.10 The image of (a) front and (b) top view of the actual of humidity experiment conducted with integrated sensor device.

Table 5.1 shows the output voltage of the sensor system read by the Arduino platform at every 5% change in RH level, from 35% to 90% RH. The output voltage value shown in the table is in average value as the measurement was repeated for several times. The sensor device responded well to the changes of humidity whereby the output voltage decreases as the humidity increases. It was found that reduction of the voltage was small for lower RH levels (35% to 70%) and rapid changes were observed when the RH was increased beyond 70%. Overall, a non-linear trend emerged, that

could be fitted to a second order polynomial curve with 98.56% accuracy as shown in Figure 5.11.

Table 5.1 The output voltage read by Arduino platform.

Relative humidity (%)	Output voltage (V)	ΔV (V)
35	1.97	0
40	1.95	-0.02
45	1.93	-0.04
50	1.91	-0.06
55	1.88	-0.09
60	1.83	-0.14
65	1.78	-0.19
70	1.73	-0.24
75	1.65	-0.32
80	1.56	-0.41
85	1.44	-0.53
90	1.22	-0.75

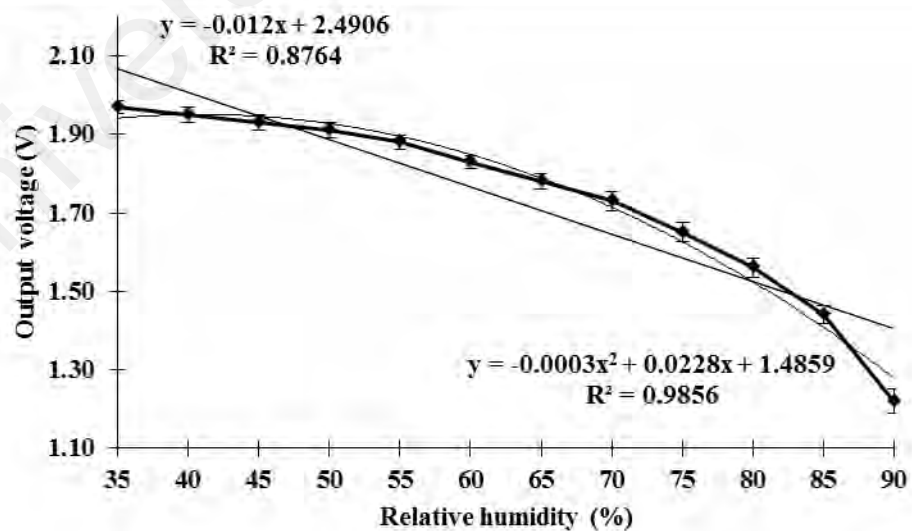
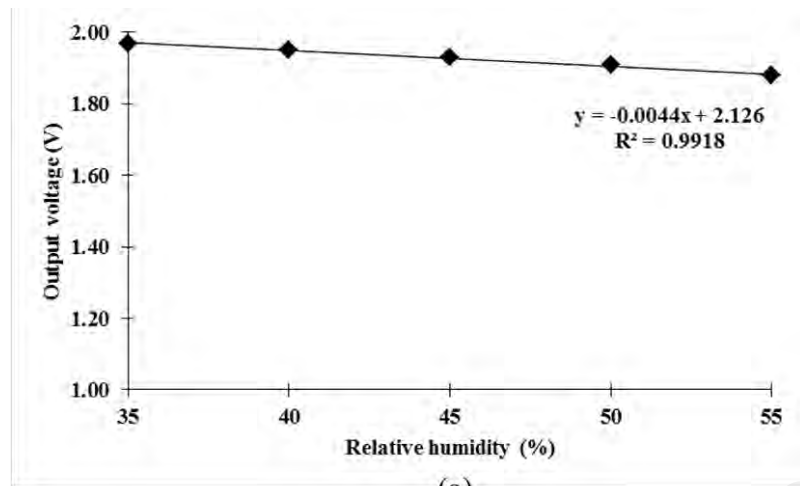
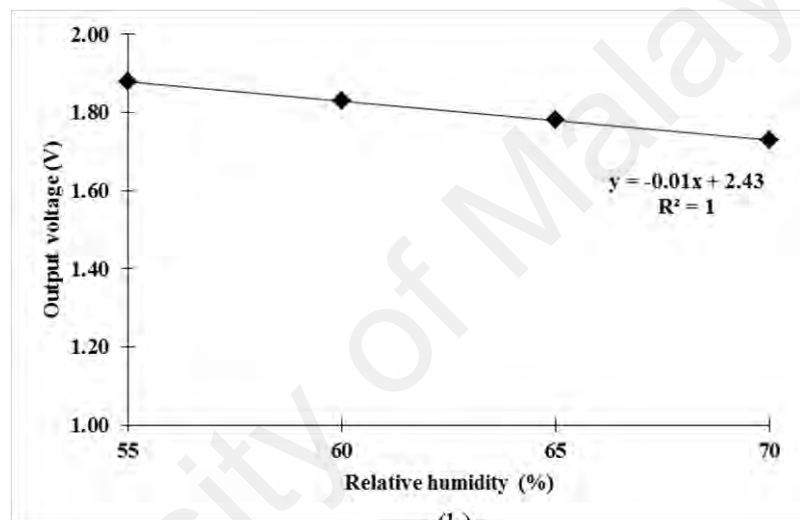


Figure 5.11 Humidity sensing performance of a typical sensor device.

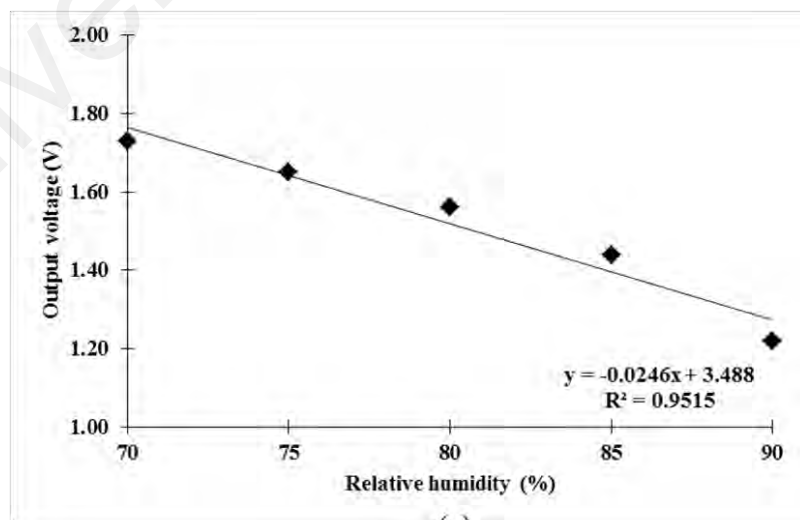
The sensitivity of the fabricated sensor device can be distinctly separated into three regions as shown in Figure 5.12. The sensitivity for the RH from 35% to 55% was -4.4 mV/%, while the sensitivity increased to -10 mV/% for RH between 55% and 70% as depicted in Figure 5.12(a) and Figure 5.12(b) respectively. At RH levels between 70% and 90%, sensitivity improved by almost 2.5 times and was found to be -24.6 mV/% as shown in Figure 5.12(c). The linear regression line was obtained from the software and the average sensitivity of the fabricated sensor device was found to be -12 mV/% for 35% to 90% RH levels. The total voltage drop was recorded to be ~750 mV throughout the tested RH measurement. These voltage variations were the result of changes in the intensity of the light captured by the photodiode which, in turn, were due to the changes of the RH level surrounding the sensor device.



(a)



(b)

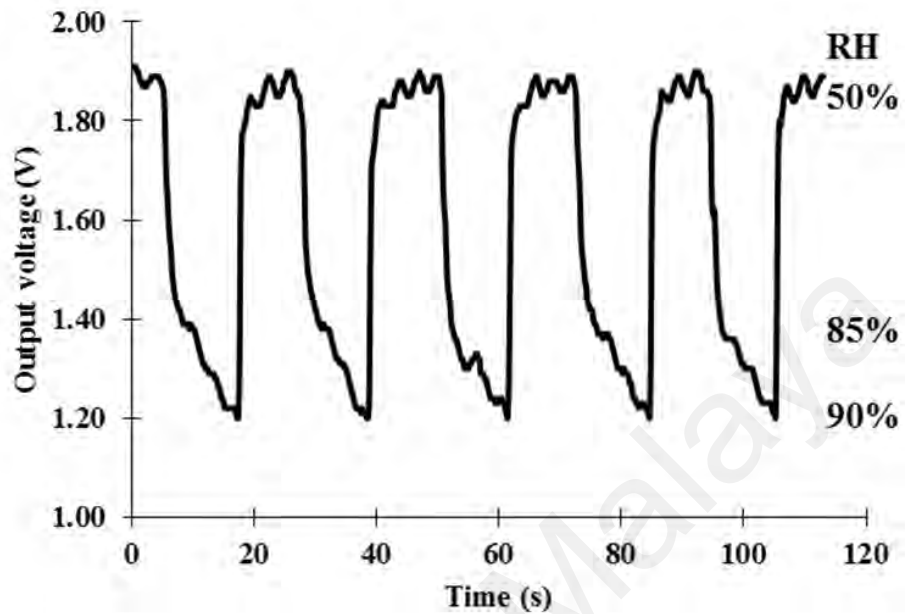


(c)

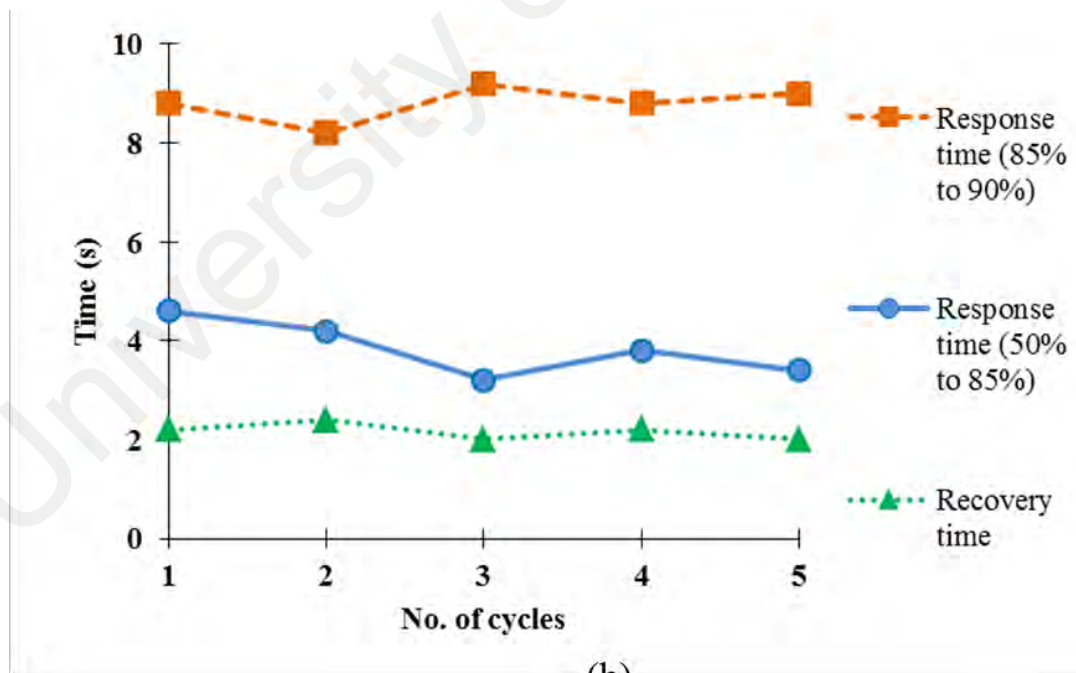
Figure 5.12 Three region of sensitivity of the sensor device. (a) 35% to 55% of RH, (b) 55% to 70% of RH and (c) 70% to 90% of RH.

Figure 5.13 shows the performance analysis of a typical sensor, including the response and recovery time for various measurement cycles. The sensor device was repeatedly moved in and out of the humidity chamber maintained at 90% of RH level with respect to the ambient level (RH ~50%). As shown in Figure 5.13(a), the fabricated sensor device responded well in terms of repeatability performance. The output voltage consistently decreased and increased back to normal condition as the sensor was exposed to humidity concentrations over several cycles. There were some fluctuations in the output voltage observed at 50% of RH level as well as when the RH increased from 85% to 90%, which is similar to the other sensors reported in the literature (Aneesh *et al.*, 2011; Azad *et al.*, 2017; Xuan *et al.*, 2014). The sensing mechanism in our system is based on the adsorption and desorption process on the surfaces of ZnO nanorods (Kim *et al.*, 2005), which leads to a change of forward scattering that is linked to the total transmission loss. The variation of humidity levels during the operation of the device at 50% RH and 90% RH led to the observed fluctuations in the output voltage prior to reaching stability. Under more careful conditioning of the humidity levels in the test chamber the fluctuation of the output voltage can be removed. In this analysis, the response time and recovery time of the sensor were observed to indicate the sensing performance of a sensor. Figure 5.13(a) further shows that the sensor response was fast for humidity levels from 50% to 85% but slowed down at very high humidity levels (85% to 90% RH). It was found that the average response time to sense the humidity level from 50% to 85% was 3.8 s while the time taken for the response from 85% to 90% was 8.8 s as shown in Figure 5.13(b). As for recovery time, the sensor has very good recovery time, whereby an average recovery time of 2.2 s was observed. In summary, the fabricated sensor exhibited stable sensing performance with reliable and repeatable signal levels and better response/recovery time compared to previous

works on ZnO based sensors as summarized in Table 5.2. This shows that the proposed sensor device is suitable to be used in real time humidity monitoring.



(a)



(b)

Figure 5.13 Sensor performance analysis. (a) Sensor repeatability at 90% of RH level with respect to room level (50%) and (b) sensor response time and recovery time of the sensor device.

Table 5.2 Performance comparison of humidity sensor with previous works.

Sensing Material	Synthesis Method	Measurement Range (RH)	Response Time	Recovery Time	Reference
ZnO	Hydro-thermal	35% - 90%	3.8 s (85% RH)	2.2 s	This work
Polyaniline-ZnO	Chemical polymerization	20% - 90%	36 s (80% RH)	48 s	(Shukla <i>et al.</i> , 2015)
ZnO	Sol-Gel	10% - 95%	120 s (95% RH)	195 s	(Yadav <i>et al.</i> , 2009)
ZnO	Screen printing	5% - 90%	92 s (90% RH)	-	(Dixit <i>et al.</i> , 2007)

5.4 Formaldehyde Vapor Sensing

Formaldehyde is considerably dangerous volatile organic compounds (VOCs) when being exposed to human at concentrations beyond specific level (Leidinger *et al.*, 2014). Therefore, early detection of this colorless toxic gas is essential in order to minimize the risk or threat to human's life. In this work, the developed sensor device which was previously tested against humidity was also validated in detecting formalin vapor concentrations.

5.4.1 Preparation of Formalin Solution

Formalin is an aqueous solution of formaldehyde. For this experiment, the solution was prepared via dilution process of formaldehyde and DI water. The concentrations of the formalin were varied by using dilution formula expressed as

$$M_1V_1 = M_2V_2 \quad (5.3)$$

where M_1 is the concentration in molarity of the concentrated solution, V_1 is the volume of the concentrated solution, M_2 is the concentration in molarity of the dilute solution and V_2 is the volume of the dilute solution. The concentrations of formalin were varied from 1% to 5% and every concentration of formalin has similar volume to maintain the respective concentration during the measurement.

5.4.2 Formaldehyde Vapor Experiment

An identical chamber setup as previous humidity experiment was used in this experiment except the wet tissue which was replaced with a petri dish for placing formalin solution inside the chamber as shown in Figure 5.14. A desired amount of formalin was poured into a petri dish and placed inside the chamber. The experiment was conducted in room conditions (temperature of 25 °C and relative humidity of 60%) to replicate the domestic user environment when handling the substance. Upon closure of the chamber lid, few moments were given to let the solution to naturally evaporate at room temperature through the volume of the chamber while the humidity level of the chamber was monitored. The humidity level of the chamber was increased due to the presence of water from the solution. The output voltage reading from photodiode was recorded at 80%, 85% and 90% of relative humidity (RH). The experiment was repeated for different concentrations of formalin varied from 1% to 5% and the results were analyzed with referenced to 0% (pure water).

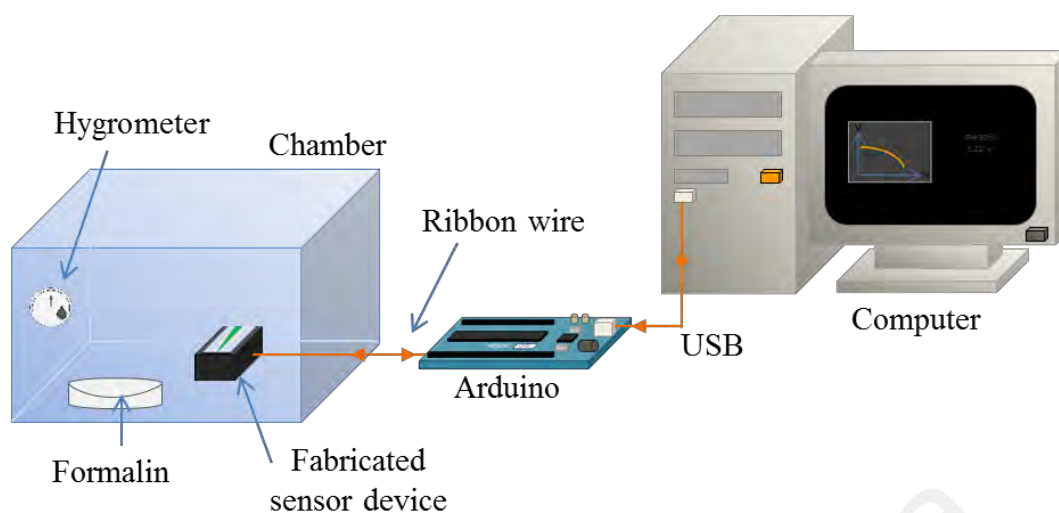


Figure 5.14 Schematic representation of the experimental setup used for formaldehyde vapor sensing.

The response of the fabricated sensor towards formaldehyde vapor concentrations by light scattering effect of ZnO nanorods is shown in Figure 5.15. The graph shows the measurement at three different RH levels (80%, 85% and 90%) inside the chamber. In this graph, the output voltage was normalized towards 1 V for relative humidity at 60% (room condition). It was found that at 80% of RH level the detection of formaldehyde vapor was not significant between the concentrations. The measurement at 85% of RH shows that the sensor starts to respond towards the detection of formaldehyde vapor concentrations. It can be seen that a larger response is observed on measurement at 85% of RH compared to 80% for the concentration from 0% to 5%. At 90% of RH, the response of the fabricated sensor shows significant output voltage differences at every 1% incremental of formaldehyde concentrations. This can be shown by the bar chart as shown in Figure 5.16. It is notable that the reduction of the output voltage (ΔV) at 90% of RH shows consistent incremental output voltage reduction across the concentrations of formaldehyde vapor as compared to the 80% and 85%.

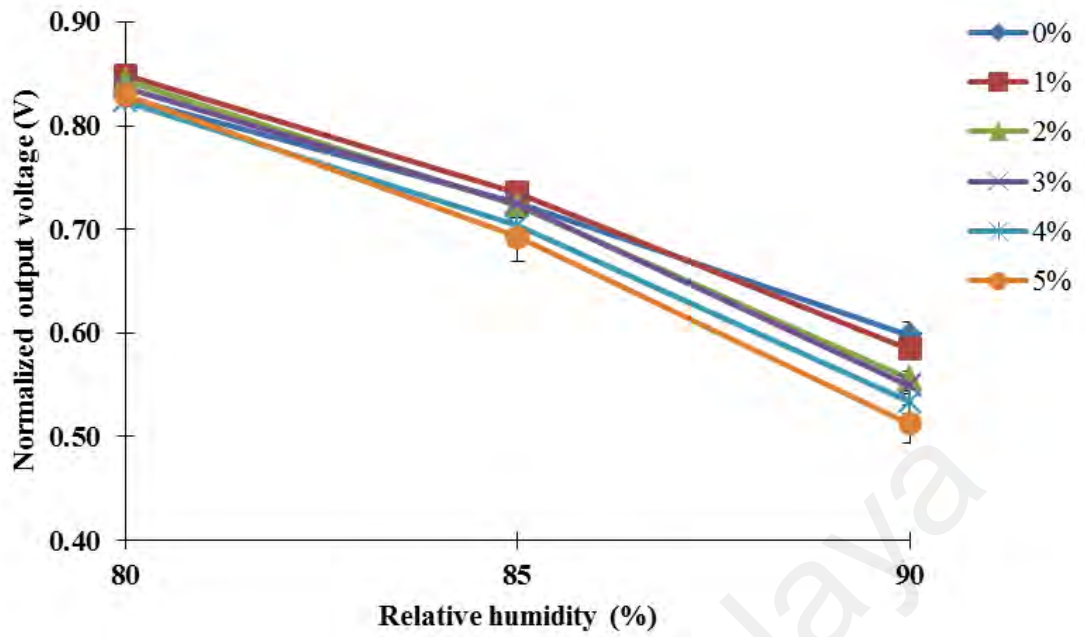


Figure 5.15 Formaldehyde vapor sensing at different RH level.

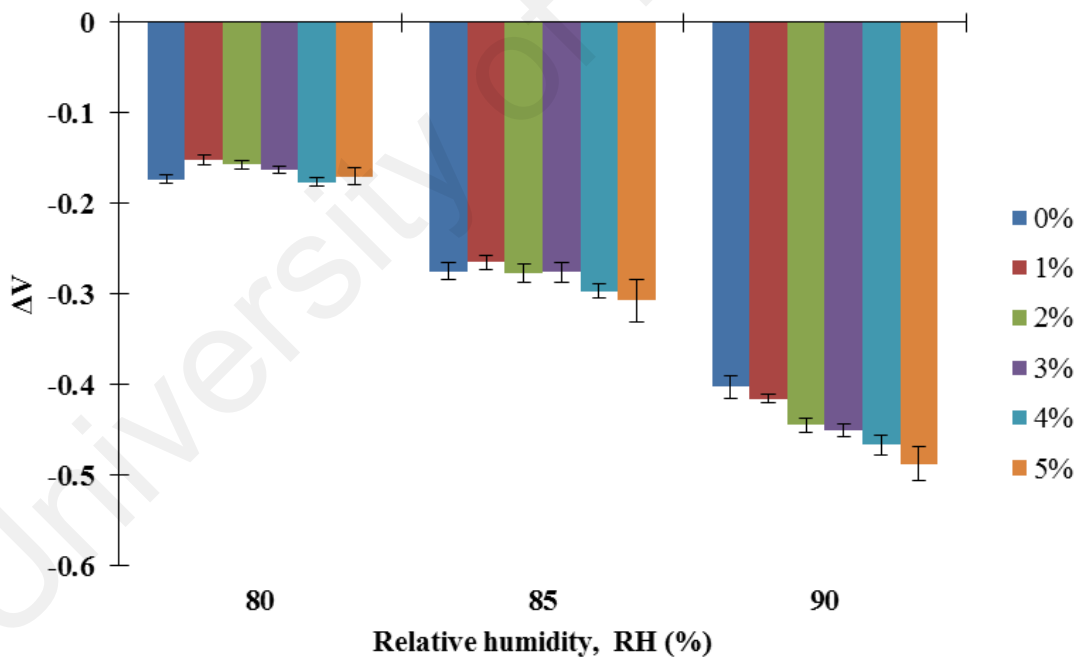


Figure 5.16 Reduction of output voltage for the fabricated sensor in response to the vapor concentrations.

It was observed that the formaldehyde vapor was not fully evaporated at 80% and 85% of RH level and needs longer time to spread to all over the volume of the chamber for the sensor to response to the changes at low concentrations. This proved by the sensor stability performance as shown in Figure 5.17. In this analysis, the measurement at 90% of RH level was prolonged for 600 s to investigate the stability of sensor response. The existence of water in formalin causes the humidity in the chamber to continue increased. However, the incremental of the RH level was getting slower as it almost reached the saturation level in the chamber. Therefore, during the stability measurement, it was recorded that the RH level only increased from 90% to 92% within 600 s. From the graph, it shows that the measurements were relatively consistent between the concentrations throughout duration. Although there was slight incremental of humidity level, the sensor responded well to the changes and showed relative response between the concentrations of the vapor. This shows that relative humidity is not a critical factor in the measurement of formaldehyde vapor concentrations when the vapor was fully and uniformly spread throughout the volume of the chamber. The result in Figure 5.17 further shows that the fabricated sensor has good stability in measuring as low as 1% of vapor concentrations.

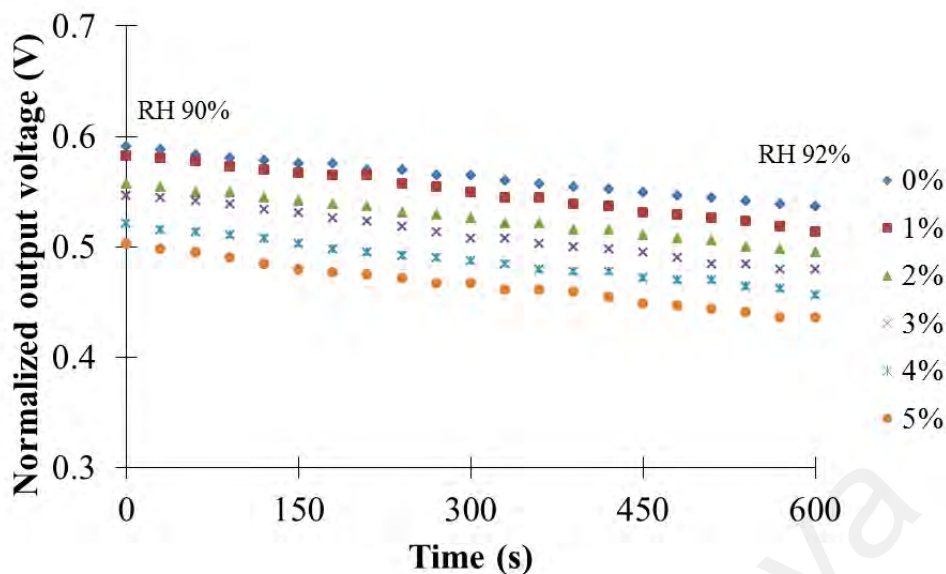


Figure 5.17 The stability analysis of the fabricated sensor.

The reduction in output voltage upon exposure to the formaldehyde vapor was due to reduction of light intensity measured at the photodiode. As discussed earlier in the humidity sensing study, the leakage of light was observed due to the adsorption process of substance onto ZnO nanorod surface which alter its electrical properties as well as the refractive index of the nanorods surroundings. Thus, reduction of output intensity was observed during characterization with humidity concentrations. In the event of detecting formaldehyde vapor, it was found that the output intensity was further decreased as the formalin concentration increases. It was noted that formaldehyde possesses refractive index of 1.3746 which is higher than water (1.33). The mixture of formaldehyde and water in different concentrations altered the refractive index of the solution as well as the air that surrounded the nanorods when evaporated into air. As a result, changing in light intensity was observed when the sensor was exposed against different concentrations of formaldehyde vapor. However, since it was minimal difference of relative index between water and formaldehyde, therefore small change of intensity was observed.

Figure 5.18 shows the performance of fabricated sensor in detecting formaldehyde vapor at 90% of RH level (considering the vapor was fully spread in the chamber). The sensing response shows that the output voltage reduced as the concentrations of vapor increases. It was found that the response towards concentrations to form a good linear trend line of 98.06%. The sensitivity of the sensor was observed to be approximate 0.0168 V/% which is good considering the capability of the fabricated sensor in detecting as low as 1% of the concentrations. Table 5.3 summarizes the total reduction of voltage (ΔV) in average at every tested vapor concentration with respected to 0%. The data clearly shows that the fabricated sensor responded well to the changes of vapor concentrations. The accumulated reduction of output voltage was consistently increased as the concentration increases. It was found that the total reduction due to the exposure to 5% of vapor concentrations with respected to 0% was 0.0856 V.

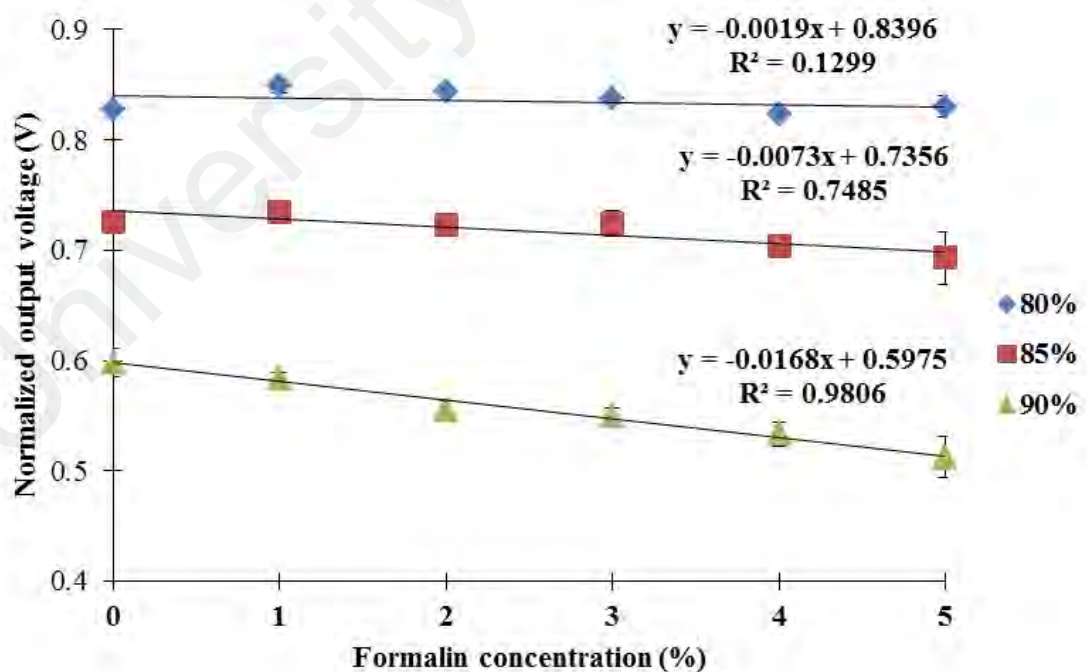


Figure 5.18 Formaldehyde vapor sensing performance.

Table 5.3 The total reduction of output voltage in average upon exposure to formaldehyde vapor.

Formalin concentration (%)	ΔV (V)
1	-0.0134
2	-0.0423
3	-0.0487
4	-0.0646
5	-0.0856

Table 5.4 summarizes the comparison of sensing characterization between relative humidity and formaldehyde vapor by using the developed sensing device. Overall, it shown that the sensitivity of formaldehyde vapor sensing is higher than humidity sensing. It shows that the ZnO is highly sensitive to the changes of formaldehyde vapor compared to humidity. However, it was noted in previous result that the measurement value of formaldehyde vapor sensing affected by the presence of humidity. The main objective of this experiment was to characterized the effectiveness of the developed sensor device to detect the lowest concentration of formaldehyde vapor. The limitation of the developed sensing device is the selectivity of the sensing parameter. The device has no capability to differentiate between the two parameters. Tthe selectivity of the sensing device towards humidity and formaldehyde can be improved by introducing two-sensor array which provide differences response between humidity and formaldehyde vapor. This method can be proposed in future research work in order to produce a sensor device that can detect more than one parameter.

Table 5.4 Comparison between relative humidity and formaldehyde vapor sensing by the developed sensor device.

	Relative Humidity	Formaldehyde Vapor
Sensing element	ZnO nanorods	
Refractive index	~ 1.00 - 1.33	1.3746
Tested concentration	35% to 90%	0% - 5%
Average sensitivity	12 mV / %RH	16.8 mV/%

5.5 Summary

The study presents the development of a simple integrated ZnO based sensor device for humidity and vapor sensing applications. The sensor device was fabricated using glass substrate coated with ZnO nanorods grown by means of a low cost hydrothermal process. Utilization of commercial LEDs as light source and low cost photodiode integrated to the Arduino platform for data processing, leads to the realization of a simple and cost effective sensor device. By employing intensity modulated/direct detection (IM/DD) sensing scheme, it provides a simple sensing mechanism, circumventing the need of more complex alternatives.

The sensor device was successfully characterized with humidity and formaldehyde vapor concentrations. With an increasing of humidity, the output voltage was found to reduce in non-linear trend with good sensitivity. The integrated sensing device was found of having fast response and recovery time which useful in real-time measurement. It also responded well in detecting formaldehyde vapor concentrations with good stability at small change of concentrations as low as 1%.

CHAPTER 6: CONCLUSION AND FUTURE WORK

6.1 Conclusion

The growth of ZnO nanorods have been successfully performed onto glass substrates via hydrothermal synthesis method. The effect of ZnO coating length was demonstrated by fabricating the ZnO nanorods layer in a triangular shaped. From the optical characterization it was found that the longer ZnO coating length exhibited higher leakage of light via ZnO scattering which resulted lower intensity of light at the output. The fabrication was carried out on three different growth times (5 h, 10 h and 15 h) which resulted the longer length and larger diameter of the nanorods as the growth time increases. The scattering effect by ZnO nanorods showed that the growth process at 10 h produces higher ZnO scattering coefficient which leads to higher leakage of light. Investigation on forward and backward scattering was found that the longer growth time reduced the forward scattering by nanorods. In contrast, backward scattering dominates where the trend improved as the forward scattering decays. These behaviors were affected by the density of the ZnO nanorods which was observed of having higher density as the growth time increases. Higher density of nanorods reduces amount of light to be scattered out by the nanorods thus more light was reflected and guided back into the glass substrate.

A new theoretical model on the optical dynamic range maximization for humidity sensing was established. The similar triangular ZnO nanorods coated glass substrates with different processing time were used to achieve possible combinations of ZnO conditions (coating length and growth durations). The study was successfully conducted theoretically and experimentally for identification of optimum operating condition for a sensing device. The experimental data were correlated reasonably well to the first order approximation of theoretical model. The investigation revealed that the

best sensing performance of any fabricated sensing device can be accomplished by achieving the optimum operating condition, independent of nanorods growth parameters or coated area. This study can be a standard reference technique for designing a compact humidity sensing device.

Realization of a simple integrated and cost effective intensity modulation (IM) based humidity and vapor detection system utilizing ZnO nanorods as active material has been successfully demonstrated. The device comprises of ZnO nanorods optimally grown on a glass substrate and mounted on 3D printed platform for precise alignment with green LED setup for edge excitation. Arduino platform was utilized for signal processing of the transmitted light detection. The integrated sensing device was experimentally validated with relative humidity concentrations from 35% to 90%. The total voltage drops of 750 mV in a non-linear fashion was observed upon testing at the highest tested humidity level. The average sensitivity of the sensing device was recorded at -12 mV/% with an average response time of 3.8 s measured at 85% of RH with respect to ambient humidity condition (50%). The recovery time of the sensing device was observed to be quicker at the rate of 2.2 s in average.

In further characterization, the application of the integrated sensing device was extended for the detection of formaldehyde vapor concentrations. A significant response was recorded with the reduction of output voltage of 0.0856 V when varying the concentrations between 1% and 5%. The performance of the sensor device exhibited good sensing sensitivity and linearity of -0.0168 V/% and 98.06%, correspondingly. The sensor device revealed a good stability in the measurement as low as 1% of formaldehyde vapor concentration for a prolonged time of 600 s.

6.2 Future Work

As for recommendation of future work, it was noted that there are slight discrepancies between the theoretical and experimental approach in the first order approximation of optical dynamic range maximization model. This can be improved by including more parameters such as incident angle and wavelength of light source into the model to refine future analysis as a second order approximation model.

Future work can also be focused on the deposition of nanoparticles such as gold (Au), silver (Ag), platinum (Pt) or palladium (Pd) onto existing ZnO nanorods to understand the effect of the material to the performance of a sensing device. Lastly, a dedicated processing chip can be proposed in future to eliminate the usage of commercial programmable platform thus can reduce the overall size of the device towards a small scale sensing device.

REFERENCES

- Ahuja, D., & Parande, D. (2012). Optical Sensors and Their Applications. *Journal of Scientific Research and Reviews*, 1(5), 060-068.
- Akita, S., Sasaki, H., Watanabe, K., & Seki, A. (2010). A Humidity Sensor Based on a Hetero-Core Optical Fiber. *Sensors and Actuators B: Chemical*, 147(2), 385-391.
- Allen, B. L., Kichambare, P. D., & Star, A. (2007). Carbon Nanotube Field-Effect-Transistor-Based Biosensors. *Advanced Materials*, 19(11), 1439-1451.
- Alsmo, T., & Alsmo, C. (2014). Ventilation and Relative Humidity in Swedish Buildings. *Journal of Environmental Protection*, 5(11), 1022-1036.
- Amin, G., Asif, M., Zainelabdin, A., Zaman, S., Nur, O., & Willander, M. (2011). Influence of Ph, Precursor Concentration, Growth Time, and Temperature on the Morphology of ZnO Nanostructures Grown by the Hydrothermal Method. *Journal of Nanomaterials*, 2011, 1-9.
- Aneesh, R., & Khijwania, S. K. (2011). Zinc Oxide Nanoparticle Based Optical Fiber Humidity Sensor Having Linear Response Throughout a Large Dynamic Range. *Applied optics*, 50(27), 5310-5314.
- Anusha, J. R., Kim, H.-J., Fleming, A. T., Das, S. J., Yu, K.-H., Kim, B. C., & Raj, C. J. (2014). Simple Fabrication of ZnO/Pt/Chitosan Electrode for Enzymatic Glucose Biosensor. *Sensors and Actuators B: Chemical*, 202, 827-833.
- Apiwattanadej, T., Sritongkham, P., & Mohammed, W. S. (2015). The Scattering Pattern Study of Zinc Oxide Nanorod on Silica Glass Substrate for Protein Immobilization Platform. *International Journal of Advances in Science Engineering and Technology*, 3(3), 80-83.
- Arasu, K. (2017). *Automated Experimental Procedure Using Sensors and Arduino*. Paper presented at the 2017 International Conference on Inventive Computing and Informatics (ICICI).
- Arifin, N. A., & Denan, Z. (2015). An Analysis of Indoor Air Temperature and Relative Humidity in Office Room with Various External Shading Devices in Malaysia. *Procedia - Social and Behavioral Sciences*, 179, 290-296.

- Ascorbe, J., Corres, J., Arregui, F., & Matias, I. (2017). Recent Developments in Fiber Optics Humidity Sensors. *Sensors*, 17(4), 1-23.
- Azad, S., Sadeghi, E., Parvizi, R., & Mazaheri, A. (2017). Fast Response Relative Humidity Clad-Modified Multimode Optical Fiber Sensor with Hydrothermally Dimension Controlled ZnO Nanorods. *Materials Science in Semiconductor Processing*, 66, 200-206.
- Banerjee, D., Lao, J., Wang, D., Huang, J., Ren, Z., Steeves, D., Kimball, B., & Sennett, M. (2003). Large-Quantity Free-Standing ZnO Nanowires. *Applied Physics Letters*, 83(10), 2061-2063.
- Barrett, S. F. (2013). Arduino Microcontroller Processing for Everyone! *Synthesis Lectures on Digital Circuits and Systems*, 8(4), 1-513.
- Baruah, S. (2011). *Hydrothermal Growth of Zinc Oxide Nanostructures for Environmental Applications*. (Doctor of Engineering in Nanotechnology), Asian Institute of Technology, Thailand.
- Baruah, S., & Dutta, J. (2009a). Effect of Seeded Substrates on Hydrothermally Grown ZnO Nanorods. *Journal of Sol-Gel Science and Technology*, 50(3), 456-464.
- Baruah, S., & Dutta, J. (2009b). Hydrothermal Growth of ZnO Nanostructures. *Science and Technology of Advanced Materials*, 10(1), 1-18.
- Baruah, S., & Dutta, J. (2009c). Ph-Dependent Growth of Zinc Oxide Nanorods. *Journal of Crystal Growth*, 311(8), 2549-2554.
- Baruah, S., K Pal, S., & Dutta, J. (2012). Nanostructured Zinc Oxide for Water Treatment. *Nanoscience & Nanotechnology-Asia*, 2(2), 90-102.
- Bass, M., Stryland, E. W. V., Williams, D. R., & Wolfe, W. L. (1995). *Handbook of Optics, Volume II: Device, Measurements & Properties* (2 ed. Vol. 2): McGraw Hill.
- Berthold, J. W. (1995). Historical Review of Microbend Fiber-Optic Sensors. *Journal of Lightwave Technology*, 13(7), 1193-1199.
- Bhattacharya, S., & Sasmal, M. (2015). *Solution Process Synthesized ZnO Nanoparticle for an Intelligent Humidity Sensor*. Paper presented at the Soft Computing and Machine Intelligence (SCMI), 2015 Second International Conference on Soft Computing and Machine Intelligence.

- Bhattacharyya, D., Dey, A., & Mukherjee, P. (1977). Water Chemisorption and Electrical Conductivity of Zinc Oxide. *Journal of The Research Institute For Catalysis Hokkaido University*, 24(3), 194-157.
- Bhattacharyya, P., Basu, P., Saha, H., & Basu, S. (2007). Fast Response Methane Sensor Using Nanocrystalline Zinc Oxide Thin Films Derived by Sol–Gel Method. *Sensors and Actuators B: Chemical*, 124(1), 62-67.
- BiacoreAB. (1994). Biacore Technology Handbook.
- Bogue, R. (2015). Detecting Gases with Light: A Review of Optical Gas Sensor Technologies. *Sensor Review*, 35(2), 133-140.
- Bohren, C. F., & Huffman, D. R. (2008). *Absorption and Scattering of Light by Small Particles*: John Wiley & Sons.
- Bora, T., Fallah, H., Chaudhari, M., Apiwattanadej, T., Harun, S. W., Mohammed, W. S., & Dutta, J. (2014). Controlled Side Coupling of Light to Cladding Mode of ZnO Nanorod Coated Optical Fibers and Its Implications for Chemical Vapor Sensing. *Sensors and Actuators B: Chemical*, 202, 543-550.
- Bora, T., Sathe, P., Laxman, K., Dobretsov, S., & Dutta, J. (2017). Defect Engineered Visible Light Active ZnO Nanorods for Photocatalytic Treatment of Water. *Catalysis Today*, 284, 11-18.
- Brugger, J. (2009). Nanotechnology Impact on Sensors. *Nanotechnology*, 20(43), 1-3.
- Burge, P. (2004). Sick Building Syndrome. *Occupational and environmental medicine*, 61(2), 185-190.
- Cao, H., Zhao, Y., Ong, H., Ho, S., Dai, J. Y., Wu, J. Y., & Chang, R. (1998). Ultraviolet Lasing in Resonators Formed by Scattering in Semiconductor Polycrystalline Films. *Applied Physics Letters*, 73(25), 3656-3658.
- Carrascosa, L. G., Moreno, M., Álvarez, M., & Lechuga, L. M. (2006). Nanomechanical Biosensors: A New Sensing Tool. *TrAC Trends in Analytical Chemistry*, 25(3), 196-206.
- Carter, B., & Brown, T. R. (2001). *Handbook of Operational Amplifier Applications*: Texas Instruments Dallas, Tex, USA.

- Chang, C.-C., Chiu, N.-F., Lin, D. S., Chu-Su, Y., Liang, Y.-H., & Lin, C.-W. (2010). High-Sensitivity Detection of Carbohydrate Antigen 15-3 Using a Gold/Zinc Oxide Thin Film Surface Plasmon Resonance-Based Biosensor. *Analytical chemistry*, 82(4), 1207-1212.
- Chauhan, P., & Sharma, S. (2016). Nanomaterials for Sensing Applications. *Journal of Nanomedicine Research*, 3(5), 1-8.
- Chen, D., Jiao, X., & Cheng, G. (1999). Hydrothermal Synthesis of Zinc Oxide Powders with Different Morphologies. *Solid State Communications*, 113(6), 363-366.
- Chen, H., Roco, M. C., Son, J., Jiang, S., Larson, C. A., & Gao, Q. (2013). Global Nanotechnology Development from 1991 to 2012: Patents, Scientific Publications, and Effect of Nsf Funding. *Journal of nanoparticle research*, 15(9), 1-21.
- Chen, Y., Bagnall, D., & Yao, T. (2000). ZnO as a Novel Photonic Material for the Uv Region. *Materials Science and Engineering: B*, 75(2-3), 190-198.
- Cherin, A. H. (1983). *An Introduction to Optical Fibers*: McGraw-Hill.
- Chiu, W., Khiew, P., Cloke, M., Isa, D., Tan, T., Radiman, S., Abd-Shukor, R., Hamid, M. A., Huang, N., & Lim, H. (2010). Photocatalytic Study of Two-Dimensional ZnO Nanopellets in the Decomposition of Methylene Blue. *Chemical Engineering Journal*, 158(2), 345-352.
- Choi, N.-J., Lee, H.-K., Moon, S. E., Yang, W. S., & Kim, J. (2013). Volatile Organic Compound Gas Sensor Based on Aluminum-Doped Zinc Oxide with Nanoparticle. *Journal of Nanoscience and Nanotechnology*, 13(8), 5481-5484.
- Choudhury, P. K. (1998). Optical Sensors in Environmental Monitoring. *Current Science*, 74(9), 723-725.
- Chung, P.-R., Tzeng, C.-T., Ke, M.-T., & Lee, C.-Y. (2013). Formaldehyde Gas Sensors: A Review. *Sensors (Basel, Switzerland)*, 13(4), 4468-4484.
- Connelly, M. (2004). Fiber Sensors. In *Encyclopedia of Modern Optics* (1st ed.): Elsevier.
- Correa-Mena, A., González, L., Quintero-Rodríguez, L., & Zaldivar-Huerta, I. (2017). *Review on Integrated Optical Sensors and Its Applications*. Paper presented at the Humanitarian Technology Conference (MHTC), IEEE Mexican.

- Correia, S. F., Antunes, P., Pecoraro, E., Lima, P. P., Varum, H., Carlos, L. D., Ferreira, R. A., & André, P. S. (2012). Optical Fiber Relative Humidity Sensor Based on a Fbg with a Di-Ureasil Coating. *Sensors*, 12(7), 8847-8860.
- Culshaw, B. (2015). *Fibre Optics in Sensing and Measurement—Achievements and Opportunities*. Paper presented at the Opto-Electronics and Applied Optics (IEM OPTRONIX), 2015 2nd International Conference on Opto-Electronics and Applied Optics (IEM OPTRONIX).
- Dar, A., Shafique, U., Anwar, J., Waheed uz, Z., & Naseer, A. (2016). A Simple Spot Test Quantification Method to Determine Formaldehyde in Aqueous Samples. *Journal of Saudi Chemical Society*, 20, S352-S356.
- Dedova, T., Volobujeva, O., Klauson, J., Mere, A., & Krunks, M. (2007). Zn Nanorods Via Spray Deposition of Solutions Containing Zinc Chloride and Thiocarbamide. *Nanoscale research letters*, 2(8), 391-396.
- Dietrich, A. M., & daCosta, W. F. (1997). Chemical Species. *Water Environment Research*, 69(4), 391-403.
- Dikovska, A. O., Atanasov, P., Andreev, A. T., Zafirova, B., Karakoleva, E., & Stoyanov, T. (2007). Zn Thin Film on Side Polished Optical Fiber for Gas Sensing Applications. *Applied Surface Science*, 254(4), 1087-1090.
- Dikovska, A. O., Atanasov, P. A., Tonchev, S., Ferreira, J., & Escoubas, L. (2007). Periodically Structured Zn Thin Films for Optical Gas Sensor Application. *Sensors and Actuators A: Physical*, 140(1), 19-23.
- Dixit, S., Srivastava, A., Shukla, R., & Srivastava, A. (2007). Zn Thick Film Based Opto-Electronic Humidity Sensor for a Wide Range of Humidity. *Optical review*, 14(4), 186-188.
- Ebbesen, T., & Ajayan, P. (1992). Large-Scale Synthesis of Carbon Nanotubes. *Nature*, 358(6383), 1-12.
- Elosua, C., Matias, I., Barriain, C., & Arregui, F. (2006). Volatile Organic Compound Optical Fiber Sensors: A Review. *Sensors*, 6(11), 1440-1465.
- Emanetoglu, N., Gorla, C., Liu, Y., Liang, S., & Lu, Y. (1999). Epitaxial Zn Piezoelectric Thin Films for Saw Filters. *Materials Science in Semiconductor Processing*, 2(3), 247-252.

- Emphasis, K., Vequizo, R., Odarve, M., Gambe, J., & Alguno, A. (2015). *Growth of Zinc Oxide Nanostructures on Glass Substrates for Ethanol Gas Sensor Application*. Paper presented at the IOP Conference Series: Materials Science and Engineering.
- Fallah, H., Chaudhari, M., Bora, T., Harun, S., Mohammed, W., & Dutta, J. (2013). Demonstration of Side Coupling to Cladding Modes through Zinc Oxide Nanorods Grown on Multimode Optical Fiber. *Optics letters*, 38(18), 3620-3622.
- Farahani, H., Wagiran, R., & Hamidon, M. (2014). Humidity Sensors Principle, Mechanism, and Fabrication Technologies: A Comprehensive Review. *Sensors*, 14(5), 7881-7939.
- Feng, Q., Zhao, R., Ma, X., & Shi, Y. (2013, 16-18 Aug. 2013). *Preparation of ZnO Semiconductor Formaldehyde Gas Sensor*. Paper presented at the Proceedings of 2013 2nd International Conference on Measurement, Information and Control.
- Ferguson, J. A., Boles, T. C., Adams, C. P., & Walt, D. R. (1996). A Fiber-Optic DNA Biosensor Microarray for the Analysis of Gene Expression. *Nature biotechnology*, 14(13), 1681-1684.
- Fidanboyly, K., & Efendioglu, H. (2009). *Fiber Optic Sensors and Their Applications*. Paper presented at the 5th International Advanced Technologies Symposium (IATS'09).
- Fiore, J. M. (1992). *Operational Amplifiers and Linear Integrated Circuits: Theory and Application*: West Publishing Company.
- Fonoberov, V. A., & Balandin, A. A. (2006). ZnO Quantum Dots: Physical Properties and Optoelectronic Applications. *Journal of Nanoelectronics and Optoelectronics*, 1(1), 19-38.
- Fritz, J., Baller, M., Lang, H., Rothuizen, H., Vettiger, P., Meyer, E., Güntherodt, H.-J., Gerber, C., & Gimzewski, J. (2000). Translating Biomolecular Recognition into Nanomechanics. *Science*, 288(5464), 316-318.
- Gadallah, A.-S., Nomenyo, K., Couteau, C., Rogers, D. J., & Léronnel, G. (2013). Stimulated Emission from ZnO Thin Films with High Optical Gain and Low Loss. *Applied Physics Letters*, 102(17), 1-4.
- Galadima, A. A. (2014). *Arduino as a Learning Tool*. Paper presented at the 2014 11th International Conference on Electronics, Computer and Computation (ICECCO).

- Gaston, A., Lozano, I., Perez, F., Auza, F., & Sevilla, J. (2003). Evanescent Wave Optical-Fiber Sensing (Temperature, Relative Humidity, and Ph Sensors). *IEEE Sensors Journal*, 3(6), 806-811.
- Ghadiry, M., Gholami, M., Lai, C. K., Ahmad, H., & Chong, W. Y. (2016). Ultra-Sensitive Humidity Sensor Based on Optical Properties of Graphene Oxide and Nano-Anatase Tio₂. *PLOS ONE*, 11(4), 1-14.
- Gholamzadeh, B., & Nabovati, H. (2008). Fiber Optic Sensors. *World Academy of Science, Engineering and Technology*, 42(3), 335-340.
- Giallorenzi, T. G., Bucaro, J. A., Dandridge, A., Sigel, G. H., Cole, J. H., Rashleigh, S. C., & Priest, R. G. (1982). Optical Fiber Sensor Technology. *IEEE transactions on microwave theory and techniques*, 30(4), 472-511.
- Grattan, K. T. V., & Sun, T. (2000). Fiber Optic Sensor Technology: An Overview. *Sensors and Actuators A: Physical*, 82(1), 40-61.
- Griffiths, J., & Robinson, S. (1999). The Oxylite: A Fibre-Optic Oxygen Sensor. *The British journal of radiology*, 72(859), 627-630.
- Haarindraprasad, R., Hashim, U., Gopinath, S. C., Kashif, M., Veeradasan, P., Balakrishnan, S., Foo, K., & Poopalan, P. (2015). Low Temperature Annealed Zinc Oxide Nanostructured Thin Film-Based Transducers: Characterization for Sensing Applications. *PLOS ONE*, 10(7), 1-20.
- Hambali, N. A., Yahaya, H., Mahmood, M. R., Terasako, T., & Hashim, A. M. (2014). Synthesis of Zinc Oxide Nanostructures on Graphene/Glass Substrate by Electrochemical Deposition: Effects of Current Density and Temperature. *Nanoscale research letters*, 9(1), 1-7.
- Haque, F. Z., Singh, N., Pandey, P., & Parra, M. R. (2013). Study of Zinc Oxide Nano/Micro Rods Grown on Ito and Glass Substrates. *Optik-International Journal for Light and Electron Optics*, 124(20), 4167-4171.
- Harith, Z., Batumalay, M., Irawati, N., Harun, S., Arof, H., & Ahmad, H. (2017). Relative Humidity Sensor Employing Tapered Plastic Optical Fiber Coated with Seeded Al-Doped Zno. *Optik-International Journal for Light and Electron Optics*, 144, 257-262.
- Harith, Z., Irawati, N., Rafaie, H. A., Batumalay, M., Harun, S. W., Nor, R. M., & Ahmad, H. (2015). Tapered Plastic Optical Fiber Coated with Al-Doped Zno Nanostructures for Detecting Relative Humidity. *IEEE Sensors Journal*, 15(2), 845-849.

- Healey, B. G., Li, L., & Walt, D. R. (1997). Multianalyte Biosensors on Optical Imaging Bundles. *Biosensors and Bioelectronics*, 12(6), 521-529.
- Hentschel, C., GmbH, H.-P., & Ltd, H.-P. (1983). *Fiber Optics Handbook*: Hewlett-Packard GmbH.
- Hodgkinson, J., & Tatam, R. P. (2012). Optical Gas Sensing: A Review. *Measurement Science and Technology*, 24(1), 1-59.
- Horzum, N., Taşçıoğlu, D., Okur, S., & Demir, M. M. (2011). Humidity Sensing Properties of ZnO-Based Fibers by Electrospinning. *Talanta*, 85(2), 1105-1111.
- Hu, W., Chen, S., Liu, L., Ding, B., & Wang, H. (2011). Formaldehyde Sensors Based on Nanofibrous Polyethyleneimine/Bacterial Cellulose Membranes Coated Quartz Crystal Microbalance. *Sensors and Actuators B: Chemical*, 157(2), 554-559.
- Husain, I., Choudhury, A., & Nath, P. (2013). Fiber-Optic Volumetric Sensor Based on Beer-Lambert Principle. *IEEE Sensors Journal*, 13(9), 3345-3346.
- Iijima, S. (1991). Helical Microtubules of Graphitic Carbon. *Nature*, 354(6348), 56-58.
- Ismail, A., El-Midany, A., Abdel-Aal, E., & El-Shall, H. (2005). Application of Statistical Design to Optimize the Preparation of ZnO Nanoparticles Via Hydrothermal Technique. *Materials Letters*, 59(14-15), 1924-1928.
- Ismail, A., Mamat, M., & Rusop, M. (2015). Humidity Sensor-a Review of Nanostructured Zinc Oxide (ZnO)-Based Humidity Sensor. *Advanced Materials Research*, 1109, 395-400.
- Jali, M. H., Rahim, H. R. A., Johari, M. A. M., Hamid, S. S., Yusof, H. H. M., Thokchom, S., Wang, P., & Harun, S. W. (2019). Optical Characterization of Different Waist Diameter on Microfiber Loop Resonator Humidity Sensor. *Sensors and Actuators A: Physical*, 285, 200-209.
- Jiang, H., Yang, R., Tang, X., Burnett, A., Lan, X., Xiao, H., & Dong, J. (2013). Multilayer Fiber Optic Sensors for in Situ Gas Monitoring in Harsh Environments. *Sensors and Actuators B: Chemical*, 177, 205-212.
- Jiang, T., Zhou, X., Zhang, J., Zhu, J., Li, X., & Li, T. (2006). *Study of Humidity Properties of Zinc Oxide Modified Porous Silicon*. Paper presented at the Sensors, 2006. 5th IEEE Conference on Sensors.

- Jiang, X., Li, C., Chi, Y., & Yan, J. (2010). Tg-Ftir Study on Urea-Formaldehyde Resin Residue During Pyrolysis and Combustion. *Journal of Hazardous Materials*, 173(1), 205-210.
- Jing, Q., Fu, W., Li, W., Yang, H., Li, M., Ma, J., Zhou, X., Sun, M., Zhao, H., & Zhang, Y. (2012). Synthesis of Snowflake-Like Multi-Layered ZnO with Controllable Pore Sizes and Its Photocatalytic Property. *Applied Surface Science*, 258(8), 3604-3610.
- Kalyani, V. L., & Sharma, V. (2016). Optical Sensors and Their Use in Medical Field. *Journal of Management Engineering and Information Technology (JMEIT)*, 3(5), 1-4.
- Kannan, P. K., & Saraswathi, R. (2017). An Impedance Sensor for the Detection of Formaldehyde Vapor Using ZnO Nanoparticles. *Journal of Materials Research*, 32(14), 2800-2809.
- Keiser, G. (2010). *Optical Fiber Communications*: McGraw-Hill Education.
- Keyvani, A. (2007). Huge Opportunities for Industry of Nanofibrous Concrete Technology. *International Journal of Nanoscience and Nanotechnology*, 3(1), 3-12.
- Khalil, S. E., Bansal, L., & El-Sherif, M. A. (2004). Intrinsic Fiber Optic Chemical Sensor for the Detection of Dimethyl Methylphosphonate. *Optical Engineering*, 43(11), 2683-2689.
- Khijwania, S. K., Srinivasan, K. L., & Singh, J. P. (2005a). An Evanescent-Wave Optical Fiber Relative Humidity Sensor with Enhanced Sensitivity. *Sensors and Actuators B: Chemical*, 104(2), 217-222.
- Khijwania, S. K., Srinivasan, K. L., & Singh, J. P. (2005b). Performance Optimized Optical Fiber Sensor for Humidity Measurement. *Optical Engineering*, 44(3), 1-7.
- Kiasari, N. M., Soltanian, S., Gholamkhash, B., & Servati, P. (2014). Environmental Gas and Light Sensing Using ZnO Nanowires. *IEEE Transactions on Nanotechnology*, 13(2), 368-374.
- Kim, H.-K., Sathaye, S. D., Hwang, Y.-K., Jung, S.-H., Hwang, J.-S., Kwon, S.-H., Park, S.-E., & Chang, J.-S. (2005). Humidity Sensing Properties of Nanoporous TiO₂-SnO₂ Ceramic Sensors. *Bulletin of the Korean Chemical Society*, 26(11), 1881-1884.

- Kitsomboonloha, R., Baruah, S., Myint, M. T. Z., Subramanian, V., & Dutta, J. (2009). Selective Growth of Zinc Oxide Nanorods on Inkjet Printed Seed Patterns. *Journal of Crystal Growth*, 311(8), 2352-2358.
- Kołodziejczak-Radzimska, A., & Jesionowski, T. (2014). Zinc Oxide—from Synthesis to Application: A Review. *Materials*, 7(4), 2833-2881.
- Kong, T., Chen, Y., Ye, Y., Zhang, K., Wang, Z., & Wang, X. (2009). An Amperometric Glucose Biosensor Based on the Immobilization of Glucose Oxidase on the ZnO Nanotubes. *Sensors and Actuators B: Chemical*, 138(1), 344-350.
- KOPP-Glass. (2016). The Properties of Glass. from KOPP Glass <http://www.koppglass.com/home/>
- Kraft, M. (2006). Vibrational Spectroscopic Sensors Fundamentals, Instrumentation and Applications. In *Optical Chemical Sensors* (pp. 117-155): Springer.
- Krätschmer, W., Lamb, L. D., Fostiropoulos, K., & Huffman, D. R. (1990). Solid C60: A New Form of Carbon. *Nature*, 347(6291), 354-358.
- Kresge, C., Leonowicz, M., Roth, W. J., Vartuli, J., & Beck, J. (1992). Ordered Mesoporous Molecular Sieves Synthesized by a Liquid-Crystal Template Mechanism. *Nature*, 359(6397), 710-712.
- Kulkarni, S. S., & Shirsa, M. (2015). Optical and Structural Properties of Zinc Oxide Nanoparticles. *IJARPS*, 2, 14-18.
- Kumar, S. A., & Chen, S. M. (2008). Nanostructured Zinc Oxide Particles in Chemically Modified Electrodes for Biosensor Applications. *Analytical Letters*, 41(2), 141-158.
- Lai, H.-Y., & Chen, C.-H. (2012). Highly Sensitive Room-Temperature Co Gas Sensors: Pt and Pd Nanoparticle-Decorated In₂O₃ Flower-Like Nanobundles. *Journal of Materials Chemistry*, 22(26), 13204-13208.
- Leal-Junior, A., Frizzera-Neto, A., Marques, C., & Pontes, M. (2018). A Polymer Optical Fiber Temperature Sensor Based on Material Features. *Sensors*, 18(1), 1-10.
- Lee, B. (2003). Review of the Present Status of Optical Fiber Sensors. *Optical Fiber Technology*, 9(2), 57-79.

- Lee, C.-Y., Chiang, C.-M., Wang, Y.-H., & Ma, R.-H. (2007). A Self-Heating Gas Sensor with Integrated NiO Thin-Film for Formaldehyde Detection. *Sensors and Actuators B: Chemical*, 122(2), 503-510.
- Lee, C.-Y., Hsieh, P.-R., Lin, C.-H., Chou, P.-C., Fu, L.-M., & Chiang, C.-M. (2006). Mems-Based Formaldehyde Gas Sensor Integrated with a Micro-Hotplate. *Microsyst. Technol.*, 12(10), 893-898.
- Lee, J.-R., Dhital, D., & Yoon, D.-J. (2011). Investigation of Cladding and Coating Stripping Methods for Specialty Optical Fibers. *Optics and lasers in engineering*, 49(3), 324-330.
- Leidinger, M., Sauerwald, T., Conrad, T., Reimringer, W., Ventura, G., & Schütze, A. (2014). Selective Detection of Hazardous Indoor Vocs Using Metal Oxide Gas Sensors. *Procedia Engineering*, 87, 1449-1452.
- León, J. R. C., Martínez-González, R. F., Medina, A. M., & Peralta-Pelaez, L. A. (2017). Raspberry Pi and Arduino Uno Working Together as a Basic Meteorological Station. *International Journal of Computer Science & Information Technology (IJCSIT)*, 9(5), 97-104.
- LinearTechnology. (2000). Lt1884/Lt1885 Dual/Quad Rail-to-Rail Output, Picoamp Input Precision Op Amps. from Linear Technology www.linear-tech.com
- Liteplo, R., Beauchamp, R., Meek, M., & Chenier, R. (2002). Concise International Chemical Assessment Document 40: Formaldehyde. *Geneva: World Health Organization, Vol. 1.*
- Liu, C., Kuang, Q., Xie, Z., & Zheng, L. (2015). The Effect of Noble Metal (Au, Pd and Pt) Nanoparticles on the Gas Sensing Performance of SnO₂-Based Sensors: A Case Study on the {221} High-Index Faceted SnO₂ Octahedra. *CrystEngComm*, 17(33), 6308-6313.
- Liu, Y., Wang, L., Zhang, M., Tu, D., Mao, X., & Liao, Y. (2007). Long-Period Grating Relative Humidity Sensor with Hydrogel Coating. *IEEE Photonics Technology Letters*, 19(12), 880-882.
- Liu, Y., Zhang, Y., Lei, H., Song, J., Chen, H., & Li, B. (2012). Growth of Well-Arrayed ZnO Nanorods on Thinned Silica Fiber and Application for Humidity Sensing. *Optics express*, 20(17), 19404-19411.

- Lokman, A., Arof, H., Harun, S. W., Harith, Z., Rafea, H. A., & Nor, R. M. (2016). Optical Fiber Relative Humidity Sensor Based on Inline Mach–Zehnder Interferometer with ZnO Nanowires Coating. *IEEE Sensors Journal*, 16(2), 312-316.
- Lokman, M., Rahim, H., Harun, S., Hornyak, G., & Mohammed, W. (2016). Light Backscattering (Eg Reflectance) by Zinc Oxide Nanorods on Tips of Plastic Optical Fibers with Application for Humidity and Alcohol Vapor Sensing. *IET Micro Nano Letter*, 11(12), 832-836.
- Mahmood, M. A., Bora, T., & Dutta, J. (2013). Studies on Hydrothermally Synthesised Zinc Oxide Nanorod Arrays for Their Enhanced Visible Light Photocatalysis. *International Journal of Environmental Technology and Management*, 16(1-2), 146-159.
- Mário, F. S. F., Enrique, C.-C., David, J. O., José Miguel, L.-H., Xian, F., Wei, J., Yoonchan, J., Nathalie, P., Limin, T., Björn, M. R., Paul, M. P., Alexis, M., Max, D., Frank, V., & Qimin, Q. (2017). Roadmap on Optical Sensors. *Journal of Optics*, 19(8), 083001.
- Marquez, F., & Morant, C. (2015). Nanomaterials for Sensor Applications. *Soft Nanoscience Letters*, Vol.05No.01, 2.
- Medlock, R. (1987). *Fibre Optic Intensity Modulated Sensors*. Paper presented at the Optical Fiber Sensors.
- Mehrabani, A., & Golnabi, H. (2011). Investigation of Humidity Effect on the Air Refractive Index Using an Optical Fiber Design. *Journal of Applied Sciences*, 11(16), 3022-3027.
- Miles, D., Cameron, P., & Mattia, D. (2015). Hierarchical 3d ZnO Nanowire Structures Via Fast Anodization of Zinc. *Journal of Materials Chemistry A*, 3(34), 17569-17577.
- Mitsubayashi, K., Nishio, G., Sawai, M., Saito, T., Kudo, H., Saito, H., Otsuka, K., Nogue, T., & Marty, J.-L. (2008). A Bio-Sniffer Stick with Faldh (Formaldehyde Dehydrogenase) for Convenient Analysis of Gaseous Formaldehyde. *Sensors and Actuators B: Chemical*, 130(1), 32-37.
- Mohd Fudzi, L., Zainal, Z., Lim, H. N., Chang, S.-K., & Holi, A. M. (2018). Effect of Temperature and Growth Time on Vertically Aligned ZnO Nanorods by Simplified Hydrothermal Technique for Photoelectrochemical Cells. *Materials*, 11(5), 1-13.

- Morimoto, T., & Nagao, M. (1970). The Relation between the Amounts of Chemisorbed and Physisorbed Water on Zinc Oxide. *Bulletin of the Chemical Society of Japan*, 43(12), 3746-3750.
- Mulyanti, B., Ramza, H., Pawinanto, R., Abdurrahman, F., Sarah, L., Arsad, I. D. N., & Ab-Rahman, M. S. (2017). Modeling and Optimization of Fiber Optic Chemical Vapor Sensor. *Journal of Telecommunication, Electronic and Computer Engineering (JTEC)*, 9(2), 73-79.
- Muto, S., Suzuki, O., Amano, T., & Morisawa, M. (2003). A Plastic Optical Fibre Sensor for Real-Time Humidity Monitoring. *Measurement Science and Technology*, 14(6), 746-750.
- Nagao, M. (1971). Physisorption of Water on Zinc Oxide Surface. *The Journal of Physical Chemistry*, 75(25), 3822-3828.
- Narasimman, S., Dinesh, U., Balakrishnan, L., Meher, S., Sivacoumar, R., & Alex, Z. (2017). A Comparative Study on Structural, Optical and Humidity Sensing Characteristics of ZnO, SnO₂ and ZnO: SnO₂ Nanocomposite. *Sensor Letters*, 15(5), 440-447.
- Narayanaswamy, R., & Wolfbeis, O. S. (2013). *Optical Sensors: Industrial Environmental and Diagnostic Applications* (Vol. 1): Springer Science & Business Media.
- Nuasaen, S., Opaprakasit, P., & Tangboriboonrat, P. (2014). Hollow Latex Particles Functionalized with Chitosan for the Removal of Formaldehyde from Indoor Air. *Carbohydrate Polymers*, 101, 179-187.
- OSRAM. (2015). Sfh 203 P Silicon Pin Photodiode. from OSRAM Opto Semiconductors www.osram-os.com
- Oza, V., & Mehta, P. (2018). *Arduino Robotic Hand: Survey Paper*. Paper presented at the 2018 International Conference on Smart City and Emerging Technology (ICSCET).
- Pan, J., Cha, T.-G., Chen, H., & Choi, J. (2013). Carbon Nanotube-Based Optical Platforms for Biomolecular Detection. In *Carbon Nanotubes and Graphene for Photonic Applications* (pp. 270-303e): Elsevier.
- Pandit, S., Dasgupta, D., Dewan, N., & Prince, A. (2016). Nanotechnology Based Biosensors and Its Application. *The Pharma Innovation*, 5(6), 18-25.

- Parisi, A., Cino, A. C., Busacca, A. C., Cherchi, M., & Riva-Sanseverino, S. (2008). Integrated Optic Surface Plasmon Resonance Measurements in a Borosilicate Glass Substrate. *Sensors*, 8(11), 7113-7124.
- Patil, Y. S., Raghuvanshi, F. C., & Patil, I. D. (2016). Zinc Oxide Nanorods as H₂S Gas Sensor. *International Journal of Science and Research (IJSR)*, 5(7), 1140-1144.
- Patnaik Patnaikuni, D. R. (2017). A Comparative Study of Arduino, Raspberry Pi and Esp8266 as Iot Development Board. *International Journal of Advanced Research in Computer Science*, 8(5), 2350-2352.
- Patni, N., Pillai, S., & Mehta, T. (2015). Nano Technology in Chemical Sensors. In (pp. 6).
- Peng, L., Zhao, Q., Wang, D., Zhai, J., Wang, P., Pang, S., & Xie, T. (2009). Ultraviolet-Assisted Gas Sensing: A Potential Formaldehyde Detection Approach at Room Temperature Based on Zinc Oxide Nanorods. *Sensors and Actuators B: Chemical*, 136(1), 80-85.
- Perrone, G. (2018). *Optical Sensing Systems for Industrial and Medical Process Monitoring*. Paper presented at the CLEO: Applications and Technology.
- Polsonkram, D., Chamninok, P., Pukird, S., Chow, L., Lupan, O., Chai, G., Khallaf, H., Park, S., & Schulte, A. (2008). Effect of Synthesis Conditions on the Growth of ZnO Nanorods Via Hydrothermal Method. *Physica B: Condensed Matter*, 403(19-20), 3713-3717.
- Promnimit, S., Baruah, S., Lamdu, U., & Dutta, J. (2013). Hydrothermal Growth of ZnO Hexagonal Nanocrystals: Effect of Growth Conditions. *Journal of Nano Research*, 21, 57-63.
- Rackauskas, S., Barbero, N., Barolo, C., & Viscardi, G. (2017). ZnO Nanowire Application in Chemoresistive Sensing: A Review. *Nanomaterials*, 7(11), 1-13.
- Rafis, H., & Rahim, A. (2017). *Structured Growth of Zinc Oxide Nanorods on Plastic Optical Fiber and Light Side Coupling Towards Sensing Applications*. University of Malaya,
- Rahim, H. R. B. A., Lokman, M. Q. B., Harun, S. W., Dutta, J., & Mohammed, W. S. (2017). Temperature Sensing by Side Coupling of Light through Zinc Oxide Nanorods on Optical Fibers. *Sensors and Actuators A: Physical*, 257, 15-19.

- Rahim, H. R. B. A., Lokman, M. Q. B., Harun, S. W., Hornyak, G. L., Sterckx, K., Mohammed, W. S., & Dutta, J. (2016). Applied Light-Side Coupling with Optimized Spiral-Patterned Zinc Oxide Nanorod Coatings for Multiple Optical Channel Alcohol Vapor Sensing. *Journal of Nanophotonics*, 10(3), 1-17.
- Rahim, H. R. B. A., Manjunath, S., Fallah, H., Thokchom, S., Harun, S. W., Mohammed, W. S., Hornyak, L. G., & Dutta, J. (2016). Side Coupling of Multiple Optical Channels by Spiral Patterned Zinc Oxide Coatings on Large Core Plastic Optical Fibers. *IET Micro & Nano Letters*, 11(2), 122-126.
- Rahman, K. M., Subashini, M. M., Nador, M., & Tawfik, A. (2018). *Development of Bio-Shields for Arduino Uno*. Paper presented at the 2018 Advances in Science and Engineering Technology International Conferences (ASET).
- Rasmussen, J. W., Martinez, E., Louka, P., & Wingett, D. G. (2010). Zinc Oxide Nanoparticles for Selective Destruction of Tumor Cells and Potential for Drug Delivery Applications. *Expert opinion on drug delivery*, 7(9), 1063-1077.
- Renganathan, B., Sastikumar, D., Gobi, G., Yogamalar, N. R., & Bose, A. C. (2011). Nanocrystalline ZnO Coated Fiber Optic Sensor for Ammonia Gas Detection. *optics & laser technology*, 43(8), 1398-1404.
- Ribeiro, R. M., Canedo, J. L., Werneck, M. M., & Kawase, L. R. (2002). An Evanescent-Coupling Plastic Optical Fibre Refractometer and Absorptionmeter Based on Surface Light Scattering. *Sensors and Actuators A: Physical*, 101(1-2), 69-76.
- Ruchika, A. K. (2015). Performance Analysis of Zinc Oxide Based Alcohol Sensors. *Int. J. Appl. Sci. Eng. Res.*, 4(4), 428-436.
- Sabri, N., Aljunid, S., Salim, M., Ahmad, R., & Kamaruddin, R. (2013). *Toward Optical Sensors: Review and Applications*. Paper presented at the Journal of Physics: Conference Series.
- Saidin, N., Choo, T., & Kok, K. (2018). *Hydrothermal Growth of ZnO: A Substrate-Dependent Study on Nanostructures Formation*. Paper presented at the IOP Conference Series: Materials Science and Engineering.
- Saito, Y., Ichikawa, O., & Oshima, T. (1987). Waterproof Optical Fiber Cable and Method of the Production Thereof. In: Google Patents.
- Salah, G., Azzedine, T., & Chahra, B. (2014). Fabrication and Characterization of Zinc Oxide (Zno) Thin Films Based Humidity Sensor with Fast Response by Sol-Gel Method. *Journal of New Technology and Materials*, 277(1748), 1-4.

Salleh, M., & Zakaria, Z. (2015). Effect of Bending Optical Fiber on Bend Loss over a Long Period of Time. *ARPJ Journal of Engineering and Applied Sciences*, 10(16), 6732-6736.

Salthammer, T. (2015). The Formaldehyde Dilemma. *International Journal of Hygiene and Environmental Health*, 218(4), 433-436.

Samarasekara, P., Yapa, N., Kumara, N., & Perera, M. (2007). Co₂ Gas Sensitivity of Sputtered Zinc Oxide Thin Films. *Bulletin of Materials Science*, 30(2), 113-116.

Sberveglieri, G. (2012). *Gas Sensors: Principles, Operation and Developments*: Springer Science & Business Media.

Schmidt-Mende, L., & MacManus-Driscoll, J. L. (2007). ZnO-Nanostructures, Defects, and Devices. *Materials today*, 10(5), 40-48.

Semenkoff, M. (1992). Bending Effect on Light Propagation in an Optical Fiber: Application to a Temperature Sensor. *Optics and lasers in engineering*, 17(3-5), 179-186.

Sengupta, G., Ahluwalia, H., Banerjee, S., & Sen, S. (1979). Chemisorption of Water Vapor on Zinc Oxide. *Journal of Colloid and Interface Science*, 69(2), 217-224.

Setter, J., Hesketh, P. J., & Hunter, G. W. (2006). Sensors: Engineering Structures and Materials from Micro to Nano. *Interface*, 15(1), 66-69.

Shaharon, M. N., & Jalaludin, J. (2012). Thermal Comfort Assessment-a Study toward Workers' Satisfaction in a Low Energy Office Building. *American Journal of Applied Sciences*, 9(7), 1037-1045.

Shan, C., Liu, Z., & Hark, S. (2008). Temperature Dependent Photoluminescence Study on Phosphorus Doped ZnO Nanowires. *Applied Physics Letters*, 92(7), 1-3.

Shimizu, Y., Kuwano, N., Hyodo, T., & Egashira, M. (2002). High H₂ Sensing Performance of Anodically Oxidized TiO₂ Film Contacted with Pd. *Sensors and Actuators B: Chemical*, 83(1), 195-201.

Shinde, S., Shinde, P., Bhosale, C., & Rajpure, K. (2008). Optoelectronic Properties of Sprayed Transparent and Conducting Indium Doped Zinc Oxide Thin Films. *Journal of Physics D: Applied Physics*, 41(10), 1-6.

SHOTT. (2016). Tie-29 Refractive Index and Dispersion. from SHOTT AG

- Shukla, R., Srivastava, A., Pandey, A., Misra, K. P., & Pandey, M. (2015). Sensitivity of Polyaniline-Zinc Oxide Composite to Humidity. *Sensors & Transducers*, 188(5), 26-32.
- Silin, V., & Plant, A. (1997). Biotechnological Applications of Surface Plasmon Resonance. *Trends in Biotechnology*, 15(9), 353-359.
- Sin, N. M., Mamat, M., Musa, M., Aziz, A. A., & Rusop, M. (2012). *Effect of Growth Duration to the Electrical Properties of Zn Doped SnO₂ Thin Film toward Humidity Sensor Application*. Paper presented at the Business Engineering and Industrial Applications Colloquium (BEIAC), 2012 IEEE.
- Smrithi, V., Mathews, C. B., & Radhakrishnan, P. (2015). *Fiber Optic Evanescent Wave Sensor for the Measurement of Curcumin*. Paper presented at the 2015 Workshop on Recent Advances in Photonics (WRAP).
- Spencer, M. J. S. (2012). Gas Sensing Applications of 1d-Nanostructured Zinc Oxide: Insights from Density Functional Theory Calculations. *Progress in Materials Science*, 57(3), 437-486.
- Sterckx, K. (2015). Analysis of Op Amp Based Transimpedance Photo Receivers. *International Conference and Exhibition on Visible Light Communications 2015*, 1-6.
- Stewart, G., Jin, W., & Culshaw, B. (1997). Prospects for Fibre-Optic Evanescent-Field Gas Sensors Using Absorption in the near-Infrared. *Sensors and Actuators B: Chemical*, 38(1-3), 42-47.
- Su, S., Wu, W., Gao, J., Lu, J., & Fan, C. (2012). Nanomaterials-Based Sensors for Applications in Environmental Monitoring. *Journal of Materials Chemistry*, 22(35), 18101-18110.
- Suchorska-Woźniak, P., Nawrot, W., Rac, O., Fiedot, M., & Teterycz, H. (2016). *Improving the Sensitivity of the ZnO Gas Sensor to Dimethyl Sulfide*. Paper presented at the IOP Conference Series: Materials Science and Engineering.
- Sugunan, A., Warad, H. C., Boman, M., & Dutta, J. (2006). Zinc Oxide Nanowires in Chemical Bath on Seeded Substrates: Role of Hexamine. *Journal of Sol-Gel Science and Technology*, 39(1), 49-56.
- Tang, C.-F., Kumar, S. A., & Chen, S.-M. (2008). Zinc Oxide/Redox Mediator Composite Films-Based Sensor for Electrochemical Detection of Important Biomolecules. *Analytical biochemistry*, 380(2), 174-183.

- Tang, Y., Zeng, X., & Liang, J. (2010). Surface Plasmon Resonance: An Introduction to a Surface Spectroscopy Technique. *Journal of chemical education*, 87(7), 742-746.
- TexasInstrument. (2014). Lmx58-N Low-Power, Dual Operational Amplifiers. In (pp. 1-40).
- Torroja, Y., López, A., Portilla, J., & Riesgo, T. (2015). *A Serial Port Based Debugging Tool to Improve Learning with Arduino*. Paper presented at the 2015 Conference on Design of Circuits and Integrated Systems (DCIS).
- Tran, H. T. T., & Spencer, M. J. S. (2017). Zinc Oxide for Gas Sensing of Formaldehyde: Density Functional Theory Modelling of the Effect of Nanostructure Morphology and Gas Concentration on the Chemisorption Reaction. *Materials Chemistry and Physics*, 193, 274-284.
- Tsay, C.-Y., Fan, K.-S., Wang, Y.-W., Chang, C.-J., Tseng, Y.-K., & Lin, C.-K. (2010). Transparent Semiconductor Zinc Oxide Thin Films Deposited on Glass Substrates by Sol–Gel Process. *Ceramics international*, 36(6), 1791-1795.
- Udd, E. (1995). An Overview of Fiber-Optic Sensors. *Review of Scientific Instruments*, 66(8), 4015-4030.
- Udd, E., Blom, R. G., Tralli, D. M., Saaski, E. W., & Dokka, R. (1994). *Application of the Sagnac Interferometer-Based Strain Sensor to an Earth Movement Detection System*. Paper presented at the Smart Structures and Materials 1994: Smart Sensing, Processing, and Instrumentation.
- Udd, E., & Spillman Jr, W. B. (2011). *Fiber Optic Sensors: An Introduction for Engineers and Scientists*: John Wiley & Sons.
- Umar, A., Ribeiro, C., Al-Hajry, A., Masuda, Y., & Hahn, Y. (2009). Growth of Highly C-Axis-Oriented ZnO Nanorods on ZnO/Glass Substrate: Growth Mechanism, Structural, and Optical Properties. *The Journal of Physical Chemistry C*, 113(33), 14715-14720.
- Uskokovic, V. (2013). Entering the Era of Nanoscience: Time to Be So Small. *J Biomed Nanotechnol*, 9(9), 1441-1470.
- Vanheusden, K., Seager, C., Warren, W. t., Tallant, D., & Voigt, J. (1996). Correlation between Photoluminescence and Oxygen Vacancies in ZnO Phosphors. *Applied Physics Letters*, 68(3), 403-405.

- Wang, J. (2005). Nanomaterial-Based Electrochemical Biosensors. *Analyst*, 130(4), 421-426.
- Wang, J., Liu, L., Cong, S.-Y., Qi, J.-Q., & Xu, B.-K. (2008). An Enrichment Method to Detect Low Concentration Formaldehyde. *Sensors and Actuators B: Chemical*, 134(2), 1010-1015.
- Wang, J., Zhang, P., Qi, J.-Q., & Yao, P.-J. (2009). Silicon-Based Micro-Gas Sensors for Detecting Formaldehyde. *Sensors and Actuators B: Chemical*, 136(2), 399-404.
- Wang, S.-B., Hsiao, C.-H., Chang, S.-J., Lam, K.-T., Wen, K.-H., Young, S.-J., Hung, S.-C., & Huang, B.-R. (2012). CuO Nanowire-Based Humidity Sensor. *IEEE Sensors Journal*, 12(6), 1884-1888.
- Wang, Z. L. (2004). Zinc Oxide Nanostructures: Growth, Properties and Applications. *Journal of physics: condensed matter*, 16(25), 829-858.
- Werle, P., Maurer, K., Kormann, R., Mücke, R., D'Amato, F., Lancia, T., & Popov, A. (2002). Spectroscopic Gas Analyzers Based on Indium-Phosphide, Antimonide and Lead-Salt Diode-Lasers. *Spectrochimica Acta Part A: Molecular and Biomolecular Spectroscopy*, 58(11), 2361-2372.
- Wolfbeis, O. S. (2008). Fiber-Optic Chemical Sensors and Biosensors. *Analytical chemistry*, 80(12), 4269-4283.
- Xing, X., Li, Y., Deng, D., Chen, N., Liu, X., Xiao, X., & Wang, Y. (2016). Ag-Functionalized Macro-/Mesoporous Azo Synthesized by Solution Combustion for Voc's Gas Sensing Application. *RSC Advances*, 6(103), 101304-101312.
- Xiong, F., Zhu, W., Lin, H., & Meng, X. (2014). Fiber-Optic Sensor Based on Evanescent Wave Absorbance around 2.7 Mm for Determining Water Content in Polar Organic Solvents. *Applied Physics B*, 115(1), 129-135.
- Xuan, W., He, M., Meng, N., He, X., Wang, W., Chen, J., Shi, T., Hasan, T., Xu, Z., Xu, Y., & Luo, J. K. (2014). Fast Response and High Sensitivity ZnO/Glass Surface Acoustic Wave Humidity Sensors Using Graphene Oxide Sensing Layer. *Scientific Reports*, 4, 1-9.
- Yadav, B., Yadav, R., & Dubey, G. (2009). Optical Humidity Sensing Behaviour of Sol-Gel Processed Nanostructured ZnO Films. *Optica Applicata*, 39(3), 617-627.

- Ye, H., Chen, G., Niu, H., Zhu, Y., Shao, L., & Qiao, Z. (2013). Structures and Mechanisms of Water Adsorption on ZnO (0001) and GaN (0001) Surface. *The Journal of Physical Chemistry C*, 117(31), 15976-15983.
- Yeo, T., Sun, T., & Grattan, K. (2008). Fibre-Optic Sensor Technologies for Humidity and Moisture Measurement. *Sensors and Actuators A: Physical*, 144(2), 280-295.
- Yi, G.-C., Wang, C., & Park, W. I. (2005). ZnO Nanorods: Synthesis, Characterization and Applications. *Semiconductor Science and Technology*, 20(4), S22-S34.
- Yu, Z.-x., & Wang, H.-x. (2012). *Analysis of Theory and Experiment on Bend Loss Research by Otdr*. Paper presented at the World Automation Congress (WAC), 2012.
- Yuan, J., & El-Sherif, M. A. (2003). Fiber-Optic Chemical Sensor Using Polyaniline as Modified Cladding Material. *IEEE Sensors Journal*, 3(1), 5-12.
- Zamarreño, C., Hernaez, M., Del Villar, I., Matias, I., & Arregui, F. (2010). Tunable Humidity Sensor Based on Ito-Coated Optical Fiber. *Sensors and Actuators B: Chemical*, 146(1), 414-417.
- Zhang, L., Gu, F., Lou, J., Yin, X., & Tong, L. (2008). Fast Detection of Humidity with a Subwavelength-Diameter Fiber Taper Coated with Gelatin Film. *Optics express*, 16(17), 13349-13353.
- Zhou, K., Ji, X., Zhang, N., & Zhang, X. (2006). On-Line Monitoring of Formaldehyde in Air by Cataluminescence-Based Gas Sensor. *Sensors and Actuators B: Chemical*, 119(2), 392-397.
- Zhou, P., Zhu, X., Yu, J., & Xiao, W. (2013). Effects of Adsorbed F, Oh, and Cl Ions on Formaldehyde Adsorption Performance and Mechanism of Anatase TiO₂ Nanosheets with Exposed {001} Facets. *ACS applied materials & interfaces*, 5(16), 8165-8172.
- Zhou, Z., Zhao, Y., & Cai, Z. (2010). Low-Temperature Growth of ZnO Nanorods on PET Fabrics with Two-Step Hydrothermal Method. *Applied Surface Science*, 256(14), 4724-4728.

LIST OF PUBLICATIONS

Journal Publications (ISI)

1. **Yusof, H. H. M.**, Harun, S. W., Dimyati, K., Bora, T., Mohammed, W. S., & Dutta, J. (2018). Optical dynamic range maximization for humidity sensing by controlling growth of zinc oxide nanorods. *Photonics and Nanostructures-Fundamentals and Applications*, 30, 57-64.
2. **Yusof, H. H. M.**, Harun, S. W., Dimyati, K., Bora, T., Sterckx, K., Mohammed, W. S., & Dutta, J. (2018). Low-Cost Integrated Zinc Oxide Nanorod-Based Humidity Sensors for Arduino Platform. *IEEE Sensors Journal*, 19(7), 2442-2449.
3. **Yusof, H. H. M.**, Jali, M. H., Johari, M. A. M., Dimyati, K., Harun, S. W., Khasanah, M., & Yasin, M. (2019). Detection of Formaldehyde Vapor Using Glass Substrate Coated With Zinc Oxide Nanorods. *IEEE Photonics Journal*, 11(1), 1-9.
4. **Yusof, H. H. M.**, Rahim, H. R. A., Thokchom, S., Dimyati, K., & Harun, S. W. (2018). Uric acid sensing using tapered silica optical fiber coated with zinc oxide nanorods. *Microwave and Optical Technology Letters*, 60(3), 645-650.
5. Jali, M. H., Rahim, H. R. A., Johari, M. A. M., Hamid, S. S., **Yusof, H. H. M.**, Thokchom, S., Harun, S. W. (2019). Optical characterization of different waist diameter on microfiber loop resonator humidity sensor. *Sensors and Actuators A: Physical*, 285, 200-209.
6. Johari, M., Al Noman, A., Khudus, M. A., Jali, **M.**, **Yusof, H.**, Harun, S., & Yasin, M. (2018). Microbottle resonator for formaldehyde liquid sensing. *Optik*, 173, 180-184.
7. Johari, M., Khudus, M. A., Al Noman, A., Jali, **M.**, **Yusof, H.**, Harun, S., & Yasin, M. (2019). Microbottle resonator formaldehyde sensor. Paper presented at the *Journal of Physics: Conference Series*.